POST-SHOCK THERMOCHEMISTRY IN HYPERVELOCITY CO_2 AND AIR FLOW

BY

MANU SHARMA

DISSERTATION

Submitted in partial fulfillment of the requirements
for the degree of Doctor of Philosophy in Aerospace Engineering
in the Graduate College of the
University of Illinois at Urbana-Champaign, 2010

Urbana, Illinois

Doctoral Committee:

Professor Joanna Austin, Chair
Professor Nick Glumac
Professor Greg Elliott
Professor Ken Christensen

ABSTRACT

This work represents ongoing efforts to study high-enthalpy carbon dioxide flows in anticipation of the upcoming Mars Science Laboratory (MSL) and future missions to the red planet. The work is motivated by observed anomalies between experimental and numerical studies in hypervelocity impulse facilities for high-enthalpy carbon dioxide flows. In this work, experiments are conducted in the Hypervelocity Expansion Tube (HET) which, by virtue of its flow acceleration process, exhibits minimal freestream dissociation in comparison to reflected shock tunnels. This simplifies the comparison with computational result as freestream dissociation and considerable thermochemical excitation can be neglected. Shock shapes of the MSL aeroshell and spherical geometries are compared with numerical simulations incorporating detailed CO_2 thermochemical modeling. The shock stand-off distance has been identified in the past as sensitive to the thermochemical state and as such, is used here as an experimental measurable for comparison with CFD and two different theoretical models. It is seen that models based upon binary scaling assumptions are not applicable for the low-density, small-scale conditions of the current work. Mars Science Laboratory shock shapes at zero angle of attack are also in good agreement with available data from the LENS X expansion tunnel facility, confirming results are facility-independent for the same type of flow acceleration, and indicating that the flow velocity is a suitable first-order matching parameter for comparative testing. In an effort to address surface chemistry issues arising from high-enthalpy carbon dioxide ground-test based experiments, spherical stagnation point and aeroshell heat transfer distributions are also compared with simulation. Very good agreement between experiment and CFD is seen for all shock shapes and heat transfer

distributions fall within the non-catalytic and super-catalytic solutions.

We also examine spatial temperature profiles in the non-equilibrium relaxation region behind a stationary shock wave in a hypervelocity air Mach 7.42 freestream. The normal shock wave is established through a Mach reflection from an opposing wedge arrangement. Schlieren images confirm that the shock configuration is steady and the location is repeatable. Emission spectroscopy is used to identify dissociated species and to make vibrational temperature measurements using both the nitric oxide and the hydroxyl radical A-X band sequences. Temperature measurements are presented at selected locations behind the normal shock. LIFBASE is used as the simulation spectrum software for OH temperature-fitting, however the need to access higher vibrational and rotational levels for NO leads to the use of an in-house developed algorithm. For NO, results demonstrate the contribution of higher vibrational and rotational levels to the spectra at the conditions of this study. Very good agreement is achieved between the experimentally measured NO vibrational temperatures and calculations performed using an existing state-resolved, three-dimensional forced harmonic oscillator thermochemical model. The measured NO A-X vibrational temperatures are significantly higher than the OH A-X temperatures.

ACKNOWLEDGEMENTS

I thank my advisor, Professor Joanna Austin, for guiding my quest for scientific knowledge and her patience and support throughout the course of my graduate studies. The opportunity to work in the experimental hypersonic field is one that I am grateful for. I have only had one advisor, but I am sure that she is one of the best advisors a doctoral student could ever hope for. I wish her the absolute best for a successful career in academia.

Special recognition must go to Professor Nick Glumac, who has helped me immensely with all his spectroscopic expertise, allowing our research group to use his equipment, the basis of the in-house spectral simulation algorithm and inspiring my interest in all spectroscopic-based techniques, which will truly extend beyond my PhD studies.

Professor Graham Candler for letting me compare our results with his code, US3D. I am incredibly grateful for the chance to compare the experimental data with his code.

Professor Greg Elliott for a lot of experimental help along the way with suggestions for schlieren, spectroscopy and Rayleigh scattering.

Aaron Dufrene taught me so much along the way during my Masters when I didn't even know how to drill and thread a hole. Having access to his knowledge over the last 3 years while he has been at CUBRC has been completely invaluable.

Pat Lynch for all his experimental help along the way with my spectroscopic setups and discussions regarding the theory.

Andy Swantek for scaling down the MSL model and thermocouple installation. Bill Flaherty for all his hard work in the development, implementation and testing of the thermocouples in the HET. Without heat transfer capabilities, our ability for comparison with CFD would

have been much more limited.

Matt Maclean and Sriram Doraiswamy from CUBRC and University of Minnesota respectively - you both helped me a lot with my understanding of the computational side of my research.

My Mum and Dad. You have been through some tough times while I've been gone, and not having your only son around would have only made things worse. But your support for me, knowing that I had to leave Oz to do what I want to do, has always been absolutely rock-solid.

All my mates back home, thanks for always reminding me of all the other important stuff in life and taking my mind away from Mach reflections, excited states, aligning optics, vibrational modeling, Mars re-entry and shock shapes. Getting all those surf updates and cricket scores over the last 5 years has kept me sane. Shout out to Wibby and Junior. Slash, Axl and the rest of the (real) GNR. You rock.

And lastly, and most importantly, Nikki - if I hadn't met you, I would have left Champaign. It's as simple as that.

TABLE OF CONTENTS

LIST OF FIGURES

LIST OF TABLES

CHAPTER 1

INTRODUCTION

1.1 Planetary Re-entry

The upcoming Mars Science Laboratory (MSL) program has increased the interest in re-entry flow fields and the associated flow dynamics in a high-enthalpy environment. The general re-entry flow field is not new; an enormous amount of work has been previously completed, motivated by the intercontinental ballistic missile and the manned space program. Nevertheless, the flow field is extremely complicated and poses a very challenging environment for the experimentalist to interrogate and for the computationalist to predict. This is especially pronounced for any Martian mission as the energy transfer and storage processes of CO_2 are more complex to model than the diatomic species of an air flow field. By virtue of the flow acceleration process, certain ground-test facilities are incapable of fully replicating the thermochemical component of the flow physics. Modern predictive capabilities seek additional experimental data for the validation of complicated physical models, which aim to completely describe the coupling between the fluid dynamics and thermochemistry.

The MSL mission, scheduled for a 2011 launch, is the 15th attempt to land an unmanned vehicle on Mars. Previous efforts have been made by the USSR (Mars 2 through Mars 7), Russian Space Agency (Mars96) and NASA (for example: Viking I and II, Pathfinder, Phoenix) and the ESA (Beagle). A key feature of the MSL in comparison to its NASA predecessors is its capability for precision landing. The Viking and Pathfinder landing footprints were on the order of hundreds of kilometers, while the MSL is designed to land within 10 kms of its designated site. The MSL retains the 70-degree sphere-cone forebody shape of previous

vehicles, but is larger with a 4.572 m major diameter. Of these vehicles, the MSL is unique in the sense that it has a direct, non-ballistic entry into the Martian atmosphere. The Viking missions, while entering the Martian atmosphere at an 11 degree angle of attack, were inserted into orbit prior to landing. Subsequently, the MSL has higher entry velocities (roughly 6 km/s) which will cause higher aerodynamic heating. From the combination of its larger aeroshell size, high ballistic coefficient and non-zero angle of attack, MSL leeside transition to turbulence is expected early in its trajectory. As the aerothermodynamics of the MSL will be more complicated than previous missions, considerable effort has been expended to better characterize high-enthalpy, reacting carbon dioxide flow fields over 70 degree sphere-cone geometries. Towards this goal, experimental studies have been completed in a variety of facilities including the CUBRC (CalSpan University of Buffalo Research Center) family of facilities [2, 3, 4, 1], the HYPULSE expansion tube facility [5, 6], the T5 shock tunnel at Caltech [7] and the NASA Ames 42-inch shock tunnel [8]. Significant computational work has analyzed this data including work conducted at NASA [7, 9, 10, 11], CUBRC [12, 4, 13] and at the University of Minnesota [14, 15].

Following the MSL mission, it is expected that every future Martian mission - whether manned or unmanned - will have much larger characteristic dimensions than the previous Martian vehicle generation. Therefore, complicating aerothermodynamic issues encountered for MSL re-entry, such as forebody transition and non-negligible radiative heating rates, will be experienced by all future vehicles. These issues and the associated flow physics must be understood if future configurations are to be optimized. All of these future missions, and not just the MSL, will benefit from high-enthalpy CO_2 ground-test aerothermodynamic data.

1.2 Real Gas Effects

A defining aspect of the re-entry flow field, and any flight hypersonic condition, are real-gas or high-temperature effects. The two major physical features of a real-gas flow that concerns

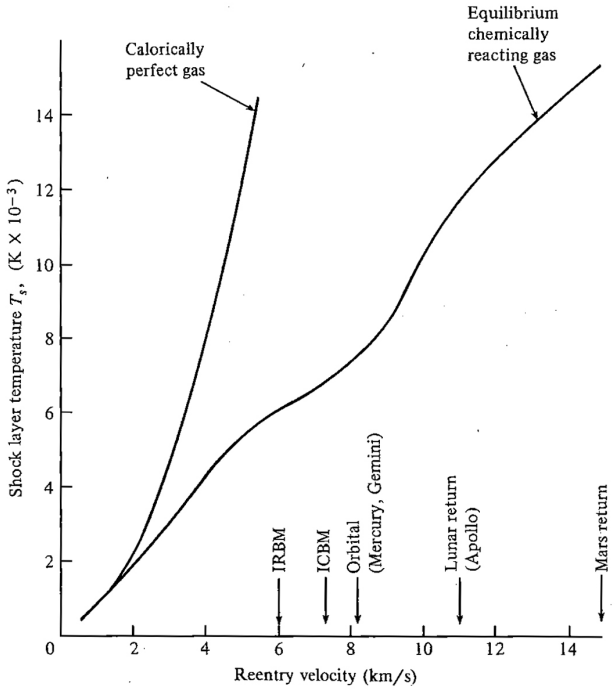

Figure 1.1: Shock layer temperature behind a normal shock for perfect and equilibrium reacting gas. Actual vehicle trajectory points are also included.

this research is vibrational excitation and dissociation. For shock waves in a high temperature gas, the Mach number no longer plays such a critical descriptive role of the flow field as it does for a calorically perfect gas. Instead, the flow is more aptly described primitive properties such as flow velocity, pressure and temperature. Post-shock temperatures calculated incorporating a chemically reacting gas will always be lower than calculations from calorically perfect gas relations as the energy is distributed amongst chemical and all the internal energy modes as opposed to just being confined to the external translational and internal rotational modes. The influence of thermochemistry upon shock layer temperature is clearly seen from Figure 1.1, which displays the strong divergence between the two solutions for re-entry velocities about 3 km/s at an altitude of 52 km/s.

For a gas flow in *thermal* equilibrium, the time scale over which the molecular thermal energy transfer process takes place is much faster than the characteristic time scale of the flow. Here a Boltzmann distribution exists; the internal energy mode (rotational, vibrational, electronic) temperatures will all be the same. Local *chemical* equilibrium will exist when

the chemical composition can be evaluated by using equilibrium T and p values. Chemical equilibrium implies that infinitely fast reactions are occurring. A *frozen* flow is one for which chemical reactions are neglected - the reaction rates are zero. In the situation where these local equilibrium conditions do not exist then it is termed a *non-equilibrium* flow field.

The term *hypervelocity* refers to high-stagnation enthalpy, high Mach number conditions generated within a facility for which real gas effects will be present. High Mach numbers can be achieved in facilities such as wind tunnels by lowering the sound speed without adjusting the flow velocity. However, due to the very low freestream temperatures, typically lower than 300 K, vibrational excitation or dissociation will not occur and only the underlying fluid mechanics are investigated. However, at hypersonic conditions thermochemistry must be considered if the flow field is to be completely described as the coupling between fluid mechanics and thermochemistry can play a significant role. The most prominent example is the so-called "Shuttle flap anomaly" whereby ground-test space shuttle pitch and moment values differed from flight measurements. The difference was subsequently determined to be due to high-temperature effects, namely the reduction in surface pressure on the Shuttle aft windward expansion surface due to real-gas effects [16]. Real-gas effects upon vehicle aerodynamics in CO_2 flowfields have been recorded. On the Pathfinder vehicle, perfect-gas and real-gas drag and pitching moment values diverged above Mach 9 for flight trajectory simulations. Also, the emergence of an unstable moment coefficient derivative was predicted due to the movement of the sonic-line as gas chemistry changed from non-equilibrium to equilibrium [17]. Entry data confirmed these predictions [18].

1.3 Motivation of Current Work

In the present work, we use an expansion tube to perform high-enthalpy studies of air and carbon dioxide flows. Experiments are performed in the Hypervelocity Expansion Tube (HET). The post-shock relaxation region behind a stationary, normal shock is studied to

demonstrate diagnostic capability within expansion tube flow fields and for comparison with a state-specific thermochemical model. The goals of the high-enthalpy CO_2 work was threefold. Firstly, to address previous discrepancies identified between experiment and computation in other hypersonic facilities [1] by obtaining the data in a facility which utilizes a different flow acceleration mechanism. Secondly, to expand the experimental database for computational physical model validation to address concerns such as CO_2 vibrational modeling and surface catalysis. In general, models of non-equilibrium flow chemistry have very few high temperature, low density datasets for validation and it is expected that any extra data will be appreciated by the CFD community. Lastly, the demonstration of heat transfer capabilities within the newly constructed facility.

Nozzles are used to accelerate the flow via expansion of shock-compressed gas. In ground-test facilities, this gas is compressed by either an incident or reflected shock. During the expansion process, the rapid decrease in pressure decreases the molecular collision rate and restricts the energy transfer rate. The collision rate is sufficient enough to accommodate translational and rotational equilibrium, but not adequate enough to achieve vibrational equilibrium. This leads to vibrational freezing, such that a constant vibrational temperature is measured downstream of the nozzle exit [19]. For a chemically reacting gas, chemical freezing will also occur as chemical changes require higher molecular collision rates than vibrational changes. Hence, the facility generated flow will have more thermal energy than an equilibrium slug of gas with the same rotational (or translational) temperature. In a situation of increased density, such as behind a shock wave, this extra energy will be released. The Landau-Teller model is typically used for the vibration-translation (V-T) energy transfer process inside the nozzle. As inputs, the model uses empirically determined vibrational relaxation times from measurements behind shock waves. The application of these values to nozzle flows has received considerable interest due to the differences in the two types of flow fields; the temperatures are very different and one process involves de-excitation (nozzle) while the other is an excitation (shock). Recent computational efforts have focused upon

the vibrational modeling [14] and chemistry-vibration coupling [15] in high-enthalpy nozzle flows. Without a nozzle, the expansion tube offers a hypervelocity ground-test alternative without any chemical or vibrational freezing.

Certain anomalous findings were observed during the comparison of experiment with simulation for the work described in Section 1.1. On certain sections of the MSL forebody, the heat flux was measured to be closer to the aphysical super-catalytic boundary condition. At angle of attack, best agreement of a transitional experimental heat flux profile with simulations resulted in laminar windside super-catalytic behavior and turbulent leeside non-catalytic behavior. The largest anomaly was the large discrepancy in the shock shape, with an experimental shock stand-off distance 225% larger than prediction. None of these anomalies have yet to be resolved, however, suspected causes span both experimental and computational issues. From the experimental stand-point, a significant portion of the data was obtained in the LENS I facility which exhibits considerable freestream dissociation which has proven to be further exacerbate CO_2 vibrational relaxation processes within the nozzle.

1.4 Outline of Document

The second chapter, *Experimental Setup*, discusses the advantages and disadvantages of using an expansion tube for hypervelocity testing. The general gas dynamic operation of an expansion tube is also addressed and how it is well-poised to investigate thermochemical effects. The operational capabilities of the HET are described, including the addition of certain integral components to the facilities' operation. The third chapter, *Test Gas Characterization*, details the a priori prediction of core flow size and a non-dimensional parameter that correlates test gas noise levels. By providing a more rigorous characterization of the test condition prior to any experimental testing, the test condition selection process will be considerably expedited. Vibrational temperature measurements using OH and NO emissions are detailed in the fourth chapter, *Post-Shock Relaxation Region Vibrational Temperature*

Measurements. The nitric oxide results are compared with a state-specific thermochemical model. Finally, the high-enthalpy results carbon dioxide are presented in the fifth chapter, *Experimental and Numerical Investigation of Hypervelocity Carbon Dioxide Flow over Blunt Bodies*. Here shock shape and heat transfer distributions are compared with axisymmetric simulations with detailed carbon dioxide vibrational modeling.

CHAPTER 2

EXPERIMENTAL SETUP

2.1 The Expansion Tube

An expansion tube has several advantages and disadvantages in comparison with the more common reflected shock tunnel [20, 21, 22]. In an expansion tube, the initial shock interacts with a contact surface generating an unsteady expansion that further accelerates the test gas. Theoretically, a wide range of test conditions with minimal free stream dissociation can be achieved by varying initial pressures [23, 24]. In contrast, in a shock tunnel, chemical and vibrational freezing commonly occur in the nozzle (see Section 1.3), and the Mach number of the test gas can only be varied by exchanging nozzles. In an expansion tube, the test gas does not directly follow the transmitted shock and as a result viscous effects become more pronounced due to the extra section of pipe. For example, the HET bore diameter is 152 mm but by the time measurements are taken inside the test section there is typically only about 50.8-63.5 mm of core flow. In comparison to perfect gas facilities, such as hypersonic wind tunnels, expansion tubes have much shorter test times. In the HET, test times are on the order of 100-250 μs. In practice, expansion tube operating ranges have been limited by secondary diaphragm considerations [25] and the appearance of large amplitude test flow disturbances [26]. Other expansion tube/tunnels facilities around the world include the newly constructed LENS XX facility at CUBRC [27], JX-1 in Japan [28], the X1 [29], X2 [30] and X3 [31] facilities at the University of Queensland and a facility at Stanford [32].

2.1.1 Calculation of thermodynamic state

The flow processes in an expansion tube are complex. Nevertheless, simple one-dimensional, inviscid, unsteady wave interactions may be used to calculate the ideal test conditions including thermodynamic state, flow velocity, and test time as a starting point for facility design.

The expansion tube consists of three sections (a driver, driven and expansion section), initially separated by two diaphragms. Figure 2.1 is an x-t diagram for typical HET gas dynamic operation. After the rupture of the primary diaphragm, denoted by the dashed vertical line to the left, a shock wave propagates downstream and initially accelerates the test gas. In this fashion, the driver and driven sections operate as a standard shock tube. The rupture of the secondary diaphragm, denoted by the dashed vertical line to the right, creates an unsteady expansion fan which further accelerates the flow. In this figure, the test gas is denoted as state 7. Figure 2.2 is a typical pitot pressure trace obtained in the test section. As an Eulerian measurement, the major flow features can be identified as they arrive at the probe. In order these include: the transmitted shock, followed by the acceleration slug (state 6), the secondary contact surface across which velocities and pressures must be matched and then the test gas. In Figure 2.1, the test gas is terminated by the arrival of the secondary expansion tail.

The secondary diaphragm, assumed in this initial theoretical analysis to be thin and break instantaneously upon arrival of the incident shock, is represented as a contact surface. Pressure-velocity (p-u) polars are used to calculate states 6 and 7 (see Figure 2.1) resulting from incident shock-contact surface interaction. A shock is transmitted and the expansion wave between regions 2 and 7 can be either right-facing or left-facing. The head and tail of the expansion have positive slopes as the flow in state 2 is supersonic and to the right. State 7 is the test gas that has been further accelerated beyond the post-shock state 2 by the unsteady secondary expansion. The secondary expansion wave will interact with the contact surface between states 2 and 3, resulting in reflected and transmitted waves. p-u

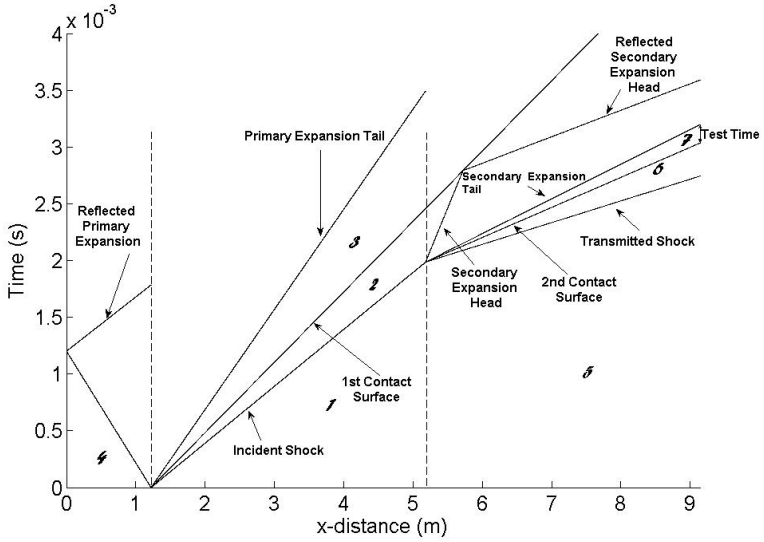

Figure 2.1: Sample x-t diagram of the calculated gas dynamic processes for the Air-5 run condition with a test gas Mach number of 7.42. Initial conditions are p_4=2500 kPa, p_1 = 1.5 kPa and p_5=175 mTorr. The driver and acceleration sections are filled with helium and the driven section with air. Calculations assume perfect gas.

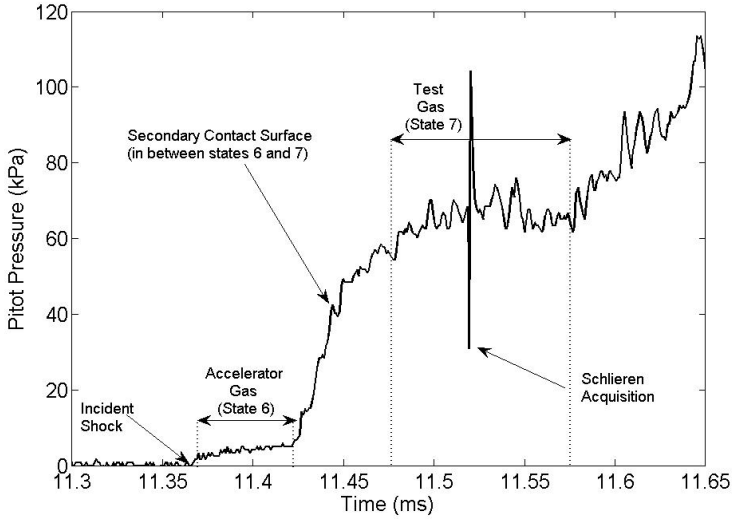

Figure 2.2: Typical pitot pressure trace in the HET for the Air-5 run condition.

polar calculations show this reflected wave to also be an expansion. The interaction of the incident and reflected secondary expansion waves creates a non-simple region.

The strength of the primary left-facing expansion wave is dependent on the initial pressures, but is in general sufficiently strong to accelerate the gas past sonic velocities. The head of the primary expansion wave will reflect from the upstream end of the tube and the tail will trail the primary contact surface.

Test time varies with the initial conditions of the expansion tube, and can be estimated from an x-t diagram. The test time begins with the arrival of the state 6-7 contact surface, and it is terminated by the arrival of either i) the head of the reflected secondary expansion wave, or ii) the tail of the secondary expansion wave, or iii) the arrival of the primary expansion from the driver, which ever occurs first. In HET operation, only cases i) and ii) need to be considered [25, 33]. For these two cases, the maximum test time corresponds to the case in which the reflected head and the tail of the secondary expansion fan arrive at the end of the tube at the same time. For the run condition shown in Figure 2.1, the test time is terminated by the expansion tail. The test time is determined using a method of characteristics similarity solution within the complicated non-simple region. The details of this approach and additional discussions of HET gas dynamic operation can be found in Dufrene et al [25] and Sharma [33].

2.1.2 HET facility design

The HET facility is constructed of honed (0.2 μm Ra) 304/304L stainless steel with an inner diameter of 152 mm and a wall thickness of 0.95 cm. The HET consists of three main sections labeled as the driver, driven and acceleration sections. The length of the driver section is 1.22 m, while the driven and expansion sections are both 3.96 m long, resulting in a total length of 9.14 m. Tube lengths were chosen based upon theoretical gas dynamic calculations outlined in Dufrene et al. [25] and Sharma [33]. The driver and driven sections are initially separated by a 1.27 mm thick 5052-H32 Aluminium primary diaphragm, while the

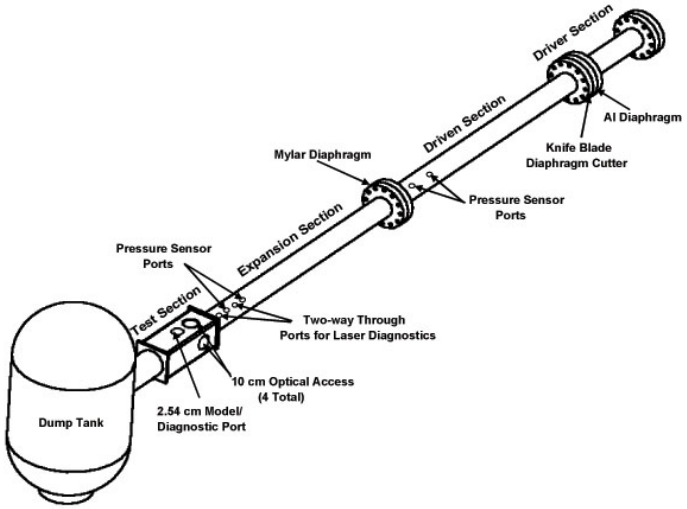

Figure 2.3: Schematic of the HET facility, identifying its key features.

driven and acceleration sections are separated by a 12.7 μm Mylar secondary diaphragm. The initial gas pressure and composition can be varied to achieve nominal Mach number operating conditions between 3.0 to 7.5 and stagnation enthalpies of 4.5 to 9.0 MJ/kg. The tube will withstand initial pressures up to 5500 kPa and the acceleration section is capable of achieving a vacuum of less than 100 mTorr. The facility is mounted on linear bearings for easy access to the diaphragm stations and to allow tube recoil during the experiment. Ten instrumentation ports are located along the tube, of which four are currently instrumented with PCB 113A26 piezoelectric pressure transducers for wave time-of-arrival and static pressure measurements. Pitot pressure measurements in the test section were made using the same type of pressure sensor mounted normal to the flow field using the sting described in Section 2.1.3. The test section shown has a sliding seal and three-way 100 mm diameter optical access. Figure 2.3 is a schematic of the HET with the major components identified.

The facility is initially evacuated, then each section filled to the desired initial pressure. The primary diaphragm burst pressure (driver pressure) is measured using a Setra 206 pressure gauge. Driven and accelerator initial fill pressures are monitored using MKS Piezo+ A900-02 transducers. Vacuum pressures (below 2000 mTorr) in the accelerator section are measured using a MKS Baratron 626A transducer with 2 Torr fullscale, rated to

0.25% of the reading. This model was deliberately selected as the capacitance manometer pressure-measurement mechanism is invariant to the gas composition. Initial pressures in the accelerator section are typically on the order of 300 mTorr, and the influence of air-leakage into the acceleration section is mitigated by initially evacuating the section down to 200 mTorr, flushing with the acceleration gas up to 12 kPa and then performing the final evacuation down to the desired pressure. Within the facility, the acceleration section leak-rate was measured to be 0.3-0.4 mTorr/min and the subsequent partial pressure of air based upon these leak-rate measurements is low enough such that the effect is negligible based on perfect gas dynamic calculations. Characterization of the out-gassing phenomena yielded a maximum 7 mTorr increase after the final accelerator evacuation. Pressure data were recorded using a National Instruments data acquistion system, consisting of a PXI-1031 chassis, a BNC-2100 8 channel connector block and a 14-bit PXI-6133 3 MS/s simultaneous sampling multi-function data acquisition module. Facilty operation has been previously characterized experimentally and numerically [25, 33, 34].

In an expansion tube, imperfect secondary diaphragm rupture, shorter test times and core flow reduction due to acceleration section viscous effects result in a challenging measurement environment. However, the advantages of minimized freestream dissociation and no non-equilibrium processes during a nozzle expansion, make the expansion tube an attractive alternative means for creating hypervelocity flows.

2.1.3 New Sting Design

The first rigid sting for the test section in the HET consisted of a 0.245 m (9.75 inch) long rigid rod which was welded to a 0.025 m (1 inch) thick flat plate. Cracking on the upstream side of the sting weld (connection between the rod and flat plate) forced a re-design of the sting concept (see Figure 2.4). The new sting design is very similar to the one described above, however, it consists of a 0.178 m long and 0.051 m (2 inches) diameter sting welded to a 0.025 m thick plate. Both pieces were made from 1018 steel with a rated yield strength

of 441 MPa. The increased radius and the reduced moment arm considerably decrease the stress upon the weld. The sting mounting system, however is markedly different from its predecessor and was designed with the twin goals of improved experimental flexibility and strength in mind. The sting assembly (rod and plate plate) is connected to a support plate which at its other end is connected to a spacer block which is welded to the cover flange of the bottom test section circular sight glass. 4 tapped holes for 3/8-24 sockethead capscrews allow the sting rod to be mounted onto the support plate and 8 tapped holes for 7/16-14 holes provide the connection between the support plate and spacer. Figure 2.5 a) shows a picture of the fully assembled sting outside the test section, while Figure 2.5 b) shows it installed within the test section. Simulations of the new sting using NX 6.0 indicated the maximum stress at the location of the fracture point on the original sting was 91.15 MPa. Since its installment, over 700 shots have been conducted in the HET with the new sting and no signs of structural failure have been observed. Additional information can be found in Sharma [33]. Machine drawings can be found in Appendix B.

2.1.4 Knife Blades

The original knife blades [35] were designed as a single-piece, self-contained tool made from A2 tool steel. Two sets of these original knife blades were constructed, however both failed. After the first tool broke after approximately 50 shots, modifications to the second tool were made. These modifications improved the tool life [33], however the knife blades broke once more after approximately 150 more shots. In both cases, the tool failure occurred as shown in Figure 2.6 and is a result of the force of the post-rupture diaphragm petals "slapping" up against the blocks. This failure is attributed to residual stresses present in the tool steel after the hardening process. To ensure that the knife edge remained sharp with extended usage and displayed excellent wear resistance, it is an absolute must that the tool be hardened. However, evaluation of the original design's hardening approach and its application considering the tool's shape revealed certain design mistakes. The original tool was hardened to

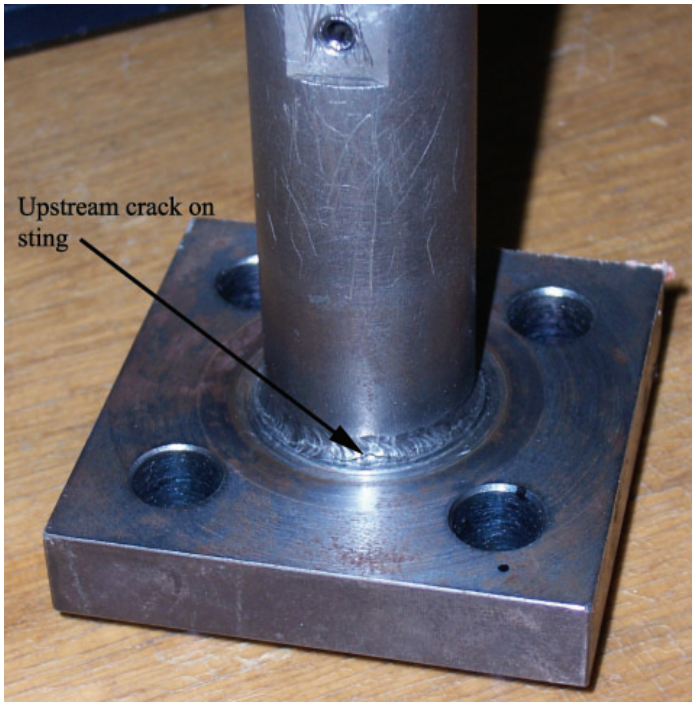

Figure 2.4: Close-up picture of the old sting which shows the location of the failure point and crack on the front of the weld between the rigid rod and flat plate.

(a) (b)

Figure 2.5: a) The new sting fully assembled outside the test section, showing the sting connected to the spacer block via the support plate. The spacer block is installed on the bottom test section port. b) The new sting installed within the test section. The front face has a total of 18 10-32 tapped holes, providing mounting capabilities from 44.45 mm to 63.5 mm above and below the tube centerline respectively.

(a) (b)

Figure 2.6: a) Back-view picture of the knife blades showing the nature of the fracture and the broken quarter piece. b) A close up of the broken quarter piece indicating the plastic deformation caused by the petal slapping force.

60 HRC, which dramatically increases the brittleness of the A2 tool steel. Considering the very high impulses experienced by the tool, it is highly recommended not to heat treat A2 tool steel to such a high hardness [36]. As one piece, the thickness of the tool varied from 35.56 mm to 3.96 mm. With such drastic section changes throughout the part, during the cooling process the thin section will cool and then harden more rapidly than the adjacent thicker section, resulting in residual stresses very close to the yield strength of the material [37].

The new design consisted of separated pieces, with 4 individual blocks and a 4-spoke knife cross, that were welded together after machining of the individual components. The separation of the tool into different components eliminated varying cross-sectional areas and was aimed at significantly reducing the presence of residual stresses post heat treatment. The blocks were cut from the previous single-piece parts (and hence already hardened) and attached to the diaphragm flange with two 5/16-24 screws per block. The diaphragm flange was modified by cutting grooves into the internal diameter, which allowed insertion of the knife cross as shown in Figure 2.7. The knife cross was assembled by welding two separate half-pieces to a single full piece. Each piece was 3.97 mm thick (5/32 inches). At

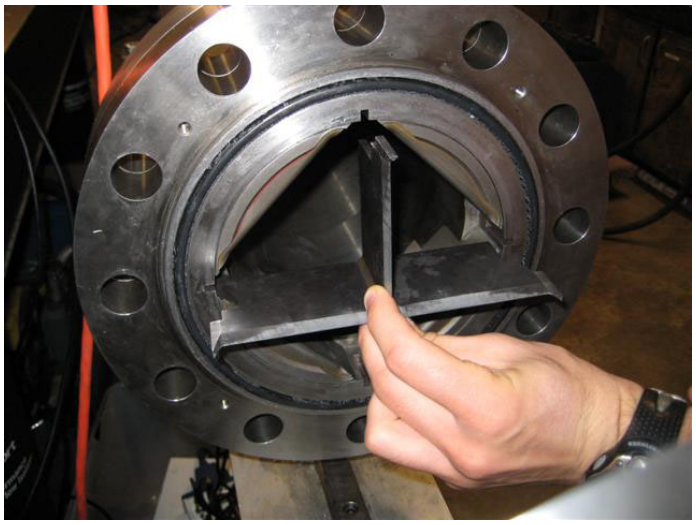

Figure 2.7: Knife cross diaphragm cutter mechanism being installed into the HET. Note the modified diaphragm flange with milled grooves to provide a locational fit for the knife cross.

its radial extent, each piece was machined with a double-step configuration so as to clear both the diaphragm step and the tube inner diameter. The steps were machined for a locational clearance fit with the diaphragm flange inner diameter and extensive clearance from the tube inner diameter. This ensures the knife cross movement and fit is constrained via contact with the diaphragm flange as opposed to the inner tube diameter. The full piece had grooves machined 0.25 mm deep on either side, with the grooves extending the entire 63.5 mm depth of the knife cross. These grooves assisted with half-piece placement during the welding procedure. Before welding, each of the three pieces was machined with the 30 degree full angle knife edge, recessed such that the tip plane of the knife edge is located 5.08 mm from the front of the piece. However, at the inner radial extent of each piece a section was left unmachined such that after welding a 12.5 mm by 12.5 mm square section remained.

Considerable efforts were undertaken in order to reduce the presence of residual stresses within the knife cross due to the complicated multi-stage fabrication process. Before welding, the entire knife cross assembly was pre-heated and checked that a uniform temperature of 470 K had been achieved. The pre-heating processes is recommended to prevent filler seam

crackage during and or after the weld has been applied. After welding, the assembled knife cross was soft annealed to return dimensional stability and relieve any stresses introduced into the metal which could have occurred due to the application of intense, localized heat to a very thin metal piece only 3.97 mm thick. Post annealing, the center section was machined out in order to match up the knife edge angles at the center of the knife cross. The final stage was the heat treatment. The piece was double tempered at approximately 820 K, to provide a final hardness of 56 HRC and decrease dimensional changes during the heat treatment process [36]. Grinding was then performed where required to account for any steel movement (change in length) during the hardening and to recover the final dimensions. Machine drawings for the entire knife blade assembly including the modified diaphragm flange can be found in Appendix B.

CHAPTER 3

TEST GAS CHARACTERIZATION

3.1 Introduction

For a given test gas, the unique gas dynamic operation of the expansion tube permits the user to consider different acceleration conditions, while keeping test gas properties of interest, such as stagnation enthalpy, nominally constant. The choice of the acceleration condition is an important consideration for test condition selection. Improving the *a priori* knowledge of expected test conditions will result in significant time-saving. Prior to this work, HET test condition characterization was achieved in very much a "trial and error" fashion, requiring the evaluation of candidate conditions via the collection of data rather than evaluation based upon theoretical or computational prediction. For example, to compare the test gas noise levels and core flow size of 4 different run conditions, it is estimated that 15-20 shots are required - corresponding to 30-40 hours of facility operation. The following sections detail HET test gas noise level and core flow size predictive capabilities.

3.2 Test Gas Disturbances

Accurate assessment of the test time is an important component for expansion tube testing. The test time is marked by the arrival of the secondary contact surface and terminated by either the arrival of the secondary expansion tail or the reflected expansion head. Due to the large pressure rise across the secondary contact surface, the arrival of the test time is generally an easily distinguishable event. The much lower pressure increase (expansion

head) or decrease (expansion tail) ensures that the termination of the test time is a more difficult event to determine. For sufficiently high levels of noise, the test time can be rendered completely unusable as test time termination cannot be identified. This motivates the desire to identify sources of test time noise for efficient test condition selection purposes.

3.2.1 Richtmyer-Meshkov Instability

A proposed source of test time noise was via the Richtmyer-Meshkov instability (RMI). The RMI occurs when an interface is impulsively accelerated. In this case, the interface is the secondary contact surface which is accelerated by the incident shock. It is proposed that the growing instability encourages mixing between the two gases and introduces disturbances into the test gas. The driving mechanism for the RM instability is the baroclinic generation of vorticity arising from the cross product of the density and pressure gradients ($\Delta p \times \Delta \rho$). For our application, $\Delta \rho$ exists from initial conditions and the Δp is provided by the incident shock pressure jump. The RM instability has been extensively studied in shock tube investigations [38, 39, 40]. In all of these cases, there was initially no pressure gradient across the interface.

The instability is named for the linear analysis presented by Richtmyer [41] and its experimental verification by Meshkov [42]. The RM interfacial perturbation is initially characterized by a linear growth region, followed by a non-linear region when the perturbation amplitude is no longer small compared to the wavelength. During the linear portion of the instability, the perturbations have a sinusoidal shape whereas during the non-linear process it evolves into features consisting of shapes described in the literature as "bubbles" and "spikes" which leads to a turbulent mixing zone.

Richtmyer's linear impulsive model is mathematically described as

$$\frac{d\eta}{dt} = k u_{67} A \eta_0 \tag{3.1}$$

where k is the wave number of the sinusoidal perturbation, A is the Atwood number and η_0 is the initial perturbation. The Atwood number is defined to be

$$A = \frac{(\rho_5 - \rho_1)}{(\rho_5 + \rho_1)} \tag{3.2}$$

where states 5 and 1 denote the initial conditions of the acceleration and driven sections respectively, Fig 2.1.

Equation 3.1 only covers linear growth when $\eta << \lambda$, however it is expected that considering the length of acceleration section, the growth will become non-linear and "bubble" and "spike" features will be created. To account for this, the equation of Sadot [43] is used which describes the linear, non-linear and asymptotic behavior of the bubbles and spike evolution

$$U = U_0 \frac{1 + Bt}{1 + Dt + Et^2} \tag{3.3}$$

where t denotes the time after secondary diaphragm rupture and U_0 is the linear growth rate, described in Equation 3.1. Additionally,

$$B = U_0 k \tag{3.4}$$

$$D = (1 \pm A)\, U_0 k \tag{3.5}$$

$$E = \left[\frac{(1 \pm A)}{(1 + A)}\right] \left(\frac{1}{2\pi C}\right) U_0^2 k^2 \tag{3.6}$$

In the above equations, the plus and minus signs denote bubble and spike features respectively. For the Atwood numbers considered in this work, $C = 1/(3\pi)$. Sadot et al. also integrated Equation 3.3 to determine the amplitude as a function of time

$$\eta_s = \left[\frac{U_0}{\sqrt{4E - D^2}} \left(2 - \frac{BD}{E}\right)\right] \tan^{-1}\left[\frac{2Et + D}{\sqrt{4E - D^2}}\right] + \frac{U_0 B}{2E} \ln\left(1 + Dt + Et^2\right) + K \tag{3.7}$$

Due to the pressure difference, the secondary diaphragm will bulge downstream. It is assumed that this convex bulge forms the initial perturbation bulge, such that the wavelength is equal to the inner tube diameter ($\lambda = 2r$). Typically, perturbation length scales are much smaller than characteristic facility dimensions, however other studies have looked at comparable sizes, for example Houas et al. [44]. The Mylar diaphragm can be modeled as a membrane since $\eta_0 > 5\tau$, where τ is the thickness of the Mylar diaphragm and equal to 12.7 μm. The initial deflection of the diaphragm [45], corresponding to the initial perturbation amplitude is equal to

$$\eta_0 = \sqrt[3]{\frac{\Delta \, \mathrm{Pr}^4}{2.86 E \tau}} \tag{3.8}$$

where E is Young's modulus and ΔP is the pressure difference across the diaphragm.

Table 3.1 summarizes four candidate test conditions used for the high-enthalpy CO_2 work, Chapter 5. The values are generated from the one-dimensional, perfect-gas, inviscid code for HET operation. In the table, state 7 denotes test conditions and ΔT_{67} is the temperature difference across the contact surface, $T_6 - T_7$. The sound speed ratio, c_3/c_2, was deliberately selected to be the same in each case so that test gas disturbances due to frequency focusing of lateral waves [26] were equal for each test condition.

Numerous shots were taken for each run condition and the standard deviation is calculated across the most steady portion of the test gas, neglecting the initial perturbed response due to the arrival of the contact surface. At each time, the average mean pitot pressure was calculated to account for the shot-to-shot variation. The standard deviation of the time-averaged pressure vector was then calculated, which is representative of the noise levels (deviation about the mean) within the test gas. Figure 3.1 presents the perturbation growth rate as a function of time from diaphragm rupture to the arrival of the contact surface at the end of the acceleration section. In Figure 3.1, each run condition displays initial linear growth up to a peak value followed by the asymptotic decrease characteristic of the non-

Label	A	M_7	U_7 (m/s)	σ (kPa)
CO2-CO2 (RC2)	-0.967	5.52	2998	1.86
CO2-Air (RC5)	-0.974	5.72	3059	2.52
CO2-Hel (RC8)	-0.979	5.75	3066	5.84
CO2-Arg (RC11)	-0.973	5.57	3014	1.81

Table 3.1: Comparison of four different CO_2 test gas run conditions for RMI analysis. These same run conditions were investigated in the high-enthalpy CO_2 Mars Science Laboratory study detailed in Chapter 5. For additional test condition properties see Table 5.1.

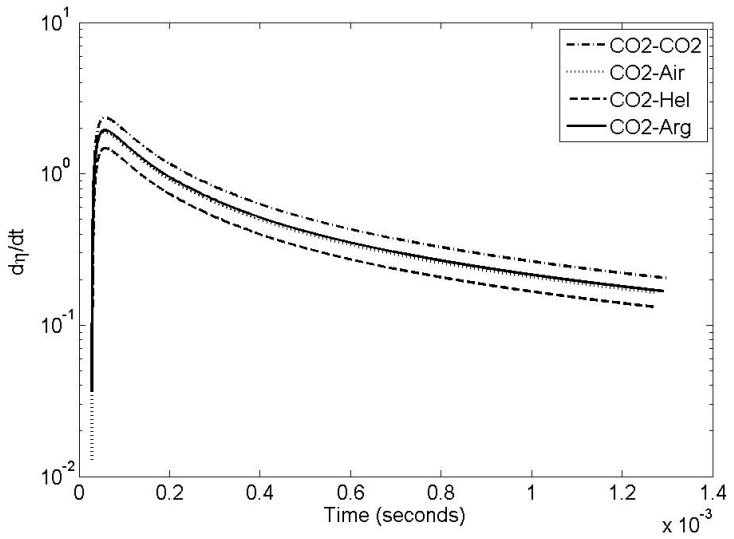

Figure 3.1: Growth rates as a function of time for four different run conditions, as described in Table 3.1.

linear regime. Linear behavior accounts for, at most, only 6% of the total contact surface travel time. The single-mode model of Equation 3.3 is only valid when $\eta_0 k < 0.6$ and for these conditions the maximum $\eta_0 k$ value is 0.286, corresponding to an argon acceleration gas.

From Figure 3.1 and Table 3.1, no consistent agreement is observed. In fact, from the experimental observations, the CO_2-He run condition test gas experiences the largest perturbations while the RMI calculations predict it to be the most stable. Therefore, it is concluded that the Atwood number is not a correlating parameter for test gas noise levels.

Driven-Acc Gas	p_1 (kPa)	p_5 (mTorr)	$\rho_1 c_1$ kg/(m^{2}s)	$\rho_5 c_5$ kg/(m^{2}s)	u_s (m/s)	D kg/(ms^2)	σ (kPa)
CO_2-CO_2	1.2	150	5.74	0.094	1853	10810	1.86
CO_2-Air	1.2	180	5.74	0.096	1853	10905	2.52
CO_2-He	1.2	1050	5.74	0.300	1853	11192	5.84
CO_2-Ar	1.2	135	5.74	0.093	1853	10808	1.81
CO_2-He	6.0	1600	28.73	0.349	1447	42077	8.98
Ar-He	6.0	1600	31.00	0.349	1671	52384	25.78
Air-He	6.0	1600	24.17	0.349	1632	40015	8.02
Air-He	1.5	175	6.06	0.04	1992	12151	4.62

Table 3.2: Comparison of eight different run conditions for acoustic impedance analysis.

3.2.2 Acoustic Impedance

The characteristic acoustic impedance, ρc, was also investigated as a correlating parameter for test gas noise levels. To accomplish this, 4 additional run conditions on top of the 4 described above were investigated. Table 3.2 is a summary of the 8 different run conditions. The first four run conditions have the same test gas (CO_2) with different acceleration gases, while the next three run conditions have the same accelerator conditions with different test gases. The last entry is the Air-5 run condition used for the spectroscopic studies, Chapter 4. Included in the table are the initial conditions, the characteristic acoustic impedances across the secondary contact surface and the calculated test gas standard deviations. Experimentally, we saw that the test gas noise magnitude correlated with the expression

$$D = u_s \left(\rho_1 c_1 + \rho_5 c_5\right) \tag{3.9}$$

From the table it is evident that larger D values correspond to larger levels of test gas noise. The correlating factor is dependent upon the total characteristic acoustic impedance across the secondary diaphragm, ($\rho_5 c_5 + \rho_1 c_1$). This suggests that larger acoustic impedances will result in larger test gas perturbations, as the ratio of acoustic force to velocity amplitude will be increased.

As a qualitative indication of the difference in test gas noise, Figure 3.2 is included.

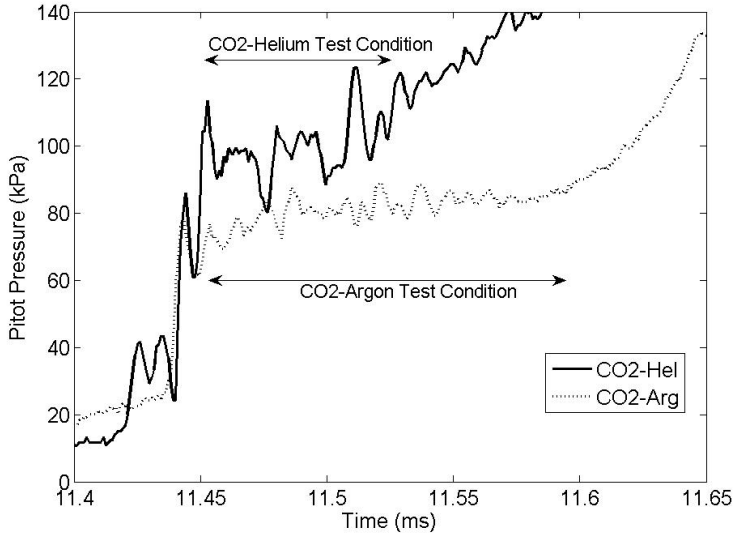

Figure 3.2: Pitot pressure time history comparison between two different interfaces, CO_2-Ar and CO_2-He. Acoustic impedance correlation predicts that the CO_2-He interface should be more unstable.

Typical test gas pitot pressure traces for the CO_2-He and CO_2-Ar interface run conditions are shown (3rd and 4th rows in Table 3.2 respectively). For these two cases, the test gas conditions (temperature, velocity) are very similar. Furthermore, the primary contact surface sound speed ratio, c_3/c_2, is also the same so according to the theory of Paull and Stalker [26] these two conditions should display the same level of test gas noise. Test gas perturbations are much more pronounced in the helium case, consistent with the calculated characteristic acoustic impedances.

We now seek a mathematically based description of test gas pitot pressure disturbances in terms of the characteristic acoustic impedance. The fluctuations in the pitot pressure produced by a small disturbance, $\phi(x,t)$, can be approximated to the first order in the derivatives of ϕ as [26]

$$P_T = P_{T_0}\left\{1 + \left[\frac{2M_7^2 - 1}{M_7^2 - (\gamma - 1/2\gamma)}\right]\frac{1}{u_{67}}\frac{\delta\phi}{\delta x} - \frac{\gamma}{c^2}\frac{\delta\phi}{\delta t}\right\} \tag{3.10}$$

In Equation 3.10, P_T is the fluctuation about the unperturbed pitot pressure, P_{T_0}. We assume ϕ to be an acoustic disturbance that oscillates sinusoidally in time such that ϕ is a function of only t. As a result, the middle term in Equation 3.10 will drop out. From linear acoustic theory (where ∞ denotes the undisturbed state), we have

$$\frac{\delta\phi}{\delta t} = \frac{P_\infty - P}{\rho_\infty} \tag{3.11}$$

Substitution of Equation 3.11 into Equation 3.10 yields

$$P_T = P_{T_0}\left\{1 - \frac{\gamma}{c^2}\left[\frac{P_\infty - P}{\rho_\infty}\right]\right\} \tag{3.12}$$

The pressure disturbance, p, is equal to $P - P_\infty$. It represents the acoustic contribution to the overall pressure field and oscillates as [46]

$$p = p_{pk}\cos(\omega t - \beta) = \mathrm{Re}[\hat{p}e^{-i\omega t}] \tag{3.13}$$

where p_{pk} is the peak pressure, ω is the angular frequency, β is the phase shift and $\hat{p}$ is the complex pressure amplitude and equal to $p_{pk}e^{i\phi}$. As a result, Equation 3.12 will reduce to

$$P_T = P_{T_0}\left[1 + \frac{\gamma p_{pk}}{c^2\rho_\infty}\cos\left(\omega t - \beta\right)\right] \tag{3.14}$$

Along a non-moving surface S_0, the complex pressure amplitude can be written as [46]

$$\hat{p} = v_{in}\rho c\zeta(\omega) \tag{3.15}$$

This yields the following expression for the peak pressure, p_{pk}, in terms of the characteristic acoustic impedance

$$p_{pk} = \frac{v_{in}\rho c\zeta(\omega)}{e^{i\beta}} \tag{3.16}$$

Treating the secondary diaphragm as the surface S_0, substituting Equation 3.16 into Equation 3.14 and evaluating the expression at the local conditions provides

$$P_T = P_{T_0}\left[1 + \frac{u_s\left(\rho_1 c_1 + \rho_5 c_5\right)}{P_7} \cdot \frac{\zeta\left(\omega\right)}{e^{i\beta}} \cos\left(\omega t - \beta\right)\right] \tag{3.17}$$

The above expression incorporates a non-dimensional parameter, τ, defined to be

$$\tau \equiv \frac{u_s\left(\rho_1 c_1 + \rho_5 c_5\right)}{P_7} \tag{3.18}$$

Physically, τ is a measure of the ratio of acoustic pressure to the overall static pressure field. For a matrix of HET run conditions, chosen with desired test gas properties in mind (for example, Mach number or stagnation enthalpy) so that the static pressure will be very similar in each case, the quantity theoretically identifies increasing test gas noise with increasing characteristic impedance across the secondary diaphragm station. This is generally consistent with experimental observation - larger τ values correspond to larger levels of measured test gas noise. In Table 3.3, the results for the last run condition, Air-5, are not consistent with the correlation. According to its τ value, it should have the largest amount of test gas noise, however experimentally only a moderately low amount of noise was seen. This highlights inadequacies in the current presentation; namely that no frequency dependence is incorporated and that the non-dimensional quantity, τ, does not provide a quantitative prediction of the level of test gas noise. Therefore, at this stage, it can be concluded that the correlation only provides a qualitative indication of one test condition's suitability over another within a matrix of test conditions, *where each run condition has been chosen with desired test gas properties in mind.* It should also be noted that τ includes the static pressure, while test gas noise levels were measured using the pitot pressure. This does not make it possible to predict numerical values for test gas noise, however it does serve as a comparative platform between test conditions to determine which cases are more suitable based upon test gas noise level considerations.

Driven-Acc Gas	D kg/(ms^2)	P_7 (kPa)	τ	σ (kPa)
CO_2-CO_2	10810	3.70	2.93	1.86
CO_2-Air	10905	3.20	3.38	2.52
CO_2-He	11192	3.14	3.52	5.84
CO_2-Ar	10808	3.56	2.90	1.81
CO_2-He	42077	3.84	10.95	8.98
Ar-He	52834	4.06	12.93	25.78
Air-He	40015	4.30	9.33	8.02
Air-He	12151	0.77	15.81	4.62

Table 3.3: Summary of the eight run conditions used for the acoustic impedance analysis including the non-dimensional correlation parameter, τ, identified from theoretical analysis.

3.3 Core Flow Prediction

In the acceleration section, the wall boundary layer behind the transmitted shock, which develops with increasing distance, entrains mass from the region between the contact surface and shock (state 6) resulting in an acceleration of the contact surface and deceleration of the transmitted shock. This phenomena has been comprehensively investigated by Mirels for both laminar and turbulent boundary layers in shock tubes [47, 48, 49, 50]. Subsequently, the core flow (state 7, arriving after state 6) size is reduced due to the development of this boundary layer. In a shock tube, the test condition arrives directly behind the shock wave and the measurement extent (core flow size) will not be affected by viscous effects. However, in the expansion tube, where the test condition arrives after the acceleration slug and its accompanying boundary layer, the test gas core diameter extent will be affected by viscous effects. Therefore, the core flow size, ϕ, is calculated based upon the thickness of the boundary layer after it has grown through the entire length of the acceleration section

$$\phi = 6 - 2\delta_{x=3.96m} \tag{3.19}$$

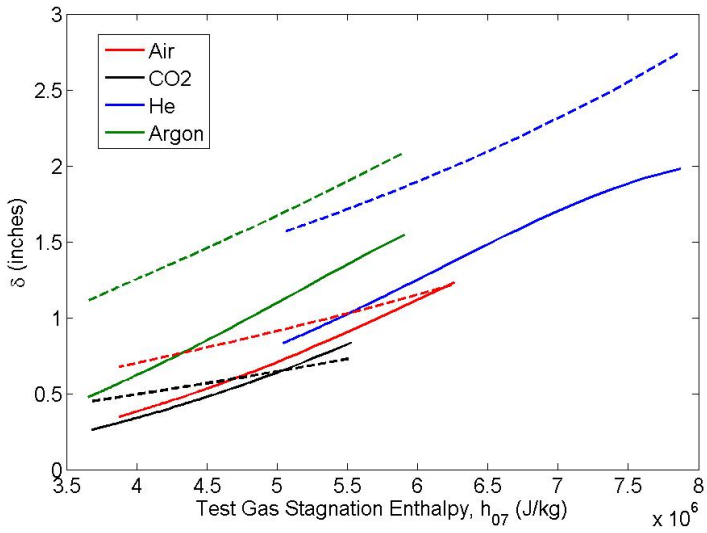

Figure 3.3: For a CO_2 test gas, laminar (solid) and turbulent (dashed) boundary layer thickness predictions at the tube exit versus test gas stagnation enthalpy. Four different acceleration gases are considered. p_1=1.5 kPa and p_4=2500 kPa. Perfect gas and ideal shock assumptions.

At hypersonic speeds, boundary layer thicknesses are larger than those at slower speeds. Viscous dissipation occurs as the very high freestream kinetic energy is partially converted to thermal energy within the boundary layer, increasing the temperature and also the viscosity - causing a thicker boundary layer. For a constant pressure profile (at a given axial location) within the boundary layer, the increase in temperature through the ideal equation of state will cause a decrease in density. In order to pass the same mass flow rate through a region of decreased density, the thickness must grow.

Laminar and turbulent boundary layer thicknesses at the tube exit (inside the test section) were calculated using Mirel's theory for a carbon dioxide test gas, Figures 3.3. The boundary layer thicknesses are presented as a function of test gas stagnation enthalpy. In these calculations, four different acceleration gases were considered for the given test gas. For a desired stagnation enthalpy, plots of this form will aid the test condition selection process as they indicate which choice of acceleration gas will result in the largest core flow.

Three test conditions were examined to test the veracity of Mirel's theory for boundary layer thickness in the HET. The test conditions were RC5, the CO_2 run condition used for

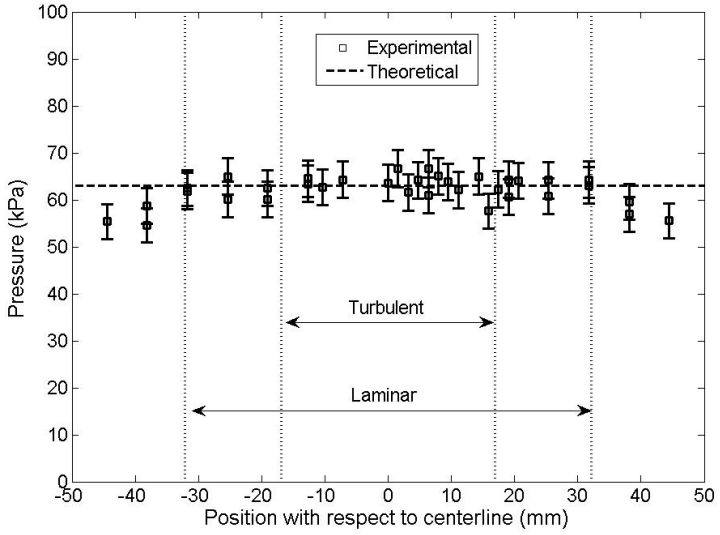

Figure 3.4: Pitot pressure survey for a high-enthalpy air run condition, Air-1, with p_4=4400 kPa, p_1=1.5kPa and p_5=175mTorr. Core flow sizes for both laminar and turbulent boundary layers using the theory of Mirels are also shown.

the MSL study described in Chapter 5, Air-1, a high-enthalpy air test gas case, and Air-3, which is a mid-range enthalpy air condition. Air-1 is a very similar run condition to the Air-5 condition used in the spectroscopy work of Chapter 4. Air-1 differs from Air-5 only in driver pressure, p_4, for which an appreciable difference in pitot pressure, but negligible difference in core flow size, is predicted. Table 3.4 compares the calculated laminar and turbulent core flow predictions with the experimental measurement. The experimental core flow uncertainty is +0 and -0.5 inches, accounting for 0.25 inch vertical accuracy on the sting. Entrance into the boundary layer from the core flow via traversing the pitot probe was taken to be the position at which a 15% reduction in measured pressure below the mean value occured. The pitot pressure survey for the Air-1 condition is shown in Figure 3.4, which visually illustrates the excellent agreement between experiment and Mirel's laminar theory and the drop in pitot pressure within the boundary layer.

Of particular interest in the table, we see that the laminar prediction best matches the experimental measurement for the high Mach number air case (Air-5) while a turbulent boundary layer exists for the low Mach number air (Air-3) condition. The unit Reynolds

Condition	Test Gas	Re_u (1/m)	M_7	$\phi_{laminar}$ (in.)	$\phi_{turbulent}$ (in.)	Exp. (in.)
Air-3	Air	9.80×10^5	4.96	3.92	2.6	3.0
Air-1	Air	5.50×10^5	7.42	2.53	1.33	2.5
RC5	CO_2	1.00×10^6	5.72	4.15	3.93	4.5

Table 3.4: The laminar and turbulent core flow predictions, based upon Mirel's theory, for three different run conditions. Theoretical values are compared against experimental measurement. Error bars on experimental values are +0 inches and -0.5 inches.

number, Re_u, of the Air-3 condition is roughly double that of Air-5. As Re is the established parameter for transition, one would expect an Air-3 boundary layer to undergo laminar-to-turbulence transition earlier than for Air-5. Additionally, the higher the value of the freestream quantity, U^2/ν, the lower the importance of higher modes obtained from a linear stability analysis [51]. In comparison to wind tunnels, this quantity will be at least an order of magnitude higher for impulse-type facilities, such as the HET, where freestream velocities replicative of hypersonic flight conditions are obtained. As such, experiments in perfect-gas facilities such as at M6NTC [52] and BAM6QT [53, 54] have identified the second mode as the most dominant mode, while they may have little relevance to transition at flight velocities [51]. Mack showed that with increasing freestream Mach number, the maximum spatial amplification rate of the first mode decreases [55]. Therefore, it is very likely that first mode instabilities are dominant within HET flows so that boundary layer stability is promoted with increasing Mach number.

3.4 Conclusions

Attempts have been made to provide a more rigorous characterization of the test condition in terms of test gas noise levels and the size of the core flow. These features were previously determined via experimental measurement which was very time-consuming and an inefficient method for the test condition selection process. The ability to now predict core flow size, coupled with a comparative basis for test gas noise levels, will significantly reduce the time

taken for this process. All previous theoretical calculations within the HET assumed inviscid flow, however this study extends the analysis towards viscous effects.

Perfect gas analysis has been completed to identify parameters which correlate with observed levels of test gas noise across a variety of run conditions. Two parameters were investigated: the Atwood number and the characteristic acoustic impedance. Noise level was quantified via the standard deviation of test gas pitot pressure. It was seen that the Atwood number, and hence any hydrodynamic instability resulting from pressure and density gradients across the secondary diaphragm, is not a successful indicator. A parameter, describing the ratio of acoustic pressure amplitude to the overall pressure field, correlates very well with test gas noise levels. The ratio is dependent upon the total characteristic acoustic impedance across the initial secondary diaphragm.

Core flow size has been estimated using the theory of Mirels, which predicts growth of the boundary layer after the transmitted shock and limits the size of the test gas core flow diameter. The influence of the acceleration gas and test gas stagnation enthalpy upon this core flow size has been investigated. Theoretical predictions have been compared with experimental data, for which the agreement is quite good for two conditions but is limited in the other instance due to experimental uncertainty arising from insufficient measurement spatial resolution.

CHAPTER 4

POST-SHOCK RELAXATION REGION VIBRATIONAL TEMPERATURE MEASUREMENTS

4.1 Introduction

Behind a strong shock, very high temperatures can occur which leads to considerable vibrational excitation and dissociation. The extent and profile of the post-shock relaxation region must be predicted to infer aerothermodynamic loads on the vehicle body. The complexity of a thermochemically active, hypersonic flow tests the current limits of computational modeling [56]. Experimental data, particularly obtained using non-intrusive techniques, are therefore valuable, but conditions are typically challenging for measurement diagnostics.

The goal of this study is to investigate the non-equilibrium relaxation region behind a normal shock using spectroscopic radiation measurements. By doing so, we aim to demonstrate the applicability of emission spectroscopy as a diagnostic for hypervelocity flows. The normal shock is created via a Mach reflection using an opposing wedge arrangement. The choice of a normal shock eliminates flow field complexities associated with a curved bow shock, such as mixed subsonic-supersonic regions, entropy gradients due to flow curvature and three-dimensionality. Nitric oxide A-X (also referred to as the gamma, or γ band) and hydroxyl radical A-X band transitions are used to measure post-shock vibrational temperature profiles in a high-enthalpy, nominal Mach 7.4 air flow.

NO and OH spectral data have previously been the focus of a series of sounding rocket flight experiments measuring ultraviolet emission behind a bow shock which were carried out in an effort to validate aerodynamic and radiative transfer models at re-entry conditions [57]. Single scans at 89.7 to 76.4 km were dominated by nitric oxide (A-X) gamma

band emissions. In contrast, the summed spectra at 100 km was dominated by hydroxyl (A-X) bands, primarily (1,0) and (0,0). Significant computational and theoretical analyses have been completed upon these data. Initially, the primary aim was to compare radiation model predictions with data based upon spectral emission obtained from four NO electronic bands [58, 59, 60]. With only A-X band radiation being observed for the OH molecule, focus then shifted to developing OH specific radiation models for comparison with the experimental data. Numerical investigations have been completed based upon these models including work completed by Levin et al. [61, 62, 63, 64, 65], Gimelschein et al. [66] and Kossi and Boyd [67]. In certain cases, significant differences were found between OH A-system vibrational temperature and those of the bulk flow. With outstanding issues arising from the flight experiments, one aim of this study is to provide additional temperature data behind hypersonic shock fronts with strong OH A-X emission at elevated temperatures.

In a partially dissociated and vibrationally excited freestream, Nerem et al. have measured relaxation times of dissociated air behind a normal shock for shock speeds between 4.9 to 6.8 km/s by examining the radiative emission time-history [68]. Vibrational temperatures and relaxation times behind normal shock waves, with shocked temperatures between 1400-3200K, were measured by Russo for CO test gas mixtures [69]. Time-resolved vibrational temperature measurements of CO were made using the emission band-reversal method and the line-reversal method for seeded sodium by assuming equilibrium between CO vibrational and sodium electronic temperatures. In the Mach range of 3.5-5.7, Moser and Hindelang measured nitric oxide vibrational relaxation times behind incident normal shock waves [70, 71]. Moser and Hindelang employed infra-red diode laser absorption spectroscopy tuned to specific ro-vibrational transitions for a NO-Ar gas mixture. At shock velocities of 6.2 km/s, Sharma and Gillespie conducted rotational and vibrational temperature measurements behind a normal shock [72], which sought to advance previous non-equilibrium relaxation region measurements by Allen et al. [73, 74, 75]. In each of these cases, nitrogen was the test gas. Sharma and Gillespie completed their measurements using photomultiplier tube radiometers

and the second positive system of N_2. Using the Marseille free-piston shock tube and a shock velocity of 5.8 km/s, Labracherie et al. studied the non-equilibrium region downstream of a normal shock wave [76]. Labracherie et al. presented the temporal evolution of vibrational and rotational temperatures and did not specifically investigate spatial temperature gradients. Temperature measurements were made for a methane-nitrogen-argon mixture using the CN B-X electronic transition. Using the spontaneous emission of the δ v =0 band of CN, Ramjuan et al. spatially measured the relaxation region behind a normal shock with a velocity of 5.6 km/s [77]. Recently, Rond et al. used the CN violet system to show time-resolved post-shock intensity profiles and to measure post-shock vibrational temperatures using emission spectroscopy [78].

These previous studies demonstrate that emission spectroscopy is a viable technique for determining internal energy mode temperatures within a non-equilibrium flow field. CO_2 flow fields were the focus of many of the experimental studies that utilized emission spectroscopy as the diagnostic technique and CN was the species of interest. In the current study, we examine air flows with NO and OH as the emitter species. Experimental results from CUBRC (Calspan University of Buffalo Research Center), for shock velocities between 3-4 km/s, used emission spectroscopy to identify the NO A-X band as the dominant radiator behind strong shocks for a O_2-N_2 gas mixture [79]. A follow-up experimental study used the region behind the shock wave to determine the squared transition moment value of the NO gamma band and to obtain time-dependent NO gamma radiative signals [80]. The calculation of internal energy mode temperatures using radiation signals from NO band systems via comparison with numerical spectra simulation has been successfully demonstrated on numerous occasions in air plasma experiments. In the NASA Ames 20 MW arc jet wind tunnel, vibrational temperatures have been measured by using the emission spectra of the NO γ (A-X) and δ (C-X) bands [81, 82]. In the same facility, rotational temperatures have also determined using the NO δ(0,4), γ(0,0), γ(0,1), γ(0,2) and γ(0,3) bands [83]. Using strong γ and weaker β (B-X), δ and ϵ (D-X) band transitions, all internal energy mode

temperatures were measured for plasma discharges in air [84].

In the previous shock wave studies, measurements have been made behind propagating waves. In the present experiments, we instead establish a stationary shock using an opposing double wedge model geometry. The flowfield is first visualized using the schlieren technique. Shock angles are measured and since the free stream inflow conditions are known, the frozen post-shock state is well-characterized.

The shock-tube was almost exclusively the only type of impulse facility used in the previous experimental studies discussed above. In reflected-shock tunnels, chemical freezing within the nozzle and freestream non-equilibrium effects can alter the test gas [1, 85, 86]. An expansion tube is an alternate means of achieving high-enthalpy hypersonic conditions. Therefore, this work also serves as a testbed for demonstrating the applicability of emission spectroscopic techniques for temperature measurement within an expansion tube. Emission spectroscopy can provide useful data for facility characterization. At the TCM2 free-piston shock tunnel in France, emission spectra have been used to calculate useful test times and demonstrate test time homogeneity for different operating conditions [87, 88]. Test time determination and species identification in the JXI expansion tube facility using emission spectroscopy was performed by Ramjuan et al. [89]. Expansion tubes typically exhibit shorter test times than those exhibited in shock-tube and arcjet wind tunnel facilities, which reduces the emission signal strength. To the knowledge of the authors, this is the first study to conduct vibrational temperature measurements using optical emission spectroscopy in an expansion tube.

4.2 Experimental Setup

4.2.1 Imaging System and Spectroscopic Setup

Mach reflection configurations were visualized using a schlieren system consisting of a Xenon nanopulser (10 ns duration) white light source and pco.1660 (Cooke Coorporation) CCD camera. The system is triggered via the transmitted shock arrival at a 1MHz response pitot

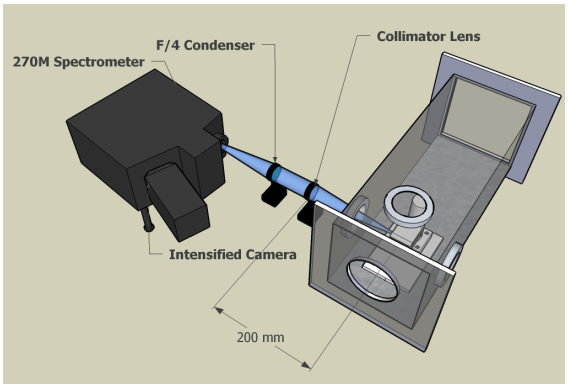

Figure 4.1: Three dimensional schematic of imaging spectroscopy collection system

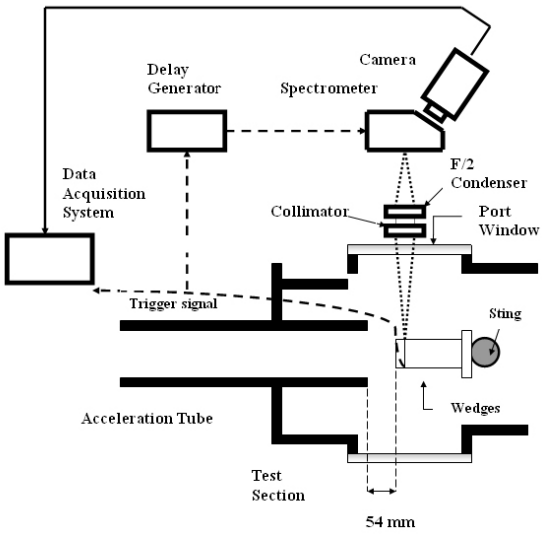

Figure 4.2: Schematic of experimental data acquisition setup

pressure transducer (PCB 113A26) sting-mounted in the test section 31.75 mm below the model centerline. Schlieren images and pitot pressure traces from previous experiments [25] and simulations [90] ensure a repeatable and steady Mach reflection during the test time.

For the spectroscopic measurements, the broadband emission light is collected and collimated at 90 degrees to the vertical axis plane of the test section with a 200 mm focal length, 50.8 mm diameter (f/4) UV coated lens. The collimated light is then focused for an imaging spectrograph. Figure 4.1 is a three dimensional rendering of the experimental setup and Figure 4.2 is a schematic of the triggering system. Two spectrographs were used in this study: a f/2 CP140 Jobin Yvon spectrograph for measurements which will be referred to as "coarse",

and a f/4 270M SPEX spectrograph for measurements which will be referred to as "fine". Spectral lines were visualized using a Princeton Instruments PI-MAX MG:512SB intensified CCD camera system and a ST-133 camera controller. For each run, the camera exposure was set to 80 μs in order to capture as large a portion of the test gas as possible without accelerator or driver gas contamination. For the f/4 270M SPEX spectrograph measurements, a slit size of 43 μm was selected as a compromise between signal strength and resolution. At the focal plane of the spectrometer for the fine measurements, the dispersion across the chip was 0.07nm/pixel, corresponding to a wavelength range of 35.71 nm. The measured resolution is 1.4 Angstrom. For the coarse measurements, two different slit sizes of 25 and 50 μm were used. For the NO wavelength and intensity calibration, a hollow cathode Fe lamp and a L6302 D2 Hamamatsu lamp with Oriel 6310 power supply are used respectively. For the OH wavelength and intensity calibration, an Oriel pencil style 6035 Hg-Ar lamp with a 6045 power supply and a 20W Newport 6319 tungsten lamp with a Oriel 68735 power supply are used respectively. For the coarse resolution results, for which no intensity calibration was performed, the 6035 Hg-Ar pencil lamp was the wavelength calibration source.

While emission spectroscopy is referred to as a point measurement, a finite collection volume does exist. In order to determine the one-dimensional (in the axial direction) extent of this imaging point, a calibrated point source was mounted on a translation stage and traversed slightly upstream and downstream while the intensity was recorded. The FWHM of the recorded intensity profile is 1mm with an uncertainty of $\pm$ 0.25mm. As with the schlieren system, spectrometer acquisition sequences were triggered using the transmitted shock arrival at the test section pitot probe which was located within the core flow, 31.75 mm below the tube centerline [25].

4.3 Thermochemical calculations

The experimental results are compared with calculations using an existing thermochemical model [91], based on the semi-classical, forced harmonic oscillator model with free-rotating (FHO-FR) molecule paths by Adamovich and co-workers [92, 93, 94]. The molecule-molecule rates of Adamovich [94] are extended to higher collisional energies by a curve fit function obtained by minimizing the deviation from the numerical integration of the transition probability over all possible O_2, N_2 and NO transfers. The three-dimensional collisional model of Adamovich and Rich [92] is used for the molecule-atom rates. State-resolved chemical reaction rates are taken from Bose and Candler [95, 96]. Boltzmann distributions are assumed for NO produced by the first Zeldovich reaction. However, non-Boltzmann distributions are modeled for NO produced by the second Zeldovich reaction [96]. Using the master equation approach of Park [86], a total of 37, 48, and 40 vibrational levels for O_2, N_2, and NO respectively are obtained in addition to monatomic O, N, and Ar, resulting in a 128 species mixture. The extended thermochemical model has been previously validated by comparison with experimentally obtained data for rate constants [97, 98], vibrational relaxation times [99, 100], dissociation rates [101, 102] and V-V transfer probabilities [103]. Initial inflow conditions for the calculations (static pressure, static temperature and test gas Mach number) are obtained from inviscid, perfect-gas calculations of expansion tube operation.

4.4 Results

4.4.1 Test Gas Freestream Condition

Table 4.1 summarizes the test gas freestream condition with a comparison between experimentally measured values and inviscid, one-dimensional, perfect gas calculations. The experimental values presented are ensemble averaged across a total of 28 separate events, consisting of 20 experiments for NO spectra acquisition and 8 experiments for OH spectra

	M_7	$h_{o,7}$ (MJ/kg)	t_{test} (μs)	$p_{7,pitot}$ (kPa)	p_7 (Pa)	u_t (m/s)	u_7 (m/s)	u_s (m/s)	T_7 (K)	ϕ (mm)
Exp.	7.30	–	104	53.64±1.36	–	4148±47	–	2044±42	–	63.5
Theo.	7.42	7.88	163	55.6	778	5228	3777	1995	644	64.3

Table 4.1: Selected test gas freestream parameters. Theoretical calculations assuming one-dimensional, perfect gas dynamics are compared with experimental measurements. Subscript 7 denotes the test gas. M is the Mach number, T is the static temperature and h_o is the stagnation enthalpy.

acquisition. Across most of the test condition parameters the agreement between theoretical expectation and measurement is very good. The largest discrepancy is seen in the calculated and measured values of the transmitted shock velocity, u_t. However, two-dimensional Navier-Stokes simulations of a very similar run condition (Air-1) have shown that the transmitted shock is considerably attenuated due to viscous effects through the acceleration section [34]. Good agreement was obtained between the numerically predicted and the experimentally measured velocity. The previous run condition, Air-1, differs from Air-5 (condition used in the current study) only by the primary diaphragm burst pressure. Perfect gas predictions indicate that the transmitted shock velocity differs by only 1 % for the change in burst pressure. Therefore, u_t is assumed to be invariant with burst pressure and the calculated u_t over-prediction results from the inviscid, one-dimensional assumption. The experimental test gas Mach number is calculated from the measured pitot pressure, $p_{7,pitot}$, using the theoretical prediction of the static test gas pressure, p_7. Very low signal-to-noise ratios prevent experimental measurement of p_7 for the current run condition. Despite a lower than theoretically predicted test-time, a sufficient slug of test gas exists in which to make spectroscopic measurements.

4.4.2 Asymmetric Mach Reflection

The Mach reflection is created by an asymmetric wedge configuration. 25 and 35 degree half-angle wedges are used with a tip-to-tip separation of 25.4 mm. In order to avoid three-dimensional effects, inlet aspect ratios of 1.25 and wedge aspect ratios of 5 were used [104].

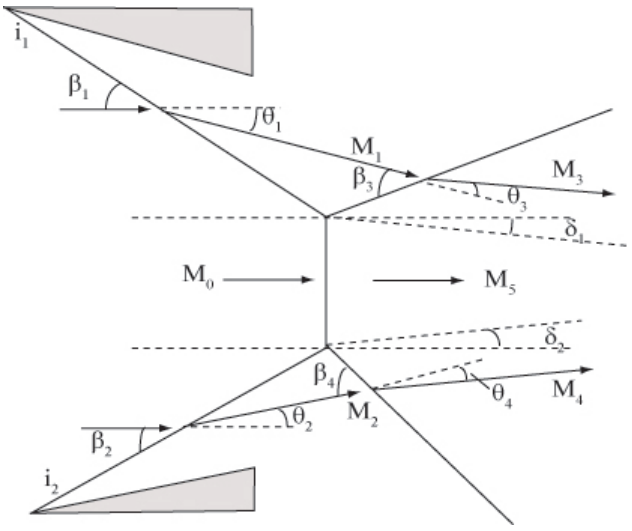

Figure 4.3: Schematic of an asymmetric Mach reflection.

Wedge angles were chosen based upon inviscid, perfect-gas shock-polar theory. Details of this approach can be found in Appendix A.2. CAD drawings of the wedges and mounting arrangements are included in Appendix B.

A detailed depiction of the Mach reflection geometry is provided in Figure 4.3. The Mach reflection consists of incident and reflected shock waves and a Mach stem. The Mach stem connects two triple points and each triple point has a corresponding slipstream. Following the nomenclature of the figure, assuming an inviscid flow and an infinitely thin contact surface, the boundary conditions for a Mach reflection are [105]:

$$\theta_1 - \theta_2 = \delta_1 \tag{4.1}$$

$$\theta_2 - \theta_4 = \delta_2 \tag{4.2}$$

The Mach reflection (MR) has been extensively studied throughout the literature as an example of a shock-shock interaction which occurs extensively in aerodynamic applications. With significant thermochemical effects present in the current study, it is important to characterize their anticipated influence upon the Mach reflection configuration. Numerous previous studies have confirmed that the overall MR configuration is displaced forward and the

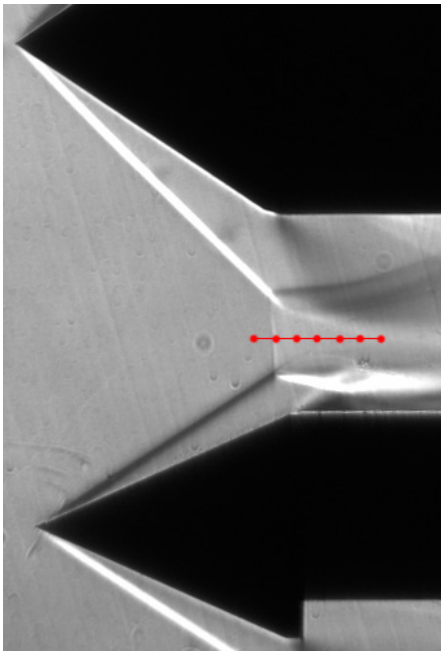

Figure 4.4: Schlieren image of an asymmetric Mach reflection in Air-5 test condition, nominal freestream Mach number of 7.42. Wedge tip-to-tip spacing is 24.5 mm. Emission spectroscopy measurement locations are indicated.

Mach stem height is decreased in the presence of non-equilibrium effects [106, 107, 108, 109]. The Mach stem height reduction increases the experimental difficulty as the post-shock measurement area is also decreased. Numerical simulations of the current asymmetric wedge arrangement indicate that the flow field is significantly dependent upon the thermochemical model [90]. Frozen, finite-rate and equilibrium models were examined, for which the finite-rate simulation provided the best agreement with experiment. However, the simulation predicted a slightly further recessed and longer Mach stem than experimentally observed. The simulations also indicated that the Mach stem position is stationary 20 μs after the passing of the contact surface. For a test gas duration of approximately 120 μs this, combined with a consistent triggering event, confirms that a steady Mach reflection exists during data collection.

A sample schlieren image of the Mach reflection is included, Figure 4.4. The MR configuration geometry has been verified via measurement of shock angles from the schlieren images. The results are presented in Table 2 and compared against perfect gas predictions.

The subscripts refer to the Mach reflection schematic depicted in Figure 4.3. The theoretical reflected-shock angles were determined from shock-polar calculations. Comparisons yield very good agreement between incident shock angles. The differences observed for the lower triple-point reflected-shock and slipstream angles are more pronounced, especially so for the slipstream angle. Whilst the static test gas temperature has not been directly measured, the agreement between test gas pitot pressure, test gas Mach number, primary and transmitted shock speeds and incident shock angles suggests that freestream conditions are well-predicted by perfect gas theory.

From schlieren images, the Mach stem is measured to be 3.9 mm high, almost perpendicular, located 12.7 mm downstream of the wedge tip plane and its centerline located 2 mm below the tube axial centerline. As Figure 4.4 shows, the uniform region behind the Mach stem which is not influenced by the converging shear layer slipstreams is very small (approximately 5 mm). It is therefore imperative that the spatial locations of the spectra collection points are known very precisely with respect to the wedge tip plane. This involves determining the repeatability of the Mach stem location and potential shift from experiment-to-experiment. The deviation on both height and location measurements was found to be ± 0.5 mm. With an uncertainty of ± 0.25 mm in the imaging location (see Section 4.2.1) this results in a combined spatial uncertainty of ± 0.75 mm. Repeat experiments show the movement of the Mach stem is small enough with respect to the uniform region length and the Mach stem height such that the calibration imaging point (acquired before the experiment) corresponds to the same location within the flowfield during the experiment. Measurements were made along the Mach stem centerline at -1, 0, 1, 2, 3, 4 and 5 mm downstream of the Mach stem, locations indicated by the symbols in Figure 4.4.

Calculations of the expected species concentrations and temperatures in the post-shock relaxation region were carried out using the thermochemical model discussed in Section 4.3, and are presented in Figures 4.5 and 4.6. These figures demonstrate the chemical and thermal non-equilibrium nature of the flow field. The mole fraction profiles up to 5 mm downstream

Shock Angles (degrees)	Theory	Exp.
β_1	46.6	44.4±0.3
β_2	33.0	32.5±0.3
β_4	40.6	45.1±0.3
δ_2	-7.4	-2.7±0.3

Table 4.2: Comparison between theoretical and experimentally measured Mach reflection shock and shear layer angles.

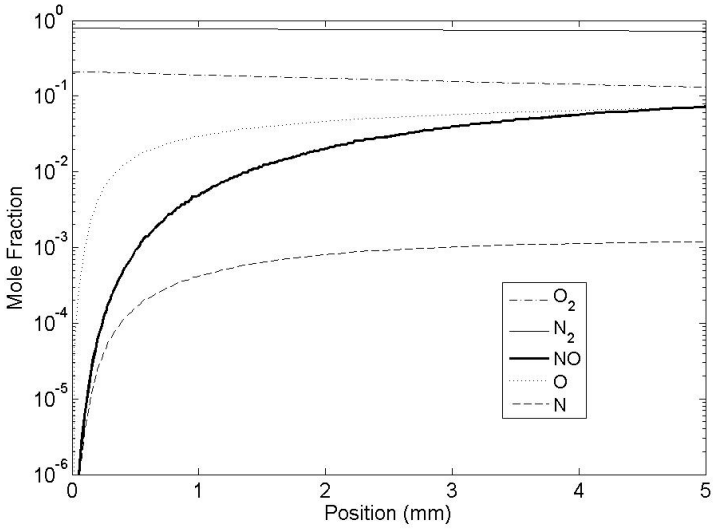

Figure 4.5: Calculated mole fraction distributions for the 5 major species up to 5 mm downstream of the Mach stem.

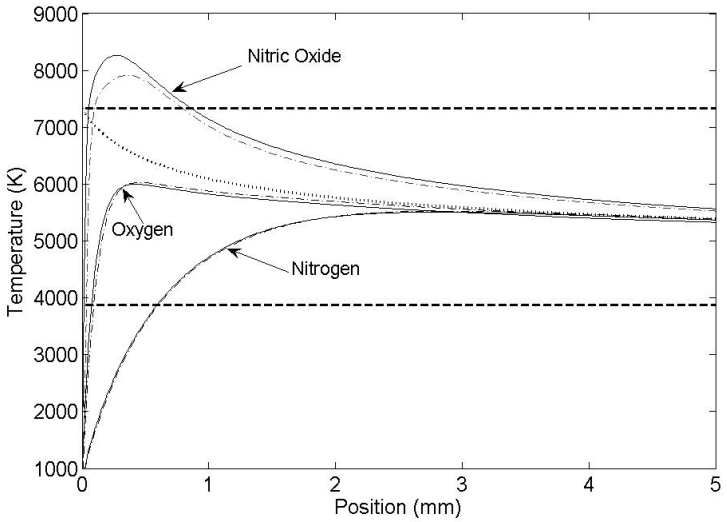

Figure 4.6: Temperature profiles up to 5 mm downstream of the Mach stem. In this figure, the dotted line (thin) represents the translational temperature, the solid (thin) lines represent the equivalent vibrational temperatures of each species and the dash-dotted (thin) lines represent the A-state vibrational temperatures. The upper and lower dashed (thick) lines show the frozen (7332 K) and equilibrium (3872 K) temperatures respectively.

of the Mach stem for the 5 major species considered in the model, NO, O_2, N_2, O and N, are shown in Figure 4.5. The results predict dissociation behind the normal shock with the presence of NO, O and N. Figure 4.6 displays the translational temperature, and the equivalent [91] and A-state vibrational temperatures for NO, N_2 and O_2 calculated along the centerline of the Mach stem up to 5 mm downstream of the Mach stem. The frozen and equilibrium temperatures are calculated to be 7332 K and 3872 K respectively. The A-state vibrational temperature (described as the first vibrational temperature in the Massa and Austin paper) is calculated according to

$$\frac{e_1 - e_0}{k \log\left(\frac{N_0}{N_1}\right)} \tag{4.3}$$

where N and e denote the mole numbers and energies for the subscripted levels respectively and k is the Boltzmann constant [91]. The NO temperatures initially overshoot the frozen temperature. This behavior is associated with the formation of NO in a non-Boltzmann

distribution via the second Zeldovich reaction [95, 96]. NO also exhibits the largest difference between the equivalent and A-state vibrational temperatures.

4.4.3 Species Identification

A spectrum obtained 10 mm downstream of the Mach stem over the wavelength regime of 200-400 nm using the f/2 CP140 Jobin Yvon spectrograph is shown in Figure 4.7. Coarse resolution acquisition was initially undertaken as a means of identifying potential temperature-measurement appropriate species. Only the 50 μm results are presented since this resolution provided the largest intensity levels (a 25 μm slit was also used). The identified emitters with temperature-fitting potential in this wavelength regime are NO, OH and N_2^+. Emission from the OH radical has the strongest signal and dominates the entire spectrum. Certain portions of the spectrum are magnified in order to show the presence of N_2^+ and NO. Based on these results, the decision was made to concentrate efforts for temperature measurements upon the ultraviolet portion of the spectrum using OH and NO. Additional measurements also detected no noticeable signatures in the visible region.

OH is present in the flow field due to moisture contamination in the air test gas. As discussed in Section 4.1, NO and OH spectral data have previously been the focus of a series of flight experiments measuring ultraviolet emission behind a bow shock. Calculations for these experiments showed the presence of trace amounts of water vapor did not affect the density, temperature, and major species (N_2, O_2, NO, N, O) concentrations behind the shock [58]. In the present work, to check the presence of water vapor or associated radical species had no measurable effect on the temperature measurements, experiments were carried out with both dry (bottled) and moist (room) air.

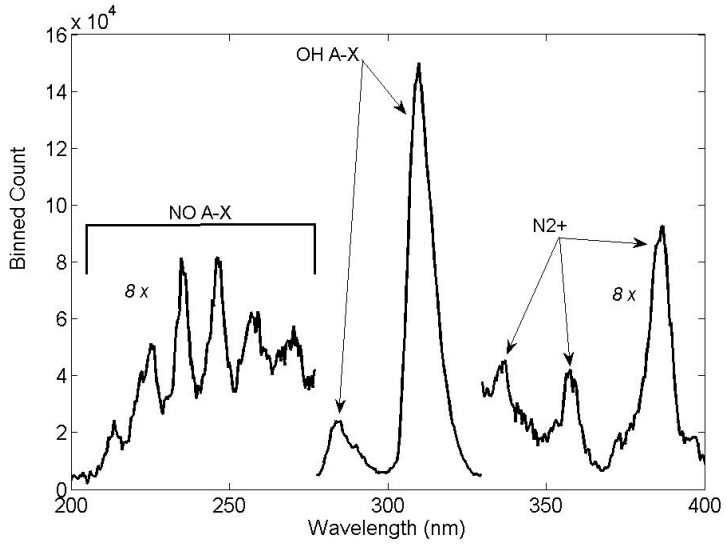

Figure 4.7: Spectrum obtained 10 mm downstream of the Mach stem with a 50 micron slit and 50 microsecond exposure time with certain portions of the spectrum magnified.

4.4.4 OH results

Due to the strong signal strength, initial measurements were conducted using the emission spectra of OH. The OH A-X band calibration setup was also easier to implement than the NO A-X band as a traditional blackbody radiation source with analytical solution could be used. The location of data collection with respect to the Mach reflection are shown in Figure 4.4. No signal was observed at the -1 mm location upstream of the Mach stem.

Fine-scale spectra were collected and temperature fits constructed for the $A^2\sum^+ \rightarrow X^2\prod$ electronic transition in the 307-320 region. An example of an emission spectrum for the OH A-X band obtained 4 mm downstream of the Mach stem is shown in Figure 4.8. Simulated and experimentally observed spectra are compared. At each axial location, LIFBASE [110] was used to generate simulated spectra across a broad temperature range at coarse temperature increments of 100 K using Lorentzian profiles and a resolution of 0.14 nm. Wavelengths were interpolated so that the LIFBASE data points matched up with the experimental points and at each temperature increment a scaling factor was computed which reduces the residual, a value defined to be the sum of the differences between experimental and predicted intensity peak values across the entire spectral range. The smallest residual of the entire tempera-

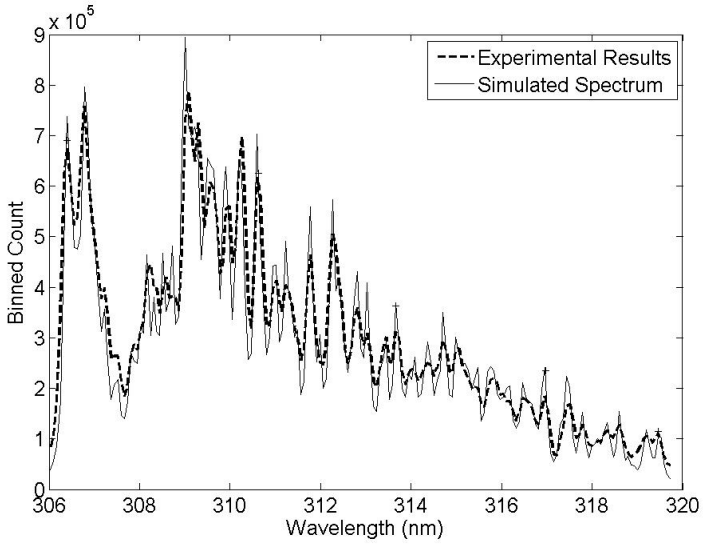

Figure 4.8: Simulated LIFBASE and experimental OH spectra obtained 4 mm downstream of the Mach stem for a vibrational temperature of 4140K.

ture range provided the fit vibrational temperature. The rotational and translational energy modes are assumed to be in equilibrium. Once the coarse temperature was determined, further optimization was performed such that the final temperature increment was 20 K. This final simulation uncertainty of 20 K is deemed appropriate as it is small compared to typical temperature uncertainty values arising from the major sources of experimental error (see Section 4.4.6), independent of the spatial location of the measurement. As shown by Figure 4.8, the results indicate that the intensities across the entire spectrum match up very well and that reasonable temperature fits have been achieved. Spectra collected at 1 mm upstream of the Mach stem yielded no signal, confirming the spatial precision of the imaging location technique and lack of freestream dissociation in the facility.

4.4.5 NO results

Experiments were undertaken in order to investigate the NO γ band. Since this is a non-equilibrium flow field, it should be noted that there are multiple vibrational temperatures

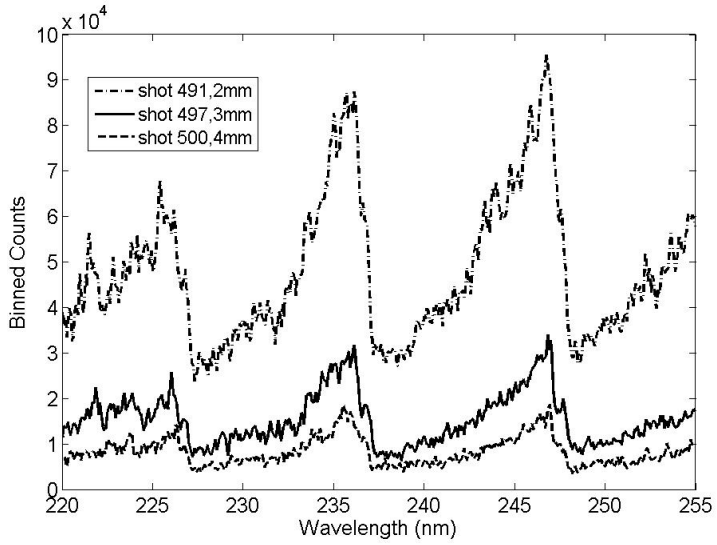

Figure 4.9: NO γ band spectra obtained at three different locations (2, 3 and 4 mm) downstream of the Mach stem.

associated with the different electronic states of the nitric oxide molecule. Figure 4.9 is an example of three NO spectra at three different streamwise locations of 2,3 and 4 mm downstream from the Mach stem. The signal strength is observed to attenuate markedly with increasing axial distance.

Spectral fitting to the NO data using LIFBASE yielded very high temperatures, possibly due to the LIFBASE rotational and vibrational quantum number limits of 80 and 5 respectively. The Figures 4.11 and 4.10 provide rotational and vibrational Boltzmann population distributions respectively for the two diatomic molecules up to the LIFBASE limits. As a means of providing expected distributions, the NO temperature used for the calculations corresponds to the temperature predicted by the thermochemical model. The OH temperature is on the order of the fitted OH A-X band vibrational temperatures. These figures indicate that the NO distributions are considerably broader than their OH counterparts and reveal that non-negligible Boltzmann rotational and vibrational populations exist for NO above the LIFBASE limits.

Hence, an in-house algorithm developed by Glumac with user-defined maximum limits was used to generate simulated spectra. Vibrational and rotational energies are deter-

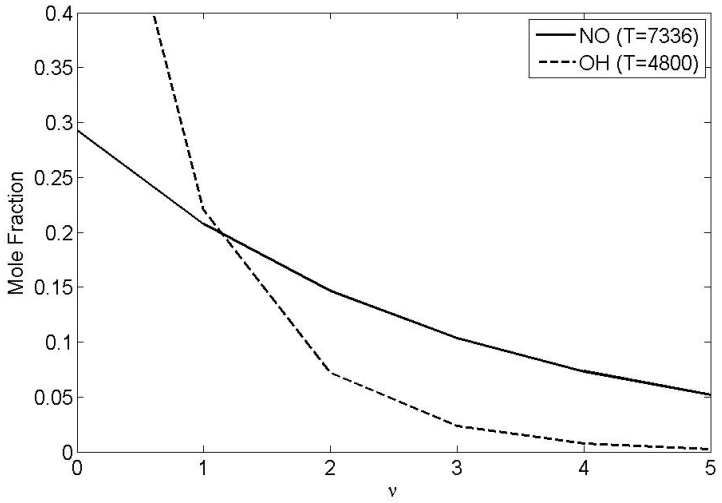

Figure 4.10: NO and OH vibrational population distributions at expected molecule vibrational temperatures

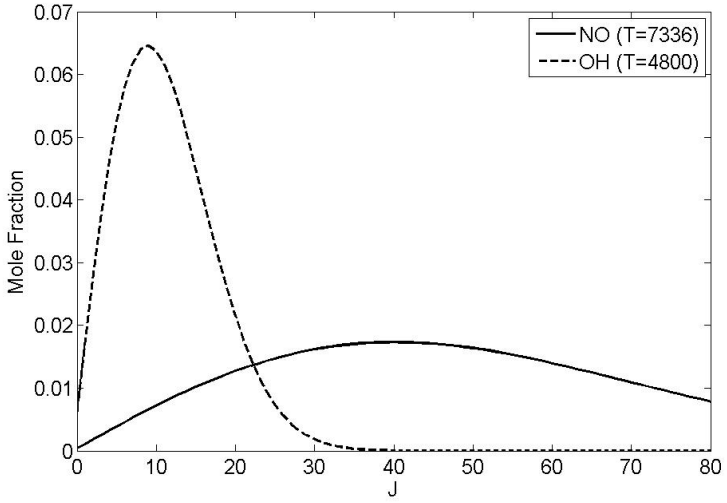

Figure 4.11: NO and OH rotational population distributions at expected molecule vibrational temperatures

mined to the third and second-order respectively via Dunham-type potential expansions. For consistency, the spectroscopic constants used in these expansions are taken as those from LIFBASE [110] and are summarized in the Appendix. For the doublet ground state, the lower and upper configuration energies are calculated using the analytical expressions of Kovacs [111]. The dependence of the spin-orbit parameter, A, upon the vibrational quantum number is taken from Amiot [112]. Line strengths were calculated via multiplication of the Franck-Condon factors and the Hönl-London factors. The Hönl-London factors for the doublet transitions were determined following the expressions of Kovacs [111] and the Franck-Condon factors were taken from Ory et al. [113]. Conversion from vacuum to air wavelengths is achieved via the Edlen formula. The LIFBASE simulation formulates emission intensity as a function of molecule lifetime, emission co-efficients and predissociation rates. LIFBASE calculates the emission co-efficients by incorporating the Hönl-London factors and the transition probabilities that are calculated using the Rydberg-Klein-Ress (RKR) method. The predissociation phenomena has been observed for the NO γ band and has been experimentally [114], theoretically [115] and numerically [116] shown to be dependent upon both vibrational and rotational quantum numbers. Vibrational levels of v′=4 and 5 can predissociate and for v′=3, rotational levels above N′= 25 can predissociate [114]. However, for the most part transitions from these levels result in energies outside the current wavelength regime. As identified by Figure 4.12, the dominant vibrational transitions which weigh heavily upon the temperature-fitting procedure will not predissociate as explained above. Furthermore, LIFBASE simulations for 220-255 nm show no difference between spectra with and without predissociation broadening. Therefore, predissociation is not considered to be a phenomena which needs to be considered for the wavelength range of interest.

Figure 4.12 shows a comparison between LIFBASE and an in-house simulation for a temperature of 6200 K for limits of ν_{max}=5 and J_{max}=80 (limits inherent to LIFBASE). The major vibrational band transitions are also indicated. The spectra are normalized by the maximum intensity in each case, which corresponds to the (0,1) peak value. The agreement

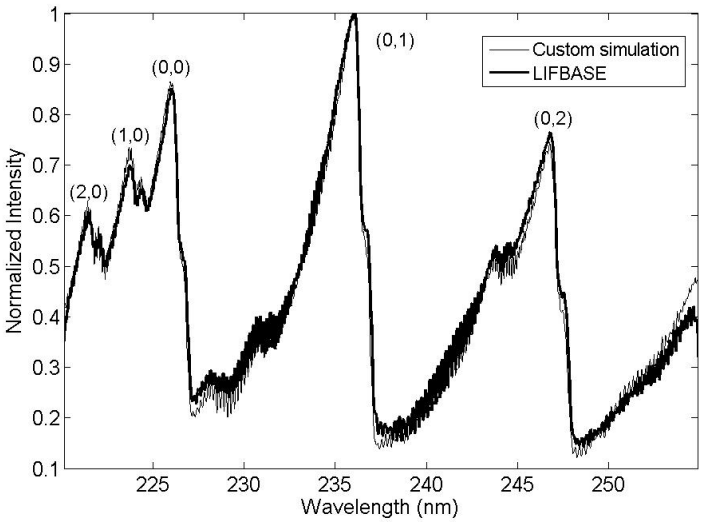

Figure 4.12: Comparison between simulated spectra using an in-house developed algorithm and LIFBASE for an A-state vibrational temperature of 6200 K. ν_{max}=5 and J_{max}=80. The major vibrational band transitions are indicated.

between the two simulations is very good and within the experimental spectral resolution. Figure 4.13 shows a comparison between the two in-house simulations, one with the lower limits of ν_{max}=5 and J_{max}=80 and the other with the extended limits of of ν_{max}=20 and J_{max}=250. As evident in the figure, the use of the extended limits alters the intensity distribution across major portions of the spectrum. The extended vibrational limits (and hence larger Δv values) will not influence the simulated spectrum, however the modeling of extra rotational levels will alter the spectrum within the 220-255 nm range. Since the intensity distribution is the optimization parameter for the temperature-fitting procedure, the inclusion of additional limits via the in-house simulations is justified. For a more detailed discussion of the in-house simulation program, please see Appendix A.3.

Fine-scale spectra were collected and temperature fits constructed for the NO $A^2\sum^+ \rightarrow X^2\prod$ electronic transition in the 220-255 nm region using the extended limits. The temperature fitting procedure was the same as described for the OH A-X transition. NO spectra were collected at 1, 2, 3 and 4 mm downstream of the Mach stem. Further downstream spectral acquisition of the relaxation region was restricted by the influence of converging

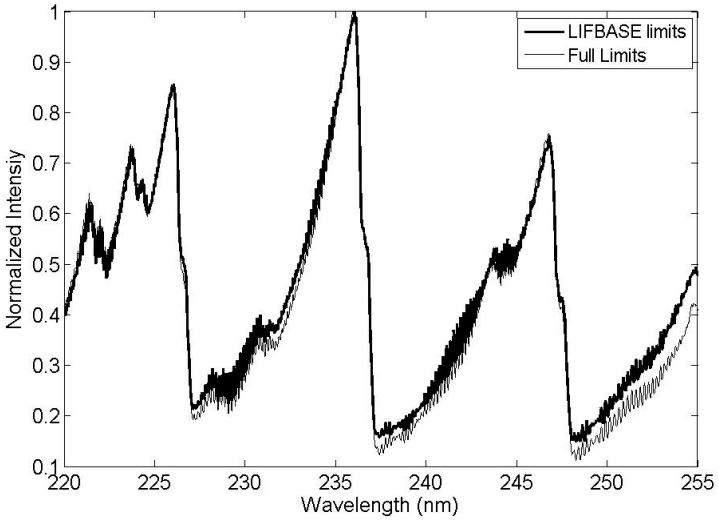

Figure 4.13: Comparison between the results of two simulated spectra using an in-house developed algorithm, one with ν_{max}=5 and J_{max}=80 (limits inherent in LIFBASE) the other with the extended limits of ν_{max}=20 and J_{max}=250.

shear layers bounding the measurement region, as shown in Figure 4.4. A sample spectrum, collected at 2 mm behind the Mach stem, is shown in Figure 4.14 along with the simulated comparison. The vibrational temperature in this case was determined to be 6900 K. Using the LIFBASE limits, the calculated vibrational temperature was 7600 K. As exhibited for all imaging locations, the NO spectra are somewhat noisy and the visual fit fidelity is not as pronounced as in the OH spectra. As shown in Figure 4.14, the major vibrational band transition intensities are all accurately matched.

The potential of contaminant emission within the 220-255 nm range was further investigated. Previous spectroscopic measurements at the TCM2 hypersonic facility have highlighted the importance of reducing test gas contamination. Pilverdier et al. noticed that a Mylar secondary diaphragm displayed significantly less emissive intensity than one made from copper [87]. The HET facility operates with a Mylar diaphragm. Ramjuan et al. also emphasized the importance of cleaning the facility [89]. As a result, before each shot both the driven and accelerator section were cleaned. No differences in the nitric oxide spectra were observed.

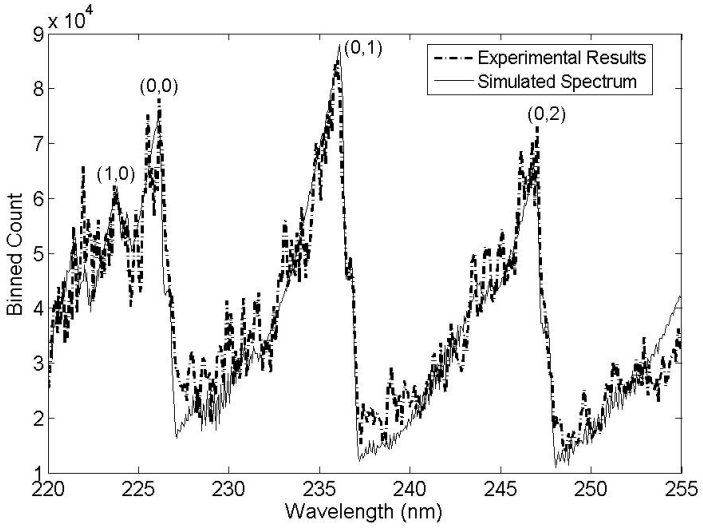

Figure 4.14: Simulated and experimental NO spectra obtained 2 mm downstream of the Mach stem for an A-state vibrational temperature of 6900K.

Dry air was also used as the test gas in order to see if the trace quantities of water vapor were affecting the results. The test location 2 mm behind the Mach stem was used to determine the influence of the moisture within the air. At this location five room air shots and six dry air shots were conducted and the temperatures determined. The standard deviation of these determined temperatures was 320K and 140K for the room air and dry air runs respectively. Despite the improvement in shot-to-shot repeatability with dry air as the test gas, no marked change in the experimental spectra was observed. Previous studies had identified O_2 Schumann-Runge band radiation within the NO γ band emission, however its presence was not seen to influence the measurement [79, 80]. Irregardless of any contaminant source, the intensity of the NO emission dominates the spectrum and is significantly greater than the contaminant signal. Therefore, as the temperature fitting procedure uses intensity peak values as the main optimization parameter, the contaminant signal is not sufficient enough to hamper the temperature calculation.

Experimentally measured NO vibrational temperatures are shown in Figure 4.15. Data are obtained from three experiments each at 1, 3 and 4 mm and six experiments at the 2 mm location. The repeatability of the measurements is good. The temperature profile

calculated using the thermochemical model detailed above is also shown. Very good agreement is achieved between calculated and experimentally measured vibrational temperatures across the relaxation region. The largest discrepancy is observed at the 2 mm location, while the temperature measurements at the other three locations are all within experimental error. The equilibrium temperature for this test condition (assuming a nitrogen, oxygen and argon air mixture) is calculated to be 3872K from the NASA CEA program [117]. Table 3 compares the ensemble average of the temperature measurement at each location versus the numerical result.

Results from the OH temperature fits described above are also presented on the same graph. The OH vibrational temperatures are considerably lower than those of NO and the temperature gradient throughout the relaxation region is much less pronounced and accompanied by a faster relaxation rate. OH error bars are not presented as no thermochemical calculation was conducted and hence no temperature gradient was available. The disparity between the experimentally measured OH and NO vibrational temperatures is indicative of the non-equilibrium flow field. The deviation from equilibrium of each of the two species depends on the specificity of the reactions that lead to their formation. As discussed in Section 4.1, OH A-X band vibrational temperatures calculated from OH radiation models have previously been reported to differ substantially from bulk vibrational temperatures. For example, Levin et al. calculated the peak stagnation line vibrational OH A-state temperature to be 2-3 times greater than the bulk flow vibrational temperature [61]. Kossi and Boyd also found considerable differences between the vibrational temperatures of the bulk flow and those calculated from an OH A-X radiation model [67]. The production mechanisms of OH and their impact on the vibrational temperature of the nascent species were found to be significant by Gimelshein et al [66]. Additionally, it was seen that even for a given production mechanism, different vibrational temperatures were predicted depending on the chemical reaction model [65]. These previous studies, together with the present work, indicate that while OH is an attractive species to probe due to its single, significantly excited state at these

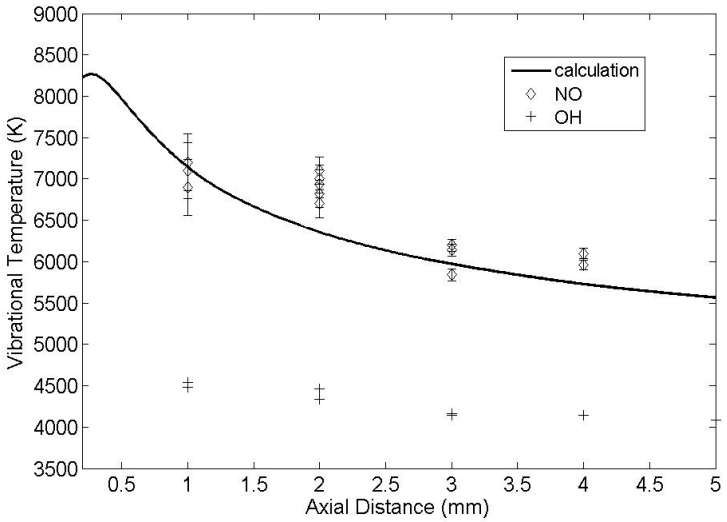

Figure 4.15: Experimentally measured NO and OH A state vibrational temperatures in the post-shock relaxation region. Measurements are compared to calculations using a detailed thermochemical model.

Distance (mm)	Numerical (K)	Experimental (K)
1	7143	7067
2	6356	6917
3	5971	6060
4	5721	6007

Table 4.3: Comparison between averaged experimental values and numerical results at different locations behind the Mach stem.

conditions, there are challenges associated with its use in non-equilibrium flows. However, the presented OH results serve as useful comparative experimental data towards resolving these issues and verifying any OH inclusive thermochemical model.

4.4.6 Sources of Uncertainty

The temperature measurement sources of error arise from shot-to-shot variation in MR location, the spatial precision of the imaging location, test condition variability, spectroscopic resolution and the temperature increment selection of the fit to simulated spectra. The first two sources are dependent upon the relaxation region temperature gradient, which was

determined from numerical calculations. As described in Section 4.2.1 and Section 4.4.2, the uncertainties in the imaging location and MR movement are 0.25 mm and 0.5 mm respectively. The freestream static temperature was used as the parameter to gauge test condition variability. For the purpose of the uncertainty analysis, the freestream static temperature is taken to be only dependent upon the HET initial pressures. Theoretically, the freestream static temperature would also be dependent upon the section gas compositions. As discussed above in Section 2.1.2, the air leak-rate into the helium filled expansion section is negligible and hence will not influence the gas dynamic prediction. Moisture within the air is expected to have a negligible influence upon the air test gas and is also not considered. Driver pressures are so large (roughly 25 atm) that any residual air within the helium gas is completely negligible. Therefore, freestream static temperatures are taken to be dependent only upon the initial HET pressures. Table 4 presents the percentage breakdown of each uncertainty source. The temperature measurement error bars at each imaging location, ΔT, based upon the five uncertainty parameters described above is calculated using the following equation

$$\Delta T = \sqrt{\sum_{i=1}^{5} \left[\left(\frac{\partial T}{\partial x_i} \omega_{x_i} \right)^2 \right]} \tag{4.4}$$

where ω_{x_i} denotes the uncertainty in the measurement of a certain parameter, x_i. Values are presented as percentages of the total uncertainty. The largest contribution to the total uncertainty is due to the Mach reflection movement from shot-to-shot. Combined with the imaging location uncertainty, these two factors account for more than 70% of the total uncertainty at each spatial location.

Axial Distance (mm)	Spectrograph Resolution	Mach Reflection	Imaging Location	Test Condition	Temperature Increment
1	0.16	77.76	19.44	2.55	0.09
2	0.15	75.45	18.86	5.17	0.37
3	0.13	63.52	15.88	18.67	1.81
4	0.11	56.67	14.17	25.25	2.80

Table 4.4: Breakdown of the contribution of the different uncertainty sources at each spatial imaging location for the nitric oxide vibrational temperature measurements. Values are given as percentages of the total uncertainty.

CHAPTER 5

EXPERIMENTAL AND NUMERICAL INVESTIGATION OF HYPERVELOCITY CARBON DIOXIDE BLUNT BODY FLOWS

5.1 Flowfield Description

In high-enthalpy hypersonic flight, thermochemical relaxation times are typically comparable to flow residence times, leading to nonlinear coupling between chemical reaction, vibrational excitation, and fluid mechanics. In carbon dioxide flows which are relevant to Martian planetary entry, thermochemical effects are particularly significant and may potentially account for some recent anomalous results in blunt body shock layers.

The bow shock flowfield is complicated as it involves entropy gradients, mixed subsonic and supersonic regions and is three-dimensional. Here only the forebody is described as the current study is not concerned with any aftbody flow dynamics. A strong bow shock forms in front of any blunt-nosed capsule, with the shock stand-off distance defined to be Δ along the stagnation line of the shock layer. This shock stand-off distance is known to be sensitive to the thermochemical state of the region between the shock and the body [118, 119]. It therefore serves as an important experimentally measurable parameter in hypervelocity flowfields. Near the stagnation line, the flow will be subsonic due to the low curvature of the bow shock, but the flow accelerates as it moves away from the axis. Eventually, it will cross the sonic line and reach supersonic speeds. Behind a bow shock, the high temperatures lead to dissociation. In the case of a pure CO_2 freestream, the dissociation will lead to significant CO emission and small concentrations of O and C. With the introduction of N_2 (3% by volume in the Martian atmosphere), CN emission will be observed. The high temperatures lead to a broad distribution of energy throughout the different modes via molecular colli-

sions as the atoms and molecules become significantly thermally excited. As discussed in Section 1.2, if thermal equilibrium is not achieved then the flow will be in non-equilibrium and must be modeled accordingly. Therefore, on top of the Navier-Stokes equations (conservation of mass, momentum and energy), additional equations must be included to solve for each individual species. Finite chemical reaction rates must be used. The models assume two sets of "equilibrium" - translational/rotational equilibrium and vibrational/electronic equilibrium, yielding the so-called "two-temperature" model.

For sufficiently high freestream velocities, shock layer emission from excited species will increase the heat transfer to the surface above conventional convective heating values via radiative heating. Heat transfer can also be augmented via surface catalysis, whereby dissociated species recombine to form CO_2. A *non-catalytic* surface results in the lowest heating rates as no recombination occurs. The *super-catalytic* case is the exact opposite in the sense that full recombination at the surface is assumed irregardless of the local equilibrium conditions. It represents the upper bound on the heat transfer prediction as the gas is returned to its lowest chemical state and hence the maximum amount of heat is released. In between the non-catalytic and super-catalytic solutions is finite-rate catalysis where the incident gas-phase species recombine directly with a previously adsorbed atom or molecule [7].

The collection of high quality, repeatable high enthalpy CO_2 data is very important for the validation of these numerical models. As computing power increases and physical modeling improves, significant cost-saving can be achieved if computation is able to correct replicate the flow physics. However, current CO_2 physical models do carry moderate to significant areas of uncertainty. The two-temperature model described above was developed for air flows and has been applied to CO_2 with minimal validation [120]. There is considerable uncertainty in the current chemical kinetics of a shock heated CO_2-N_2 mixture as many of the reactions have not been validated at conditions typical of Martian re-entry. Catalytic properties of dissociated CO_2 materials are not as well characterized as those in air. Despite expected MSL turbulence transition, the simple engineering correlation using Re_θ and M_e is

usually employed and a more accurate assessment may be required. Additionally, no validated non-equilibrium CO_2 radiative heating model exists.

Current deficiencies in our knowledge of non-equilibrium CO_2 have practical design consequences. The MSL currently carries a 50% uncertainty on its predicted turbulent heating levels [121], which results in a considerable TPS (Thermal Protection System) weight penalty. Depending on which catalysis model is used (for which the catalysis effects are not particulary well characterized or modeled), the predicted centerline heating spans heat flux values ranging from 37 to 125 W/cm^2 [7].

5.2 Review of High-Enthalpy Carbon Dioxide Work

Several researchers have also studied high-enthalpy CO_2 flow over blunt bodies. Stewart and Chen measured bow shock stand-off distances over a 140 degree blunt angle cone (an early version of the MSL model) for a 14.3 MJ/kg pure CO_2 run condition in the NASA Ames 42-inch shock tunnel [8]. Of the three different gas mixtures investigated for the same blunt body, the maximum discrepancy between computation and experiment in the shock stand-off distance was observed for the pure CO_2 condition.

In the T5 facility, Wen and Hornung compared non-equilibrium theoretical sphere shock stand-off distance predictions with extensive experimental and numerical results and found acceptable agreement [118]. In the reflected shock tunnel HEG, CO_2 flow over a 70-degree blunt cone was studied using simulations and experiments by Netterfield et al. [122].

Hollis and Perkins compared various sphere-cone model forebody and aftbody heat transfer values with computational simulations in the HYPULSE expansion tube [5, 6] and the 31-inch Mach 10 Langley wind tunnel [5]. Overall, very good agreement between CFD and experiment was achieved.

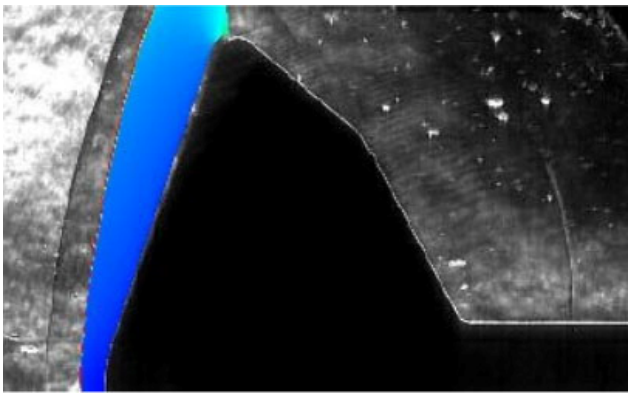

Figure 5.1: Comparison between experimental and numerical shock shape on a 24 inch diameter MSL model in the LENS I facility for a nominal 5.63 MJ/kg run condition. Image re-produced with permission from Matt MacLean of CUBRC.

5.2.1 CUBRC Results

The hypersonic facilities at Calspan-University of Buffalo Research Center (CUBRC) have been central to the investigation of planetary entry flight conditions for many programs, including the up-coming MSL mission. Recent studies revealed that the experimentally observed shock shape and stand-off distance differed significantly from numerical simulations over a 24" diameter MSL model for high-enthalpy test conditions at 5 and 10 MJ/kg in the LENS I reflected shock tunnel facility [1]. The computed shock stand-off distance for the 5 MJ/kg test condition was a factor of 2.25 times smaller than the experimental value as shown in Figure 5.1, for which this discrepancy is clearly visible. However, at a 2 MJ/kg test condition in the same facility, no such differences were observed. To examine this discrepancy further, the same model was tested in the LENS X expansion tube facility at 5 MJ/kg [1]. Excellent agreement was obtained between simulations and experiments in the LENS X facility.

It was proposed that a possible cause for the observed reflected shock tunnel discrepancy was due to uncertainty in the thermochemical state of the freestream after the chemically dissociated test gas is strongly expanded in the nozzle. A follow-up numerical study found that shock shape and stand-off distance matched experimental observation when 42% of the total energy was artificially frozen in vibration [12]. As discussed by the authors, such a

result is clearly aphysical and especially so when one considers that the original calculation had 3.6% of the total energy frozen in vibration. Additionally, frozen vibrational energy was seen to have a greater impact upon the shock stand-off distance than frozen chemical energy. As mentioned above, for a very similar run condition, such a discrepancy was not observed in an expansion tunnel facility. This suggests that complex CO_2 system vibrational relaxation processes, such as those occuring in the reflected shock tunnel nozzle, may not be completely understood.

The previously discussed CUBRC experiments formed a component of a very comprehensive investigation of high-enthalpy CO_2 sphere-cone blunt body flow fields, incorporating several facilities and extensive numerical modeling. In the Caltech T5 facility, a series of shots for a 70^o blunt cone were conducted, and surface heat flux measurements obtained. At angle of attack, it was observed that super-catalytic simulations agreed best with laminar windside data whereas the turbulent leeside was most accurately predicted by the non-catalytic cases [7]. Similar results were also observed for LENS experiments when the model was initially coated in SiO_2 to promote a non-catalytic response [120]. In LENS I, at zero angle of attack, for all locations away from the nose, measurements were best matched with the aphysical super-catalytic boundary condition [4]. The authors commented that the uncertainty in the freestream (due to dissociation) is expected to explain some, but not all, of the discrepancies between heat transfer prediction and measurement. Laboratory experiments which investigated surface reactions involving dissociated CO_2 found no evidence for the depletion of CO by surface reaction at either room temperature or 250^oC [123]. Such a result is inconsistent with the robust CO oxidation reactions required to enforce the super-catalytic boundary condition. This provides further motivation to collect additional data and compare heat transfer measurements with simulations incorporating catalytic boundary conditions.

5.3 Scope of Current Work

At the cost of reduced test time and potential loss in core flow, expansion tubes are capable of producing high-enthalpy conditions while the degree of freestream dissociation is significantly reduced in comparison to reflected shock tunnels. In a reflected shock tunnel, chemical and vibrational freezing can occur downstream from the nozzle throat, which as discussed above can alter the test conditions in a complex manner. In the present work, the HET is used to provide additional high-enthalpy CO_2 data and compare with numerical results.

The issues discussed above in Sections 5.1 and 5.2.1 provide impetus for the current study. Due to the operating constraints of the HET, sufficiently high velocities cannot be achieved to access radiative heating conditions. The small scale of the facility and low Reynolds numbers will make any MSL capsule transitional studies difficult. However, catalysis effects can be investigated as sufficient CO mole fractions can be achieved to account for any CO oxidation reactions. The fact that the HET can provide high-enthalpy CO_2 flow demonstrates the potential for the facility to be used to provide the kind of fundamental data that is required by the CFD community to accurately predict non-equilibrium CO_2 flow.

In this study, we first obtain a suitable test condition with first-order matching of the high-enthalpy CUBRC test case. Next, spherical models of different diameters (7.9 to 63.5 mm) are examined as a canonical flow field and measured shock stand-off distances compared with theoretical prediction. Sphere shock layer shapes are compared with axisymmetric simulations using the US3D code [124]. These comparisons are useful for additional verification of facility operation, as well as for validation of future computational simulations and thermochemical models. For the same test condition, shock shapes over a MSL model geometry at three flight angles of attack (0, 11 and 16 degrees) are obtained and also compared with simulations. At each angle of attack, surface heat flux measurements were made using co-axial thermocouples. The heat transfer distributions are compared with calculations assuming non-catalytic and super-catalytic boundary conditions.

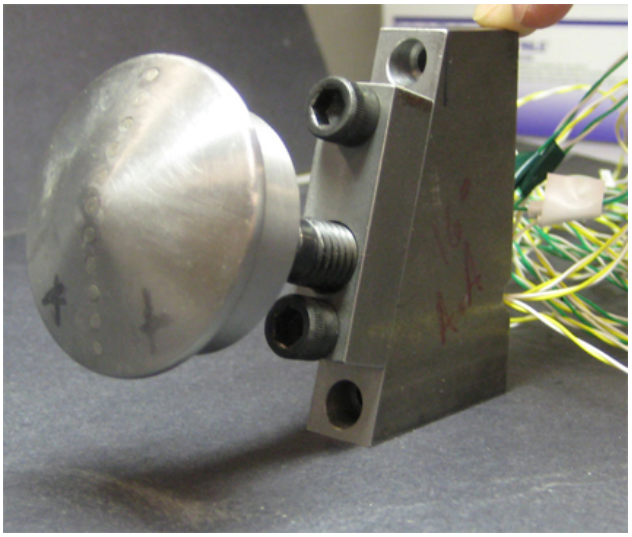

Figure 5.2: MSL model, machined from A2 tool steel with a major diameter of 2 inches. MSL scaled down for HET application by Andy Swantek.

5.4 Experimental Setup

Shock shapes are visualized using a schlieren system consisting of a Xenon nanopulser (10 ns duration) white light source and pco.1660 (Cooke Coorporation) CCD camera. The system is triggered via the transmitted shock arrival at a 1MHz response pitot pressure transducer (PCB 113A26) sting-mounted in the test section 63.5 mm below the model centerline.

The spheres and MSL are mounted within the test section such that their axial centerlines approximately correspond with the tube centerline. The 11 and 16 degree angle of attack positions were achieved by mounting the MSL model on triangular spacer blocks, whose hypotenuse was angled at the desired angle of attack from the vertical. The spheres and MSL were made from Al 2024 and A2 tool steel respectively. With a major diameter of 50.8 mm, the MSL model used in this study is approximately 1/100th the size of the actual vehicle. The scaled down dimensions of the MSL were designed according to those specified in Hollis et al. [2]. As with the actual vehicle, the model has a 70 degree sphere cone forebody, however the current model only has single conic (40 degree) aftbody whilst the actual vehicle is biconic. The MSL model, instrumented with thermocouples, is shown in Figure 5.2.

The thermocouples used in these experiments are based on the design of Sanderson [125].

They are coaxial, 2.4 mm in diameter, type E (Constantan-Chromel), and mount flush with the surface of a model. The two coaxial elements are designed such that an extremely thin junction (on the order of 1 μm) is formed at the surface. This type of thermocouple gauge is used extensively in the T5 reflected shock tunnel [125, 126, 127], where the high enthalpy test conditions result in adequate signal levels and the robust design of the gauges make them highly resistant to damage caused by particulates in the test gas as well as the large heat fluxes [125]. The output signal is processed by a differential amplifier circuit mounted exterior to the test section. This also serves to eliminate the effects of any extraneous electromotive forces generated by the thermocouple. The circuit gain is 1000 to maximize signal amplitude. Individual calibration of thermocouples is not necessary, since the temperature response of all common thermocouple types is well known. The NIST thermocouple reference tables were used to convert from voltage to temperature [128]. For more information regarding the development, testing and performance verification of the thermocouples, see Flaherty and Austin [129].

5.5 Numerical Modeling

The simulations were conducted using the code US3D developed at the University of Minnesota [124]. US3D is a hybrid, implicit unstructured finite volume code that solves the compressible Navier-Stokes equations. The inviscid fluxes are calculated using a low dissipation version of Steger-Warming flux vextor splitting. Second order accuracy in space is achieved using an upwind biased MUSCL approach. Implicit time integration is performed using a parallel line relaxation procedure. The grid was adapted to align with the bow shock wave to improve the accuracy of the solutions.

The state-specific vibrational model of Doraiswamy et al. for the CO_2-CO-O_2-O system is employed[14] for thermochemical modeling. In this model, the symmetric stretch and bending modes of CO_2 are grouped together due to the Fermi resonance between the modes,

and these modes are assumed to be in equilibrium with the translational modes. The antisymmetric mode is considered separately and relaxes toward equilibrium with finite-rate vibration-translation and vibration-vibration processes. The first few vibrational states are considered for each species up to a limit of $8000\,\mathrm{cm}^{-1}$ above the ground state. Each vibrational level is treated as a separate species, with a total of 15 state-specific levels considered (4 levels for CO_2, 5 for CO, 6 for O_2). The vibrational relaxation model has been shown to reproduce experimental measurements, and a complete description is given in Doraiswamy et al [14].

The three chemical reactions that describe the CO_2-CO-O_2-O system are taken to be

$$CO_2 + M \leftrightharpoons CO + O + M \tag{5.1}$$

$$O_2 + M \leftrightharpoons O + O + M \tag{5.2}$$

$$CO_2 + O \leftrightharpoons CO + O_2 \tag{5.3}$$

Standard rate constants for these reactions are used [14].

5.6 Results and Discussion

5.6.1 Criteria for Selection of Experimental Test Conditions

A carbon dioxide test gas condition was selected to match the relevant experimental parameters in CUBRC facilities as closely as possible [130, 131]. Since in general all test parameters cannot be matched from facility to facility, identification of the dominant flow properties for a particular measurement is important in comparative ground testing as well as in flight simulation. One aspect of the present study is to evaluate what parameters should be matched for adequate comparative measurements of shock shape and heat transfer in different expansion tube facilities. Simulations of blunt bodies in nitrogen flows by Macrossan showed that

free stream dissociation had little effect on the bow shock at different angles of attack [132], indicating that in nitrogen, the degree of dissociation in shock tunnel versus flight tests was less important to match than the Mach number.

As an expansion tube can cover a range of operating conditions, a parametric study based on steady, one-dimensional gas dynamic calculations is completed to select candidate test conditions. The following criteria were identified as important during the run condition selection process:

- Matching the enthalpy of the LENS I run condition
- Core flow size
- Minimizing test gas noise
- Large shock stand-off distances
- Practical HET operational considerations

5.6.1.1 CUBRC Run Condition Matching

The discrepancy between the CUBRC LENS X and LENS I results was observed for test conditions with 5.63 MJ/kg stagnation enthalpy in CO_2 [12]. For the same stagnation enthalpy, we select the test gas velocity as the first-order matching parameter due to the large kinetic energy contribution to the total enthalpy. Higher order matching could be achieved by using the frozen Mach number as a selection parameter, however the LENS X run condition frozen Mach number is 11.81, which is outside the operating regime of the HET.

In an expansion tube, for a fixed test gas composition and burst pressure (constant p_4), test gas properties can be changed by either altering the driven fill pressure, p_1, or the acceleration section conditions (γ_5, p_5). Table 5.1 presents properties for four different run conditions. In each case, the test gas velocity is within ± 43 m/s of the CUBRC test gas

Interface	p_1 (kPa)	p_5 (mTorr)	u_7 (m/s)	$h_{stag,7}$ (MJ/kg)	M_7	T_7 (K)	ρ_7 (kg/m^3)	u_t (m/s)	Test Time (μs)
CO_2-CO_2 (RC2)	1.2	150	2998	5.51	5.52	1212	0.016	3454	293
CO_2-Air (RC5)	1.2	180	3059	5.66	5.72	1172	0.014	3698	274
CO_2-Hel (RC8)	1.2	1050	3066	5.68	5.75	1168	0.014	4328	272
CO_2-Arg (RC11)	1.2	135	3014	5.55	5.57	1201	0.016	4045	288

Table 5.1: Properties for candidate HET run conditions. Initial fill conditions differ by the choice of acceleration gas.

velocity. Transmitted shock velocity is typically accurate to within ±43 m/s in the HET and it is expected that similar error bars will exist for test gas velocity measurements [133]. In the first column, the run conditions were generated by varying the acceleration section gas; here argon, helium, air and carbon dioxide are used. The run conditions are described in terms of the driven-accelerator gas combination. The driven section pressure, p_1, is kept constant in each case and p_5 chosen so as to match the test gas velocity requirement. In each case the driver gas is helium and p_4 kept constant at roughly 2.5 MPa.

5.6.1.2 Core Flow Prediction

Knowledge of the core flow size prior to experimentation is very important for an a priori estimate of expected model dimensions. For the current study, as large a capsule frontal diameter as possible is desired as it permits the maximum number of thermocouple port locations. Boundary layer thickness at the tube exit is predicted via the theory of Mirels as outlined in Chapter 3. This is the boundary layer that forms between the transmitted shock and the secondary contact surface and limits the core flow diameter. Figure 5.3 plots the boundary layer growth along the acceleration section from the secondary diaphragm station to the tube exit (3.96 m), for both laminar and turbulent cases. Table 5.2 is the comparison of the different predicted core flow diameters, depending on laminar or turbulent boundary layers, for the four different conditions. Values in brackets indicate the reduction in core flow diameter assuming a 6 inch. core flow at time of secondary diaphragm rupture (x=0 m). RC2 and RC5 have both the lowest core flow loss and lowest difference between turbulent

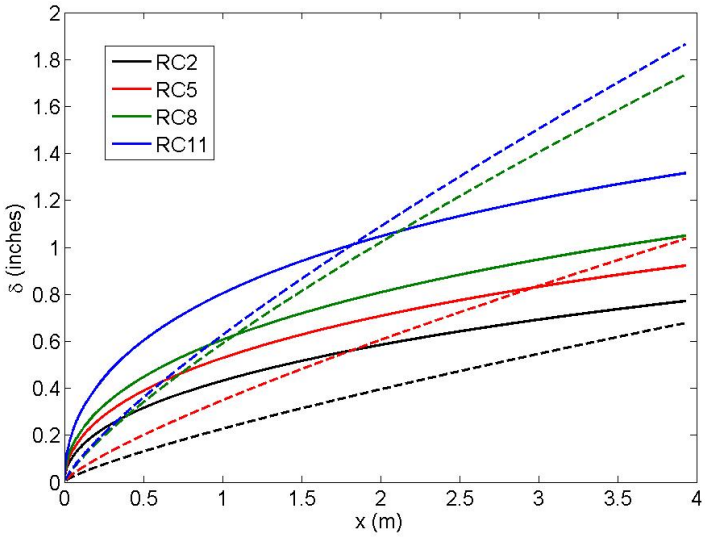

Figure 5.3: Comparison of boundary layer growth for the four candidate run conditions. Solid lines denote laminar boundary layers, dashed lines denote turbulent boundary layers.

Run Condition	$\phi_{laminar}$ (in.)	$\phi_{turbulent}$ (in.)
RC2	4.65 (23)	4.46 (26)
RC5	4.16 (31)	3.93 (35)
RC8	3.90 (35)	2.54 (58)
RC11	3.37 (44)	2.27 (62)

Table 5.2: Laminar and turbulent core flow diameter values for the four candidate run conditions. Percentage decrease of the core flow diameter is given in brackets.

and laminar predictions which indicates that even in the worst case scenario (turbulent) boundary layer these two conditions are the best.

5.6.1.3 Test Gas Noise Minimization

Significant test flow disturbances were found to exist in the first expansion tubes [134, 135]. Paull and Stalker presented a theoretical basis for high frequency fluctuations within an expansion tube test gas slug, which they confirmed via experimental measurements [26]. They showed that acoustic lateral waves emanating from the driver-test gas interface (primary contact surface) were "focused" into the test gas and were responsible for the high-frequency fluctuations. These fluctuations were shown to be minimized by decreasing the primary contact surface interface sound speed ratio, $\frac{c_3}{c_2}$. Experiments within the HET have also confirmed that minimizing this ratio improves test gas arrival confidence and reduces the level of pitot pressure perturbation about the mean [25, 35]. An analytical relationship for the primary contact surface sound speed ratio is [25, 33]

$$\frac{c_3}{c_2} = \frac{\left(\frac{p_4}{p_1}\right)^{\frac{1-2\gamma_4}{2\gamma_4}} \left(\frac{c_4}{c_1}\right)}{\sqrt{\frac{\frac{2}{M_s^2}+\gamma_1-1}{\gamma_1+1}\left[1+\frac{2\gamma_1(M_s^2-1)}{\gamma_1+1}\right]^{\frac{1}{2\gamma_4}}}} \tag{5.4}$$

where the subscripts refer to the states shown in Figure 2.1 and M_s is the incident shock Mach number. In Dufrene et al [25], it was established that the maximum acceptable value of $\frac{c_3}{c_2}$ was 0.55, whereby the fluctuations were at most $\pm 50\%$ of the mean value. With a fixed burst pressure (constant p_4) as in the case of HET operation, lower p_1 values correspond to lower $\frac{c_3}{c_2}$ values. In Table 5.1, each run condition was deliberately selected with the same p_1 value so that the frequency focusing effect is the same in each case.

As discussed in Section 3.2.2, test gas noise levels were seen to correlate with the total characteristic acoustic impedance across the secondary diaphragm. It was seen that the RC8 test gas displayed significantly larger fluctuations than the other 3 conditions. Ordered from

high to low levels of noise, the candidate conditions were RC8, RC5, RC2 and RC11.

5.6.1.4 Shock Stand-off Distance Prediction

Estimates of the shock stand-off distance were made for candidate test conditions using the theory of Wen and Hornung [118]. For non-equilibrium flows, Lick applied inverse methods to calculate shock shape in front of a sphere [136] and his work was extended by Hall et al. [137]. Using the ideal dissociating gas model (diatomic gas), Hornung investigated non-equilibrium flow over spheres and cylinders [138]. Extending Hornung's original work to more complex gases, Wen and Hornung carried out a joint theoretical and experimental study of non-equilibrium dissociating flow over spheres and developed a model for the stand-off distance in terms of a modified dimensionless reaction rate parameter [118]. Inger et al. presented a hypersonic shock stand-off theory, incorporating non-equilibrium gas mixtures with freestream dissociation, based upon a compressibility co-ordinate transformation [139]. A theoretical model for the non-equilibrium shock stand-off distance was also introduced by Belouggadia et al [140], following an analytical solution proposed by Olivier [141]. The Olivier solution was confined to frozen and equilibrium flows, while the numerical model of Belouggadia et al. implemented calculated density profiles. At the post-shock to equilibrium density ratios in the present experiments, we find there is very little difference between density profiles calculated by the Wen and Hornung and Belouggadia et al. methods. As a result, the theory of Wen and Hornung is used in this study. Their theory is now briefly reviewed.

In their inviscid analysis, Wen and Hornung assumed a simplified density profile along the shock stagnation-line. From the frozen value, ρ_s, the density rises linearly towards the stagnation point of the sphere until, if at all, the equilibrium value is reached after which the density will stay constant with the density at the body, ρ_b, equal to the equilibrium density, ρ_e. The linear gradient is determined by the dissociation rate directly downstream of the

shock. They defined a non-dimensional shock stand-off distance, $\widetilde{\Delta}$, as:

$$\tilde{\Delta} = \frac{\rho_s}{\rho_\infty}\frac{\Delta}{d} \tag{5.5}$$

where ρ_∞ is the freestream density, Δ is the shock stand-off distance and d is the sphere diameter. The theory admits the calculation of $\widetilde{\Delta}$ in terms of a dimensionless reaction rate parameter, $\widetilde{\Omega}$. $\widetilde{\Omega}$ has the physical significance of being the ratio of the energy absorption by chemistry to the input rate of freestream kinetic energy. Physically, a zero $\tilde{\Omega}$ corresponds to frozen conditions (no dissociation) and an infinite value corresponds to very fast reactions and equilibrium. In between these two limits, two conditions exist: a fully non-equilibrium shock layer, with $\rho_b<\rho_e$, and a shock layer with both non-equilibrium and equilibrium portions, such that $\rho_e=\rho_b$. Wen and Hornung derived the following relationships for a fully non-equilibrium shock layer and a partial non-equilibrium, partial equilibrium shock layer respectively

$$\tilde{\Delta} = \frac{1}{\tilde{\Omega}}\left[-1+\sqrt{1+2L\tilde{\Omega}}\right] \tag{5.6}$$

$$\tilde{\Delta} = \frac{\rho_s}{\rho_e}\left[L+\frac{1}{2\tilde{\Omega}}\left(\frac{\rho_e}{\rho_s}-1\right)^2\right] \tag{5.7}$$

For spheres, L is taken to be equal to 0.41 [118]. We see that in the former case, the stand-off distance is only a function $\widetilde{\Omega}$ while for the latter case it is a function of both $\widetilde{\Omega}$ and $\frac{\rho_e}{\rho_s}$. Wen and Hornung also presented explicit expressions for a transition point ($\widetilde{\Omega}_0$,$\widetilde{\Delta}_0$) at which the density will equal the equilibrium density. These are

$$\tilde{\Omega}_0 = \frac{(\rho_e/\rho_s)^2-1}{2L} \tag{5.8}$$

$$\tilde{\Delta}_0 = \frac{2L}{1+(\rho_e/\rho_s)} \tag{5.9}$$

It is well-known that the shock stand-off distance is most dependent upon the density ratio across the shock wave, $\frac{\rho_s}{\rho_\infty}$ [118, 138]. From shock-jump relations, this ratio can expressed

solely in terms of the specific heat capacity ratio, γ, and the incident Mach number. From Table 5.1, the Mach numbers are very similar and hence the variation in shock stand-off distance will be very small. Therefore, it is expected that no effective experimental benefit in terms of the shock stand-off distance is achieved by selecting one condition over another. For a 2 inch sphere with a frozen shock layer ($\tilde{\Omega}$=0), the shock stand-off distance across the four candidate run conditions varies by only 0.3 mm, which offers no experimental advantage.

5.6.1.5 Practical Considerations

The primary practicality concern for run condition selection is to reduce the shot time, of which the acceleration section evacuation process occupies a major portion. The pump-down time is reduced if the acceleration gas is air as it eliminates the need to pump-down the accelerator to below 200mTorr before filling with the desired gas and then evacuating down to the final p_5. For high Mach number non-air accelerator gas run conditions, where p_5 is typically below 300 mTorr, this adds at least 25 minutes to the shot time.

5.6.2 RC5 Run Condition

Based on the discussions of Sections 5.6.1.1-5.6.1.5, the RC5 run condition was selected. The choice was primarily dictated by practical considerations such as the pump-down time, test gas noise levels and the size of the core flow. While RC2 offered larger core flow sizes and lower test gas levels than RC5, these differences were not considered large enough to offset the cost of longer run times associated with the CO_2 acceleration gas. Comparison between perfect-gas prediction and experimental measurement is shown in Table 5.3. All the experimental values are averaged values across a number of realizations. The pitot pressure measurements were obtained 6.35 mm below the tube centerline. Static pressure values were obtained at two stations, 30.48 cm and 55.88 cm, upstream from the tube exit.

There is a discrepancy between the experimental and theoretical pitot pressure value. The theoretical test gas pitot pressure is determined from the Rayleigh pitot equation. The

	M_7	$h_{o,7}$ (MJ/kg)	Test Time (μs)	$P_{7,pitot}$ (kPa)	P_7 (kPa)	u_t (m/s)	u_7 (m/s)	u_s (m/s)	ϕ (mm)
Exp.	–	–	150	82.0±4.0	2.7±0.3	3644±41	–	1832±38	114.3
Theo.	5.7	5.67	274	128.3	3.2	3710	3059	1853	105.4

Table 5.3: Selected test condition (RC5) parameters. Theoretical calculations assuming one-dimensional, perfect gas dynamics. Comparison with experimental measurements.

equilibrium pitot pressure, using CEA, is calculated to be 119 kPa - clearly not a sufficient reduction to match the experimental value. Despite the pitot pressure discrepancy, it is felt that the run condition is accurately achieved based upon the close agreement with simulation as discussed in the next section.

The transmitted shock speed was also measured in the test section using the shock time-of-arrival at staggered pitot probes. This approach has been used in the past to characterize a test condition and in that instance, it was found that the measurement agreed with computational results [90]. Experimental pitot surveys of the core flow at this test condition were carried out to determine that the maximum model diameter that can be chosen is about 65 mm.

The $\tilde{\Delta}$-$\tilde{\Omega}$ curve for RC5 was generated, Figure 5.4. Here the y-axis is slightly re-cast as another non-dimensional shock stand-off distance, $\frac{\Delta}{d}$. The equilibrium density was calculated with the specified inflow conditions identified in Table 4.1 and using CEA [117]. The transition co-ordinate was calculated to be (3.72,0.0417). Wen and Hornung theoretically predicted and experimentally demonstrated that as the sphere diameter is increased, the stagnation line shock layer will transition from completely non-equilibrium conditions (to the left of the dashed vertical line in Figure 5.4) to a profile with an increasingly equilibrium portion. The next section explores different spherical diameter shock layers and their comparison with axisymmetric CFD simulations.

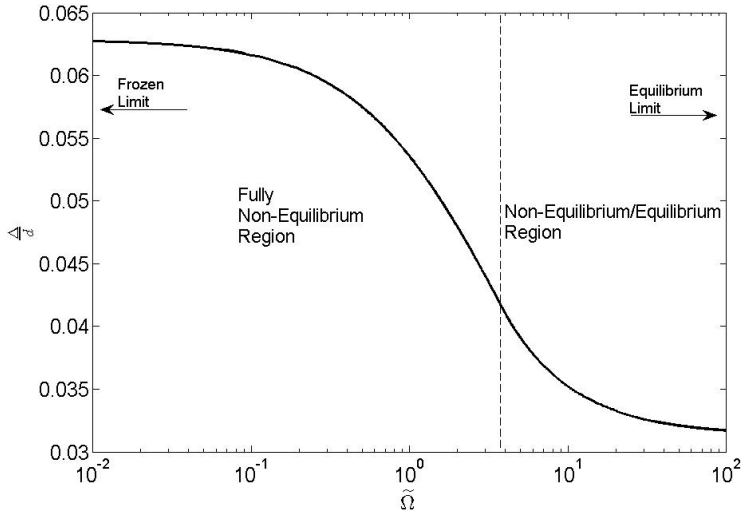

Figure 5.4: Non-dimensional shock stand-off distance as a function of the dimensionless reaction rate parameter, $\tilde{\Omega}$, for the RC5 run condition. The point where ρ_b=ρ_e, separating a fully non-equilibrium shock layer from a partial equilibrium/partial non-equilibrium region, is indicated by the dashed vertical line.

5.6.3 Sphere shock shapes

We initially examine spherical models in benchmark tests for which results can be compared with theoretical predictions and numerical simulations. This flowfield provides additional verification of facility operation via numerical simulations and thermochemical calculations with a relatively simple geometry. Shock stand-off distances over a sphere have been previously investigated in non-equilibrium air and nitrogen flows [138, 142]. As discussed in Section 5.2, Wen and Hornung measured shock stand-off distances over spheres in a high-enthalpy carbon dioxide flow field [118]. Outstanding issues in a carbon dioxide flowfield still remain, including the role of thermochemical energy storage and transfer and the possibility of facility-specific data. Therefore, the measurement of shock stand-off distances for similar enthalpy conditions in another hypervelocity facility provide data to complement existing results.

Selected schlieren images for spheres of diameters from 25.4 to 63.5 mm are shown in Figure 5.5 a)-d) and compared with numerical simulations. Numerical simulations were carried out at the free stream conditions predicted by ideal gas theory, Table 5.3. The measured

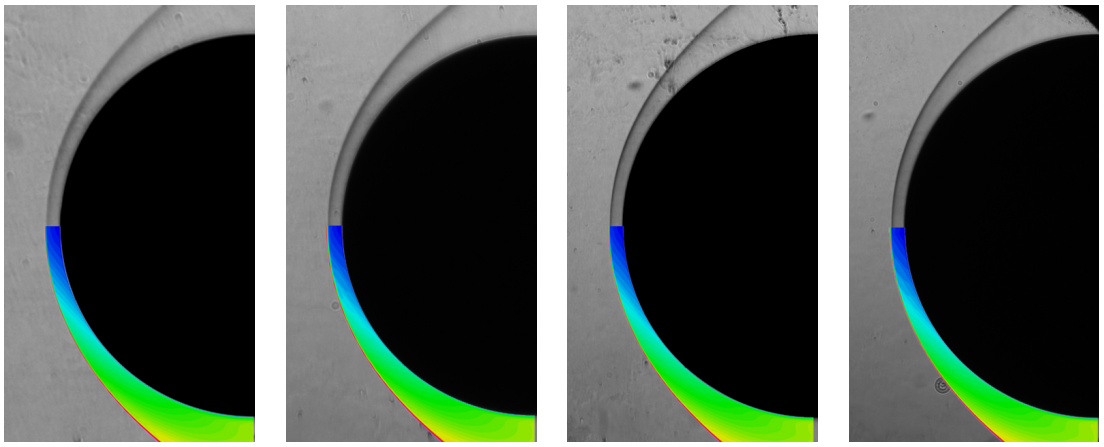

a) b) c) d)

Figure 5.5: Comparisons of experimental schlieren images and simulations of bow shock shapes over spheres of diameter a) 25.4 mm, b) 37.5 mm, c) 50.8 mm, and d) 63.5 mm.

and predicted shock stand-off distances for each sphere diameter are in very good agreement and within at maximum 10% of each other, Table 5.4. The experimental uncertainty on the stand-off distance measurement is estimated to be 1 pixel, or approximately 0.05 mm.

Normalized vibrational temperature contours are shown in Fig 5.6 a)-d). For all the spherical geometries, the simulated temperature contours predict that the majority of the stagnation line shock layer is in thermal equilibrium and only a small non-equilibrium region exists near the bow shock.

Stagnation line density profiles for the four spheres were calculated, Figure 5.7, and plotted against $\frac{y}{\Delta}$, where y is the distance from the shock. The equilibrium limit, calculated from a CEA calculation, is also included. Wen and Hornung presented inviscid computations, while these computations are fully viscous and capable of resolving the boundary layer as evidenced by the steep rise in density close to the body. Profiles of $\frac{T_v}{T}$, the ratio of vibration-to-translation temperatures, are also presented in Figure 5.8. Here we see that for all sizes, the major portion of the shock layer is in thermodynamic equilibrium. For all spheres, equilibrium is reached shortly downstream of the shock by $\frac{y}{\Delta}$=0.09. We see that increasing the sphere diameter increases the equilibrium extent within the shock layer. Fig-

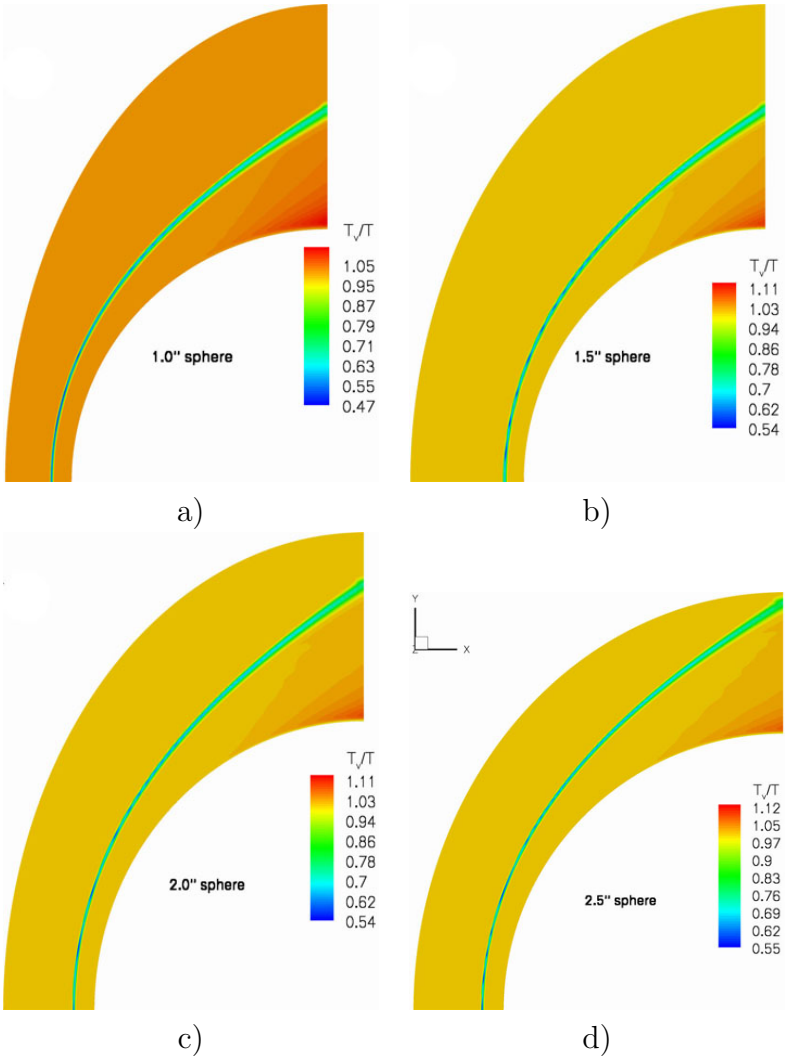

Figure 5.6: Vibrational temperature contours from US3D simulations for sphere diameters of a) 25.4 mm, b) 37.5 mm, c) 50.8 mm, and d) 63.5 mm.

ure 5.9 is the shock layer temperature profile for the 1.5 inch sphere. Mass fraction profiles for CO, O and O_2 and also for CO_2 are shown in Figures 5.10 and 5.11 respectively for the 1.5 inch sphere. From these figures we can see that thermodynamic equilibrium exists (Figure 5.8), but not chemical equilibrium as the species concentrations are changing. The chemical non-equilibrium is what accounts for the rising density profile above the equilibrium value as dissociation is a contributing factor to the change in density. This is also reflected in the dimensional temperature profile, Figure 5.9, where the temperature decreases sharply within the non-equilibrium region and continues to decay throughout the shock layer. This occurs as the dissociation of CO_2 increases the chemical energy of the system, which comes at the expense of thermal energy and the subsequent decrease in temperature takes place. From Figure 5.10, the minor species concentrations increase throughout the shock layer as CO_2 dissociates. The depletion of CO and O and the increase in CO_2 close to the body is indicative of CO_2 recombination within the boundary layer. Recombination within the boundary layer suggests an equilibrium boundary layer [143] and will increase the thermal energy of the flow as chemical energy is released. However, the driving force for the temperature profile within the boundary layer will be the boundary condition of a cold wall.

Figure 5.12 is the $\tilde{\Delta}$-$\tilde{\Omega}$ curve for RC5 (re-produced here from Figure 5.4) compared against the experimental result. The predicted values of Δ for the four spheres from the theory of Wen and Hornung, based upon the calculated $\tilde{\Omega}$ values, are presented in Table 5.4. It is clear from both the table and figure that the theoretical prediction does not represent the experimental result. In the table, percentage difference between theory and experiment is included in parentheses. The differences are quite large, but more concerning is that the values do not even match the characteristic shape of the $\tilde{\Delta}$-$\tilde{\Omega}$ curve. For their theory to be applicable, Wen and Hornung require that the binary scaling, ρd, be sufficiently large (where d is the sphere diameter). Wen establishes a "rule of thumb" for binary scaling, however this is valid only for a diatomic gas [144]. In their work, the sphere diameters ranged from 2 to 6 inches and the freestream densities were considerably higher, resulting in ρd values that are

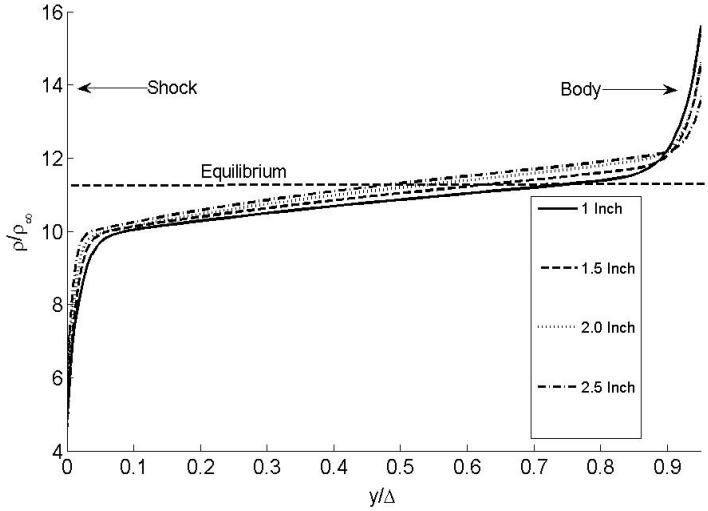

Figure 5.7: Stagnation line density profile from US3D numerical computations for the 4 different sphere diameters considered in this study: 1, 1.5, 2 and 2.5 inches. Profiles are calculated for freestream conditions predicted by inviscid, perfect-gas HET operation.

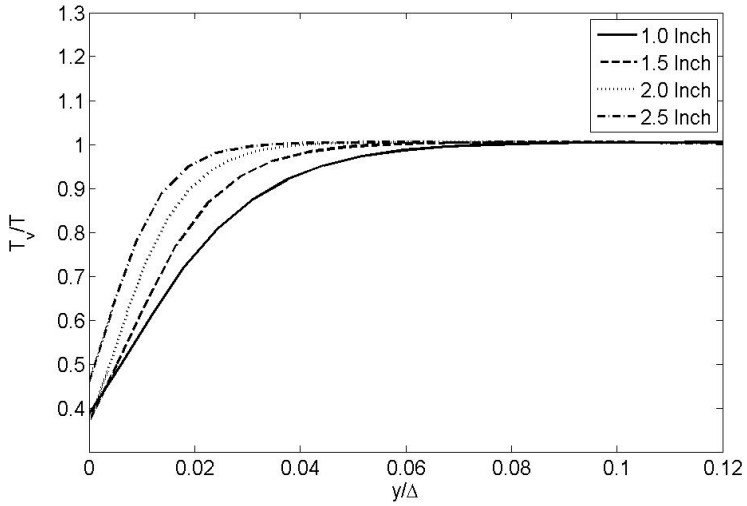

Figure 5.8: Stagnation line temperature profiles from US3D numerical computations for the 4 different sphere diameters considered in this study: 1,1.5,2 and 2.5 inches. Normalized temperature is presented as the ratio of vibrational temperature to translational temperature. Note that only a small section of the shock layer is plotted as thermal equilibrium is reached very quickly.

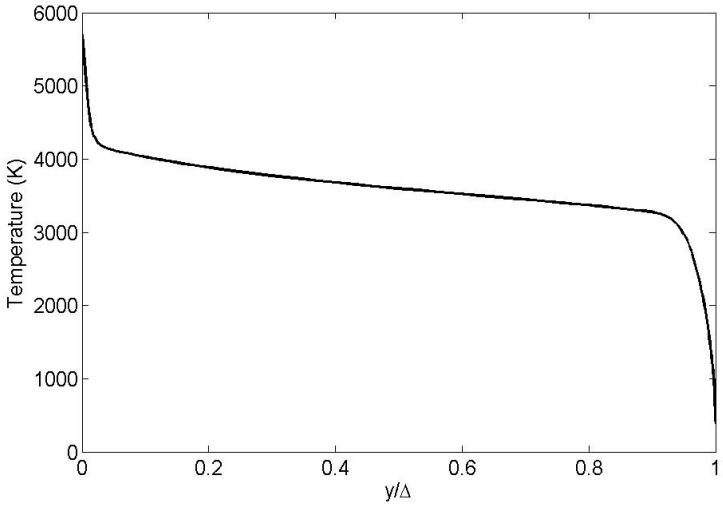

Figure 5.9: Stagnation line temperature profile from US3D numerical computation for the 1.5 inch sphere.

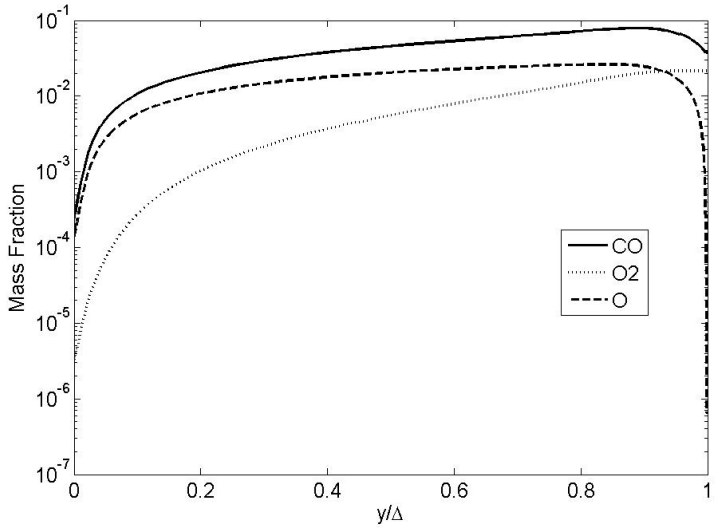

Figure 5.10: Mass fraction profiles for CO, O and O_2 from US3D numerical computations for the 1.5 inch sphere.

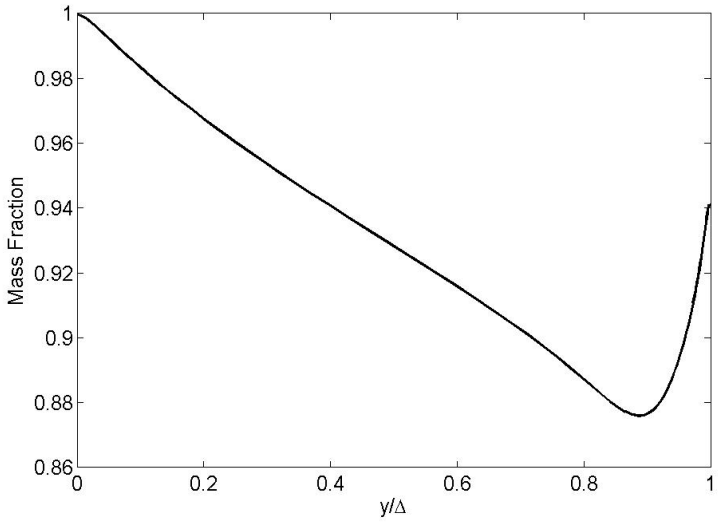

Figure 5.11: CO_2 mass fraction profile from US3D numerical computation for the 1.5 inch sphere.

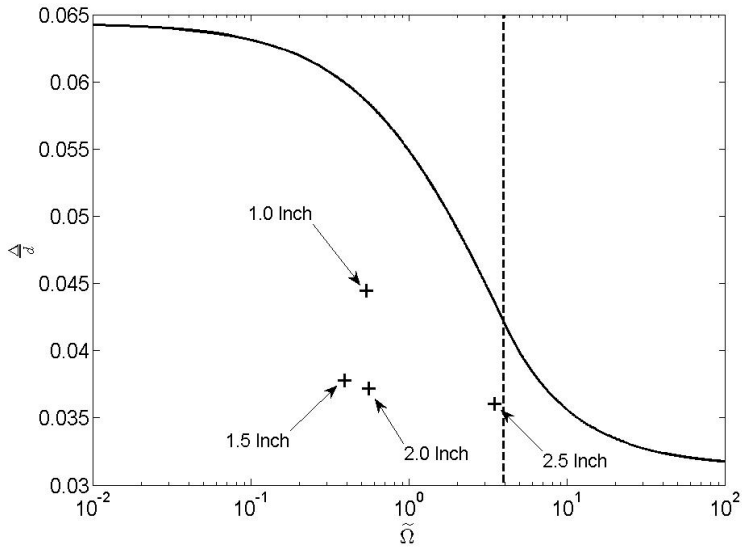

Figure 5.12: Comparison of normalized experimental stand-off distance (black crosses) with theoretical prediction (solid black line). The predicted transition from non-equilibrium to equilibrium is shown as the dashed line.

Sphere diameter (mm)	Δ_{exp} (mm)	Δ_{num} (mm) US3D	Δ_{theory} (mm) Wen and Hornung [118]	Δ_{theory} (mm) Inger et al. [139]
63.5	2.29	2.45 (7.0)	2.76 (20.5)	2.77 (21.0)
50.8	1.89	1.98 (4.8)	2.97 (57.1)	2.43 (28.6)
38.1	1.44	1.53 (6.3)	2.28 (58.3)	1.65 (14.6)
25.4	1.13	1.06 (-6.2)	1.49 (31.9)	1.16 (2.7)

Table 5.4: Comparison between the experimental shock stand-off distance, the numerical result from US3D and the two theoretical solutions.

an order of magnitude larger than the RC5 value. For example, for a comparable stagnation enthalpy and Mach number run condition, the maximum T5 ρd value is 6.87×10^{-3} while the maximum HET value is 9.14×10^{-4}. The results from the T5 facility saw good to very good agreement between the binary-scaling based theory and experimental measurement for stagnation enthalpies ranging from 4.11 to 10.76 MJ/Kg in CO_2 [118, 144]. It therefore appears that the binary scaling values of this study are too small for the experimental conditions to be applicable to Wen and Hornung's theory.

As the theory of Wen and Hornung did not appear to be valid for the current study, shock stand-off distances based upon the theory of Inger et al. [139] were also calculated. The theory implements a compressibility coordinate transformation. It is an inviscid approximation. Within their paper, Inger et al. obtained good agreement with the experimental data of Wen and Hornung [118]. The calculated results are also shown in Table 5.4. Percentage difference between experiment and theory are shown in parentheses. Unlike the theory of Wen and Hornung, the coordinate transformation approach has captured the trend observed in the experimental data of an increasing shock stand-off distance with increasing sphere diameter. The theory over-predicts both the experimental measurement and numerical result, with an experimental over-prediction of up to 27%. Based upon these results, it appears that the compressibility coordinate transformation approach is capable of providing a reasonable approximation of shock stand-off distances in non-equilibrium gas flows for low-density, small-scale conditions that otherwise appear not to be applicable for the theory of Wen and Hornung. For details on the application of these two theories please see Appendix A.4.

5.6.4 Shock Shapes at Angle of Attack

Experimental images and numerical simulations of the bow shock shape over the MSL geometry at three angles of attack are shown in Figure 5.13. Images show increasing shock stand-off distance with increasing angle of attack. In the non-zero angle of attack images, in particular for the 16 degree case, the shock appears to be spherically shaped on the windward side and more conically shaped over the leeward side. Similar results were also observed by Stewart and Chen [8]. For the 16 degree case, Figure 5.13 c), the maximum bow shock gradient with respect to the horizontal (freestream) has shifted towards the windward side. As measured from experiment, the vertical shift of this location is 8.5 mm. To quantify the comparison between the predictions and experiments, an edge detection algorithm was used to extract the shock shape. For the 11 degree case, the average horizontal displacement at each given vertical location between numerical and experimental result is calculated to be 1.64 pixels. With a minimum resolution of 1 pixel, restricting the accuracy to approximately 0.06 mm, this agreement is excellent, as seen in Figure 5.14 which shows the comparison between the two bow shock fronts. A similar degree of agreement was also seen for the 16 degree case.

We compare the measured shock shape at zero angle of attack with the experimental and computational results from previous studies, Figure 5.15. The stand-off distance is a strong function of the density ratio across the shock. Despite the difference between the LENS X and HET frozen Mach numbers, the density ratios differ by about 15% and as such, to first-order it is appropriate to scale the images by the model diameter. Therefore, to first-order we see very good agreement between our result and that observed in the LENS X expansion tunnel [1]. Calculated shapes at the conditions of the LENS X experiments are also in good agreement with the present measurements.

As previously discussed, images revealed that the experimental shock stand-off distance in the LENS I facility was approximately 2.25 times larger than predicted by simulation. The large anomalous shock stand-off distances have raised the question as to whether shock

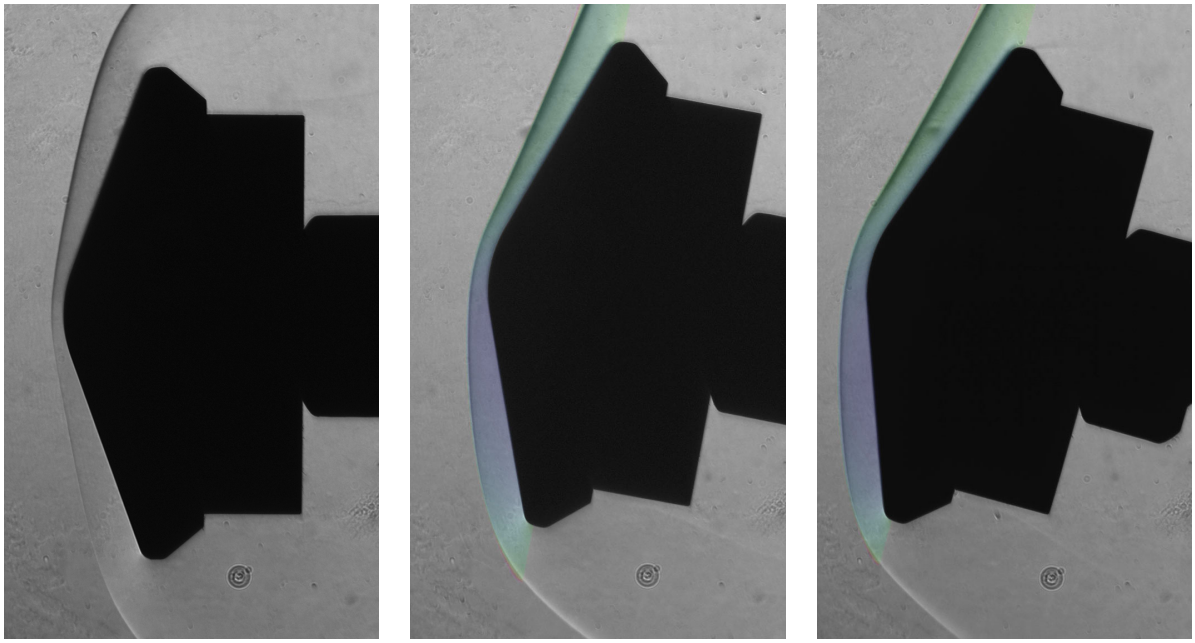

a) b) c)

Figure 5.13: Schlieren images, of bow shock shapes over the MSL geometry at angles of atack of a) 0, b) 11 and c) 16 degrees. For the 11 and 16 degree cases, the simulation results have been overlayed onto the experimental image.

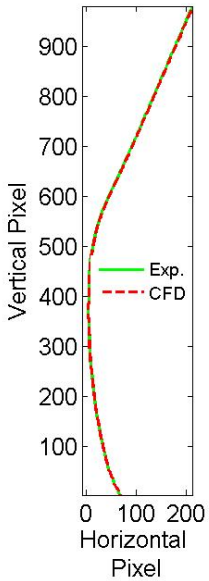

Figure 5.14: Comparison between experimental (solid line) and numerical (dashed line) bow shock front shapes over the MSL for run condition RC5. Angle of attack is 11 degrees. In the figure, 1 pixel is approximately equal to 0.06 mm.

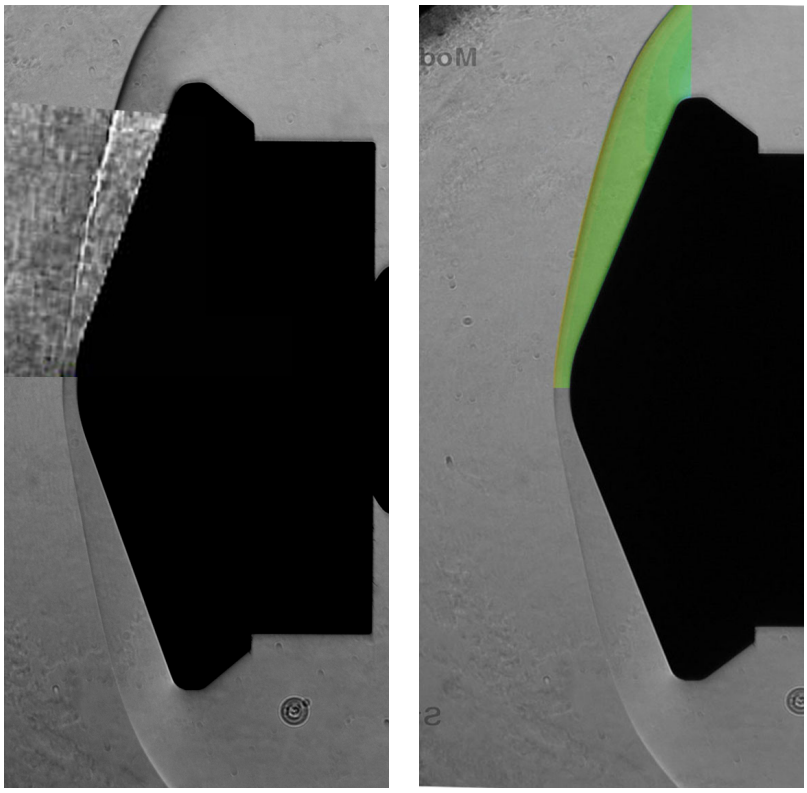

a) b)

Figure 5.15: Comparison of the present data with a) CUBRC LENS X data [1] and b) DPLR simulations for the MSL model at zero angle of attack [1]. Good agreement is observed with simulations, and for both expansion tunnel experiments.

tunnels are valid for evaluating non-equilibrium phenomena in CO_2 [120]. The data collected in this work, for which most of the freestream energy is in kinetic (as opposed to internal) form, aims to contribute to the experimental database towards answering this question.

5.6.5 Laminar Heat Flux and Catalytic Heating

Extensive work has been completed using heat transfer measurements for CO_2 aerothermodynamic studies. For a configuration with a similar corner-nose radius ratio as the MSL, Stewart and Chen reported a 13.76% difference between experiment and simulation [8]. For the Pathfinder geometry (70-degree sphere cone), Hollis and Perkins measured heat transfer on Macor models using palladium thin-film gauges [6]. Computed forebody heating rates agreed well with measurements except those readings near the stagnation point [11]. They

attributed this difference to the computational grid and uncertainties in the physical models. For a variety of run conditions, Hollis et al. found that windside heating augmentation was not correlated with Re despite such a correlation being identified in perfect-gas air flows for the same configurations [2]. Thermocouple data was obtained for a variety of run conditions in the T5 facility [7]. In a LENS I study, thermocouple data was collected on a MSL model at 11-degree angle of attack [3]. Based upon these results, and at the same conditions, further studies were commissioned and heat transfer data collected using thermocouples, thin-film gages and calorimeters [4]. A large volume of aeroheating data also exists that was obtained in different wind tunnel facilities including the NASA Langley 20-inch Mach 6 wind tunnel [2, 9, 145, 146], the NASA Langley 31-inch Mach 10 wind tunnel [5] and T9 at AEDC [147] (Arnold Engineering Development Center). Wind tunnel data was preferred for capsule selection studies due to the repeatability of operating conditions and well defined thermodynamic conditions (perfect gas). However, this entire dataset cannot speak to any thermochemical influences and is mentioned here for completeness.

Extensive investigations into the influence of wall catalysis boundary conditions upon surface heating in high-enthalpy carbon dioxide flow fields have been completed in the LENS facilities [2, 4]. MacLean and Holden compared heat transfer results with different catalytic boundary conditions. Discrepancies between the experimental surface heat transfer results and computation in the reflected shock tunnel facilities for three different high-enthalpy CO_2 run conditions (h_0=5.63, 5.99 and 8.65 MJ/kg) [4] were observed. At the low-enthalpy condition (h_0=1.89 MJ/kg), the overall agreement was very good. MacLean and Holden conclude that freestream uncertainty, and hence vibrational relaxation processes within the nozzle, is a contributing factor to, although not a full explanation of, these differences. Results from the CUBRC studies found that the experimental heating rates fell between non-catalytic and super-catalytic boundary conditions, which suggested that finite-rate catalysis existed at all points on the surface [4]. In the T5 facility, super-catalytic predictions best matched the laminar windside data while the turbulent leeside data best matched a non-catalytic wall [7].

In all of the above cases, heat transfer prediction issues occurred despite very good pressure distribution agreement.

As previously discussed in Section 5.4, heat flux in this study is measured using in-house constructed type E thermocouples based upon designs used at Caltech. Gage uncertainty is ±8% based upon the calculations of Davis [126]. We first measure the stagnation point heat flux measurements on a 25.4 mm diameter stainless steel sphere. From three repeat experiments, the average heat flux across the test time is found to be 6.73±0.55 MW/m^2. The semi-empirical prediction of Sutton and Graves [148], which is an extension of the theory of Fay Riddell [143], and US3D numerical results were used for comparison. The theory of Fay and Riddell assumes an equilibrium boundary layer, which is reasonable given the extent of the equilibrium region in the shock layer predicted in Figure 5.6a). The prediction of Sutton and Graves is 6.85 MW/m^2, which agrees well within the experimental uncertainty of the gages. The upper and lower bounds of the US3D prediction, corresponding to super-catalytic and non-catalytic simulations respectively, were 7.34 MW/m^2 and 6.93 MW/m^2, placing the experimental result closer to a non-catalytic wall.

Since the MSL model was constructed of tool steel, two cylindrical models, one of 316 stainless steel and one of A2 tool steel were next tested. Both cylinders were instrumented with a gauge mounted on the vertical axis of symmetry at a 45 degree angle. Figure 5.16 shows the comparison between two gauges in terms of the detected temperature rise. The temporal offset occurs only due to shot-to-shot variation in triggering. For heat transfer calculation, it is the gradient of the temperature history that is important and, as shown in Figure 5.16, the gradients appear to be very similar. At the 45 degree location, the average heat flux measured in repeat experiments was 2.55 MW/m^2 and 2.53 MW/m^2 on the tool and stainless steel models respectively. It is concluded that the heat flux measurements are not influenced by model material for these two steels.

A sample heat flux measurement obtained at the MSL nose for a 0 degree angle of attack is shown in Figure 5.17. At the beginning of the test time, it was observed that the instan-

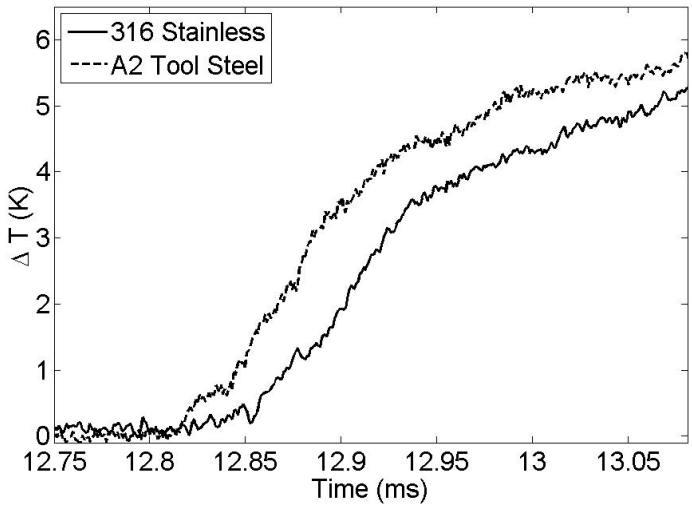

Figure 5.16: Change in temperature time history traces detected by two different thermocouples on A2 and 316 stainless steel cylinder models.

taneous heat flux exhibited transient behavior, displaying primary and secondary peaks as seen in Figure 5.17. The primary large peak is always observed while the secondary smaller peak is not always present. It is postulated that the steep increase in heat flux is a perturbed response of the gage arising from the sharp temperature difference across the secondary interface, separating the relatively hot accelerator gas from the relatively cold test gas. From perfect gas predictions, this temperature difference is estimated to be approximately 5700 K. Pitot pressure traces indicate that the width of the secondary interface is approximately 5 μs, which is on the same order as the width of the primary peak in Figure 5.17. To examine the effect of the transient behavior, the average heat flux is calculated for different sampling windows, Figure 5.17. In each calculation, the end of the test time is fixed (in this case at 13.06 ms) and the sampling window changed by changing the start of the test time, t_{start}. For example, in the figure, as t_{start} increases along the abscissa, the sampling window decreases. As the sampling window includes less and less of the peaks, the instantaneous and average traces converge. Furthermore, as expected based upon the large magnitude of the primary peak, the gradient of the average heat flux is much more pronounced when the primary peak is included in the calculation. Therefore, the incipient heat flux behavior is

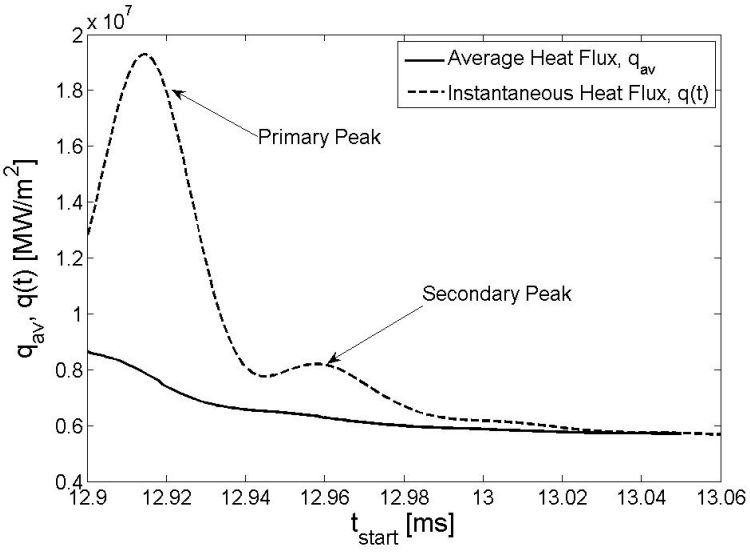

Figure 5.17: Comparison of instantaneous heat flux and the calculated heat flux during the test time.

attributed to gage acclimatization to the large temperature difference across the secondary interface and as such is not included in the average heat flux calculation. The start of the test time is taken to be the time at which the instantaneous heat flux falls within 15% of the average value. For example, in this case the start of the test time for the average heat flux calculation is taken to be 12.97 ms, corresponding to a 90 μs test time.

The MSL model was instrumented with 11 thermocouples along the line of symmetry, with 5 on each side of the nose location. Repeat experiments were conducted for each of the three angle of attack conditions. The heat transfer distributions at the three angle of attacks are shown in Figures 5.18-5.20. Measurements were taken at selected locations, corresponding to the nose tip and $\pm$ 4.3, 8.6 and 17 mm offset from the nose tip. The results from these distributions capture the general trends observed in previous MSL studies in a high-enthalpy shock tunnel. [2]. The nose heat transfer decreases with increasing angle of attack, which is indicative of the stagnation point shifting to the windward side as observed in Figures 5.13 a)-c). At 16 degrees, the average measured heat flux is 5.11 MW/m^2, which is approximately a 14% reduction compared to the 0 degree configuration. On the windward side, the heat fluxes appear to be invariant with angle of attack for the angles considered. Additionally, the

asymmetric nature of the curve has been captured at the 11 and 16 degree cases, whereby the leeward side measurements (at the same radial location magnitude) are lower than those on the windward side. For the current experiments, no transition is expected or observed given the Reynolds number and the scale of the model.

In each case, for Figures 5.18-5.20, the experimental measurement is compared to non-catalytic and super-catalytic surface boundary condition simulations. In general, accounting for the experimental uncertainty, the data falls within the bounds of the two solutions. Due to the lower degree of freestream dissociation in the HET compared to LENS I for the same stagnation enthalpy, the relative difference between the non-catalytic and super-catalytic solutions is not as large. Unfortunately, this smaller difference and the experimental uncertainty of the gages means that it is not possible to conclude which boundary condition provides the best agreement.

At all three angles of attack, experimentally measured heat fluxes at the outermost extent of the model are above the super-catalytic solution. Such a result appears to be anomalous as the super-catalytic solution enforces full surface recombination, irregardless of the local species mole fractions, and therefore represents an aphysical upper bound on the heat flux. Hollis et al. observed windside heating augmentation, which was not found to correlate with Reynolds Number, in the LENS I facility [2]. In this study, however, both windside and leeside elevated heating levels are observed. At this stage, the reason for this observation is unknown.

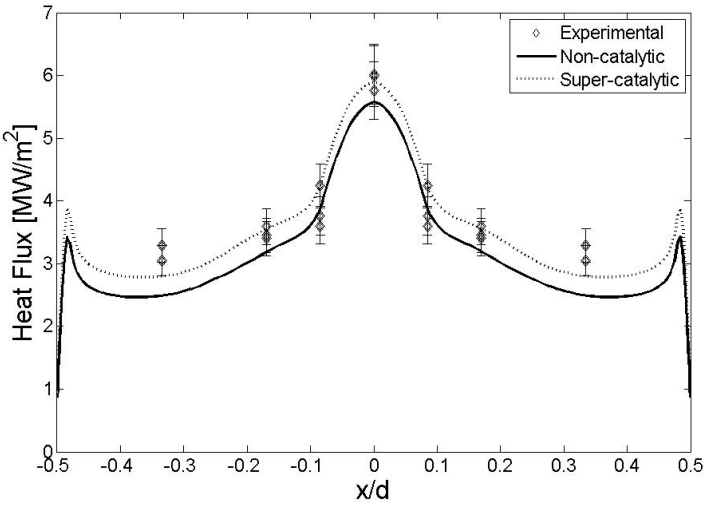

Figure 5.18: Heat flux measurements at selected locations along the centerline of the MSL geometry for 0 degree angle of attack. Numerical simulations for both non-catalytic and super-catalytic conditions are shown.

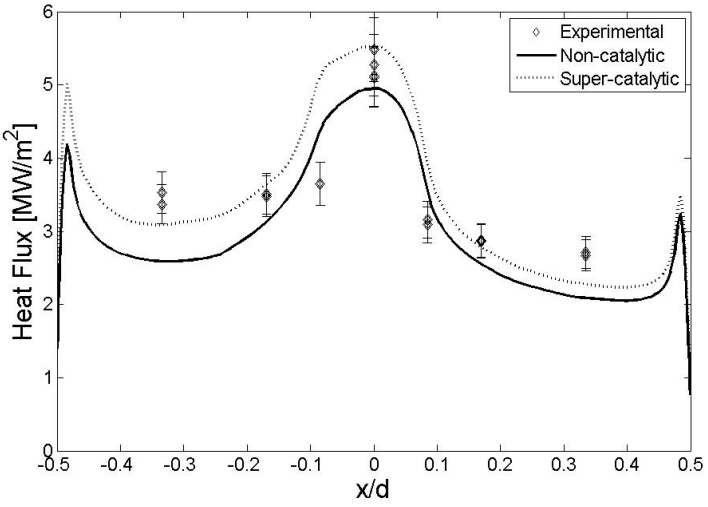

Figure 5.19: Heat flux measurements at selected locations along the centerline of the MSL geometry for 11 degree angle of attack. Numerical simulations for both non-catalytic and super-catalytic conditions are shown.

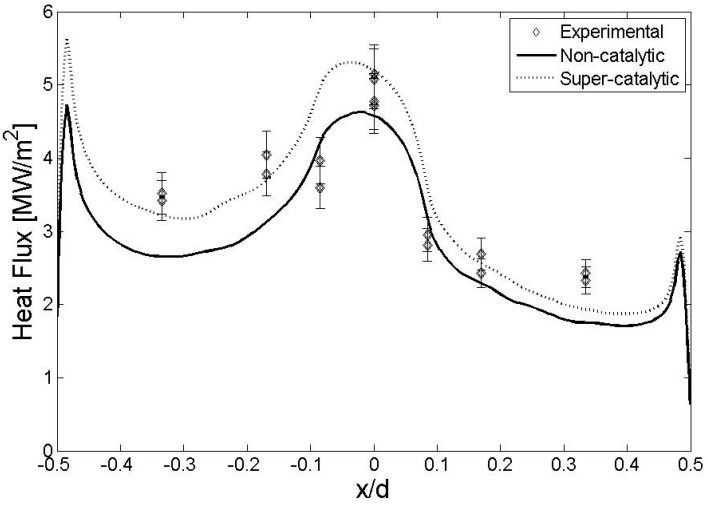

Figure 5.20: Heat flux measurements at selected locations along the centerline of the MSL geometry for 16 degree angle of attack. Numerical simulations for both non-catalytic and super-catalytic conditions are shown.

CHAPTER 6

CONCLUSIONS

6.1 Summary of Completed Work

The overall goal of this work has been to investigate the coupling between fluid mechanics and thermochemistry in hypervelocity flow by concentrating upon post-shock flowfields in air and carbon dioxide. Two canonical flow fields were selected - a stationary normal shock (air) and a bow shock (carbon dioxide) over bluff bodies. Experiments have been conducted in the Hypervelocity Expansion Tube (HET) at the University of Illinois at Urbana-Champaign.

In the first part of this work, results were presented towards more rigorously characterizing test gas properties than what was previously capable. A parameter, the total characteristic acoustic impedance across the secondary diaphragm, was experimentally identified as correlating test gas noise levels. Theoretical analysis indicated the importance of this quantity in pitot pressure fluctuation and resulted in an improved non-dimensional correlation. Established theoretical models have also been applied to the HET for core flow calculations based upon either laminar or turbulent boundary layer development within the acceleration section.

In the high-enthalpy air study, emission spectroscopy was used to measure nitric oxide and hydroxyl radical vibrational temperatures behind a strong normal shock. The stationary normal shock is created via a Mach reflection using an opposing wedge model in a high enthalpy Mach 7.42 air freestream in an expansion tube facility. The inflow conditions for the normal shock have been experimentally defined by pressure, velocity and shock angle measurements. Experimental spectral data from the NO and OH A-X band sequences were

collected at selected locations, 1 mm apart, behind the Mach stem. OH temperature fits were conducted using simulated spectra generated by LIFBASE, whereas the NO fits required higher vibrational and rotational levels and the use of an in-house spectral simulation algorithm. A state-resolved thermochemical model was used to calculate the NO A-state temperature profile up to 5 mm downstream of the Mach stem. Very good agreement is obtained between NO vibrational measurements and computations. As has been reported for previous studies of flight data, the temperatures calculated from OH emission differ significantly from those of other species in these non-equilibrium flows. These results extend previous studies applying emission spectroscopy for test gas identification in impulse facilities and demonstrate the measurement of species vibrational temperatures in an expansion tube.

Experiments were conducted in an expansion tube facility to visualize bow shock shapes and measure heat flux over blunt bodies in a hypervelocity carbon dioxide flow. The blunt bodies of interest are spheres of varying diameters and a scaled version of the Mars Science Laboratory aeroshell. This study was motivated by previous experiments at the CUBRC hypervelocity facilities which found that substantially different shock stand-off distances were measured in different impulse facilities. One contributing factor is that the free stream carbon dioxide thermochemistry depends on the means by which the flow is accelerated to high velocities. To address this question and provide complementary results to those from CUBRC, experiments were carried out in the Hypervelocity Expansion Tube. Experimental shock layer shapes for different geometries, including spheres and the MSL forebody, are compared with simulations using the University of Minnesota solver, US3D, which incorporates detailed CO_2 thermochemical modeling.

A test condition, labeled RC5, was selected by using first-order matching with the test gas velocity to match the stagnation enthalpy of a CUBRC test condition. Spheres with varying diameters were chosen as benchmark models for which shock stand-off distances could be compared with existing data and theory. Excellent agreement was obtained between

simulation and experiment for different diameters. Sphere stagnation point heat transfer measurements were in good agreement with semi-empirical fits and non-catalytic numerical results.

The scaled MSL model was next tested in this flow field. Shock shapes were visualized and heat transfer measurements were made at three different angles of attack: 0, 11, and 16 degrees. Excellent agreement was obtained between measured shock shapes and both CUBRC LENS X results and numerical simulations, implying that the stagnation enthalpy and velocity are reasonable first-order matching parameters for these measurements in different expansion tube facilities. The results confirm facility-independence for the same type of flow acceleration. The heat transfer data follow the general trends observed in previous experiments. Peak-heating shifted to the windward side with non-zero angle of attack. Windward side heat transfer values appear quite insensitive to angle of attack, while the leeward side values decrease appreciably with increasing angle of attack. In general, accounting for the experimental uncertainty, the data falls within the bounds of the two non-catalytic (lower) and super-catalytic (upper) numerical solutions.

6.2 Future Work

6.2.1 High Enthalpy CO_2 Aerothermodynamics

The above results indicate the promise of the HET for future high-enthalpy CO_2 studies. With considerably reduced freestream dissociation, the expansion tube is an alternative high-enthalpy ground-test facility which offers certain advantages over reflected shock tunnels. The CO_2 aerothermodynamics literature has identified key areas of required improvement, some which can be addressed by an expansion tube such as the HET. Hollis et al. commented that due to the sizes of the MSL models, no fully-laminar baseline data exists [2]. Due to the smaller model sizes and lower Reynolds Numbers, these fully laminar conditions can be

obtained in the HET. The RC5 core flow size is approximately twice the size of the current model (Table 5.3). Larger blunt body geometries could be tested and a larger version of the MSL forebody aeroshell explored for possible transition. More importantly, this permits much larger spherical diameters and shock stand-off distances - leading to the potential of measurement within the shock layer itself using spectroscopic or scattering based techniques.

In this work, the computational simulations indicated that the effect of catalysis is not so pronounced within the HET and experimental comparison revealed that no clear agreement with either non-catalytic or super-catalytic solutions could be achieved. Towards resolving this specific issue, and high-enthalpy CO_2 catalysis effects in general, heat transfer measurements could be obtained on models made from a non-catalytic material such as MACOR®. Models could also be instrumented with thin-film gauges, already with demonstrated application within the HET [129], which have the advantage of higher signal-to-noise ratios than the co-axial thermocouples. Recent improvements in pressure sensitive paint response times permit application to hypersonic flows, for which model surface pressure distributions can be compared with numerical results.

Identifying a set of HET run conditions, across which vibrational relaxation model sensitivity is seen, would be very useful for model validation. A candidate parameter to evaluate this sensitivity is the binary scaling, ρd. Figure 6.1 shows practical operating ranges of the HET for the binary scaling, ρd, plotted against the test gas stagnation enthalpy.

6.2.2 Spectroscopic Diagnostic Capabilities

From a purely gas property measurement perspective, the successful demonstration of emission spectroscopic techniques within the HET indicates that fluorescence spectroscopy should be pursued. With point-like measurement characteristics (as opposed to absorption spectroscopy averaged line-of-sight measurements), the technique has the advantage of resolving future flow fields in the HET that are expected to be physically small. Examples include very small shear layers, due to hypersonic fluid mechanics, and very thin boundary layers

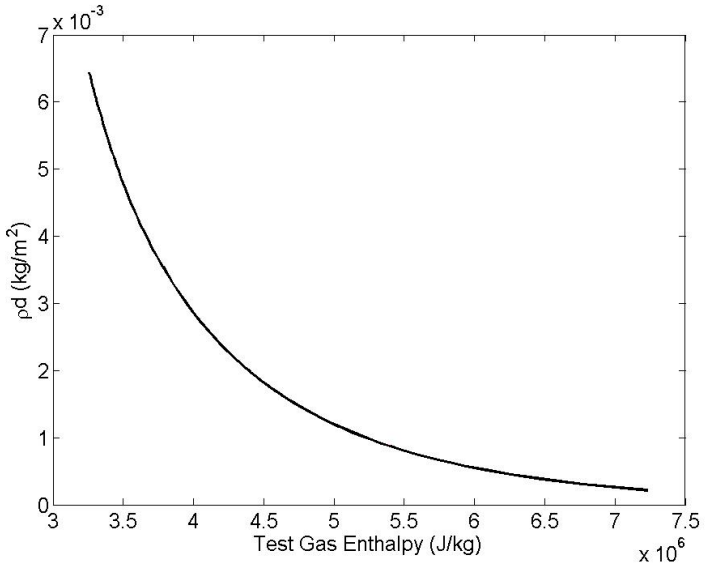

Figure 6.1: Binary scaling parameter vs. CO_2 test gas stagnation enthalpy for a 2 inch diameter.

due to restrictions on the model size. Furthermore, fluorescence spectroscopy is not confined to measuring naturally "hot" flow fields, such as post-shock relaxation regions, but can be applied to boundary layers and separation zones where sufficiently high upper-level populations would not be present.

In the intermediate stage, with judicious selection of the measurement region, absorption spectroscopy could be applied within the HET. For larger shock stand-off distances, achieved via cylindrical as opposed to spherical geometries and with sufficient thermal equilibrium extent (as seen in the current study), absorption spectroscopy could be used to measure shock layer temperatures.

APPENDIX A

EXTENDED ANALYSIS

A.1 Boundary Layer Calculations

For the calculation of laminar and turbulent boundary layer thicknesses, strong ideal shocks with perfect gas flows are assumed. According to Mirels [47], the ideal shock calculations are valid when the transmitted shock Mach number, M_t, is less than 6. All of the run conditions considered in this work have transmitted shock Mach numbers below this value. Mirel's theory is derived for a shock fixed co-ordinate system, such that u_w=u_t and $u_{e,0}$=$u_w - u_{67}$. Referencing Mirel's notation, subscript e denotes the region in between the transmitted shock and the secondary contact surface, and subscript inf denotes conditions upstream of the shock. It is assumed that the freestream region between the transmitted shock and the secondary contact surface, state 6, is inviscid and uniform so that $\rho_{e,0} = \rho_6$. Upstream conditions of the shock correspond to state 5.

At the core of Mirel's theory is the concept of the maximum separation length between shock and contact surface, l_m. At this point, the shock and the contact surface will be moving with the same velocity, following the deceleration of the shock and acceleration of the contact surface due to mass entrainment by the developing boundary layer. l_m is calculated by

$$l_m = \left[\frac{d\rho_6 u_{e,0}}{4\beta_1 \rho_5 \left(u_w - u_{e,0}\right)} \left(\frac{u_w - u_{e,0}}{\nu_5} \right)^n \right]^{1-n} \tag{A.1}$$

where n is equal to 1/2 and 1/5 for laminar and turbulent boundary layers respectively, ν is the kinematic viscosity and β_1 is a correlating constant which is calculated differently depending on the state of the boundary layer. The maximum separation length is incorporated within the definition of two non-dimensional variables, T and X

$$T = \frac{l}{l_m} \qquad\qquad X = \frac{u_{e,0} t}{l_m} \tag{A.2}$$

In the following equations, the quantities, W and Z, are defined as

$$W = \frac{u_w}{u_{e,0}} \qquad\qquad Z = \frac{\gamma_5 + 1}{\gamma_5 - 1} \tag{A.3}$$

A.1.1 Laminar Prediction

For laminar flow, the relationship between X and T is

$$X = -2\left[\ln\left(1 - T^{1/2}\right) + T^{1/2}\right] \tag{A.4}$$

The boundary layer thickness is calculated using

$$\delta = \beta_1 \left(\frac{\mu_5 l}{\rho_5 u_{e,0}}\right) \tag{A.5}$$

where the constant, β_1, is

$$\beta_1 = 1.59 C_{e,0}\left[1 + \frac{1.796 + 0.802W}{ZW - 1}\right] \qquad\qquad C_{e,0} = \frac{\rho_6 \mu_6}{\rho_5 \mu_5} \tag{A.6}$$

β_1 is in fact an approximation to the parameter, β, which in the generalized form of Mirel's theory supplants β_1 in Equation A.1. In the laminar case, Mirel presents 3 methods to approximate β and in this case β_1 was chosen due to ease in implementation.

A.1.2 Turbulent Prediction

The relationship between T and X is

$$X = -\frac{5}{4}\left[\ln\left(\frac{1 - T^{1/5}}{1 + T^{1/5}}\right) - 2\tan^{-1}\left(T^{1/5}\right) + 4T^{1/5}\right] \tag{A.7}$$

In order of computation, the values to be calculated for a turbulent boundary layer are

$$\beta_0 = \frac{p_5 W K_0}{p_6 (W-1)} \tag{A.8}$$

$$\beta_1 = \beta_0 \left[\frac{W^2 + 1.25W - 0.80}{W(W-1)}\right]^{4/5} \tag{A.9}$$

$$\mathrm{Pr} \approx \frac{4\gamma_5}{15\gamma_5 - 15} \tag{A.10}$$

$$\frac{h_r}{h_{e,0}} = 1 + \frac{(W-1)^2}{ZW-1}\mathrm{Pr}^{1/3} \qquad \frac{h_{e,0}}{h_5} = \frac{ZW-1}{W(Z-W)} \qquad \frac{h_r}{h_5} = \frac{h_r}{h_{e,0}} \cdot \frac{h_{e,0}}{h_5} \tag{A.11}$$

$$b = \frac{h_r}{h_5} - 1 \qquad\qquad c = \frac{h_r - h_{e,0}}{h_5} \tag{A.12}$$

$$T_m = T_6\left[0.5\left(\frac{h_5}{h_{e,0}} + 1\right) + 0.22\left(\frac{h_r}{h_{e,0}} - 1\right)\right] \qquad \rho_m = \rho_6\left(\frac{T_m}{T_6}\right)^{1/(\gamma_5 - 1)} \tag{A.13}$$

$$\frac{\delta^*/\delta}{1-W} = \frac{1}{W-1}\left\{\frac{7h_{e,0}}{h_5}\int_0^1 \frac{\zeta^6\left[W - (W-1)\zeta\right]}{1 + b\zeta - c\zeta^2} d\zeta - 1\right\} \tag{A.14}$$

$$\frac{\theta/d}{1-W} = \frac{7h_{e,0}}{h_5}\int_0^1 \frac{\zeta^6\left[W - (2W-1)\zeta + (W-1)\zeta^2\right]}{1 + b\zeta - c\zeta^2} d\zeta \tag{A.15}$$

$$K_0 = 0.0575\frac{\delta^*/\delta}{1-W}\left(\frac{1-W}{\theta/d}\right)^{4/5}(W-1)^{9/5}\left(\frac{\mu_m \rho_5 \rho_m^3}{\mu_w \rho_6^4}\right)^{1/5} \tag{A.16}$$

$$\delta^* = -K_0 l^{4/5}\left(\frac{\upsilon_5}{u_w - u_{e,0}}\right)^{1/5} \tag{A.17}$$

The turbulent boundary layer thickness can then be evaluated using Equation A.17 and the fact that the right hand side of Equation A.14 is known.

A.2 Mach Reflection Configuration Selection

Pressure-deflection shock polars are considered very convenient for analyzing phenomena involving shock wave reflections [149]. They essentially represent the locus of all possible static pressures behind an oblique shock wave as a function of the deflection angle for given upstream conditions [150]. A Mach reflection will have 3 different polars and Figure A.1 shows an example pressure-deflection diagram. There are obviously an infinite number of possible combinations of the three polars, however, in order to guarantee that only a Mach reflection is possible then the R_1 and R_2 polars should never intersect.

There are two main considerations to take into account in regards to the wedge design and their mounting - the inlet aspect ratio (IAR) and wedge aspect ratio (WAR). The IAR and WAR are defined as:

$$IAR = \frac{b}{h} \tag{A.18}$$

$$WAR = \frac{2b}{c} \tag{A.19}$$

where b, h and c are the wedge half-span, leading edge separation and wedge chord length respectively. Based off a theoretical study of aspect ratio effects, Skews suggests that the IAR be at least 1.25 [104] in order to eliminate three-dimensional effects such as edge reflection off the wedges. Unfourtunately due to design constraints, the original wedges only inlet aspect ratios of 0.75. For a Mach reflection, the WAR needed for the flow to be esentially two-dimensional is difficult to determine [104], however, the tests of Ivanov et al [151] suggest that 2.5 should be sufficient. A backing plate was used in order to mount the wedges to a certain portion of the flatted area of the sting. Due to the large diameter of the sting rod, the wedges were initially mounted to the backing plate and then connected to the sting from the front. Factors which shaped the sizing of the backing plate included: minimizing its area due to stagnation loading, sufficient width to ensure clearance for the 4 hole wedge connections and sufficient height to allow at least 3 sockethead capscrew sting rod connections. The back central portion of each wedge was removed in order to permit tool access clearance for

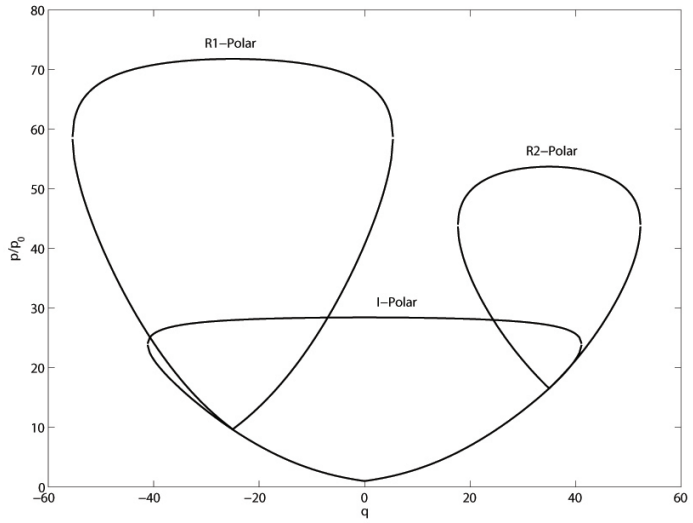

Figure A.1: Pressure-deflection polar for a flow Mach number of 4.95, with wedge angles of θ_1=25^o and θ_2=35^o. Assumptions are: steady flow, weak shock solution and a perfect gas.

the sting rod capscrew connections. The backing plate area had to be minimized, whilst ensuring its structural integrity and sufficient clearance for the 4 hole connections between each wedge.

For known top and bottom wedge angles, θ_1 and θ_2, the code requires the input of these two values. For a certain run condition (and hence inflow Mach number) we need determine the maximum θ value above which detachment would occur.

$$M_0^* = \sqrt{\frac{M_0^2(\gamma+1)}{2+M_0^2(\gamma-1)}} \tag{A.20}$$

The minimum and maximum V_x values for State 0 are given by:

$$\left(V_{x,min}^*\right)_0 = \frac{1}{M_0^*} \tag{A.21}$$

$$\left(V_{x,max}^*\right)_0 = M_0^* \tag{A.22}$$

Iteration is then required to find values of $V^*_{y,0}$ and θ for each value of $V^*_{x,0}$ between its minimum and maximum values. The values of $V^*_{y,0}$ and θ are given by:

$$V^*_{y,0} = \sqrt{\frac{\left(M^*_0 - V^*_{x,0}\right)^2 \left(V^*_{x,0} M^*_0 - 1\right)}{\frac{2}{\gamma+1}\left(M^*_0\right)^2 - V^*_{x,0} M^*_0 + 1}} \tag{A.23}$$

$$\theta = \tan^{-1}\left(\frac{V^*_{y,0}}{V^*_{x,0}}\right) \tag{A.24}$$

θ_{max} can then be determined after these iterative calculations. We then need to check that $\theta_{max} > \theta_1$ and $\theta_{max} > \theta_2$ so that no detached shocks occur at either of the wedges. The code uses an iterative solver loop in order to determine β_1 from the expression:

$$\tan\theta = 2\cot\beta\left[\frac{M_0^2 \sin^2\beta - 1}{M_0^2(\gamma + \cos 2\beta) + 2}\right] \tag{A.25}$$

The normal component of the inflow Mach number, $M_{n,1}$ can be found from:

$$M_{n,0} = M_0 \sin\beta_1 \tag{A.26}$$

This provides the normal component of State 1's Mach number, $M_{n,1}$:

$$M_{n,1} = \frac{M^2_{n,0} + \frac{2}{\gamma-1}}{\frac{2\gamma}{\gamma-1} M^2_{n,0} - 1} \tag{A.27}$$

Therefore, State 1 Mach number conditions, M_1 and M^*_1 are:

$$M_1 = \frac{M_{n,1}}{\sin\beta_1 - \theta_1} \tag{A.28}$$

$$M^*_1 = \sqrt{\frac{M_1^2(\gamma+1)}{2 + M_1^2(\gamma-1)}} \tag{A.29}$$

Following the steps described previously, $V_{x,1}$, $V_{y,1}$ and also $\theta_{1,max}$ are obtained. The steps used for State 1 calculations can then be used to get β_2, $M_{n,2}$, M_2 and M^*_2, which in turn

will give $V_{x,2}$,$V_{y,2}$ and $\theta_{2,max}$.

Using the following expressions [150]:

$$\lambda = \sqrt{\left[\left(M_0^2-1\right)^2 - 3\left(1+\frac{\gamma-1}{2}M_0^2\right)\left(1+\frac{\gamma+1}{2}M_0^2\right)\tan^2\theta\right]} \tag{A.30}$$

$$\chi = \frac{\left(M_0^2-1\right)^3 - 9\left(1+\frac{\gamma-1}{2}M_0^2\right)\left(1+\frac{\gamma_1}{2}M_0^2+\frac{\gamma+1}{4}M_0^4\right)\tan^2\theta}{\lambda^3} \tag{A.31}$$

$$\tan\beta = \frac{M_0^2 - 1 + 2\lambda\cos\left[\frac{\left(4\pi\delta+\cos^{-1}\lambda\right)}{3}\right]}{3\left(1+\frac{\gamma-1}{2}M_0^2\right)\tan\theta} \tag{A.32}$$

With δ=0 for a strong shock solution and δ=1 for a weak shock solution. We can then determine the pressure ratio from:

$$\frac{p_1}{p_0} = 1 + \frac{2\gamma}{\gamma+1}\left(M_0^2\sin^2\beta - 1\right) \tag{A.33}$$

We know that $\theta_1 = 25$ degrees and $\theta_2 = 35$ degrees, which provides us with the starting points of the R_1 and R_2 polars on the I-Polar. We can then use the process used above in order to calculate λ, χ and β for each possible θ in order to produce curves for both the strong and weak shock solutions. It must be remembered, however, that the calculated pressure ratio only represents the local pressure ratio across the reflected shock. The total pressure ratio (across both the incident and reflected shock) is easily obtained by multiplying by the incident pressure ratio previously determined. Both reflected shocks aim to move the slipstreams entering regions 3 and 4 towards a total deflection of 0 degrees and therefore by the boundary conditions described in Equations 4.1 and 4.2, the local θ can be determined. From Equation A.25, the reflected shock angles of β_3 and β_4 can then be calculated.

Term	Energy (cm^{-1})	Λ
$^2\Pi_{1/2}$	0	1
$^2\Pi_{3/2}$	119.8	1
$^2\Sigma^+$	43966	0

Table A.1: Electronic energy and term description for the NO A-X transition.

A.3 NO A-X Transition Energy Calculations

In Table A.1, we see that the ground-state actually consists of two terms (with terms $^2\Pi_{1/2,3/2}$) and is known as a *doublet*. Along with orbital behavior, molecules also spin about their own axes. This is characterized by the orbital and spin angular momentum vectors, L and S respectively. In the case of diatomic molecules, only the components of L and S along the internuclear axis need to be considered. Along the internuclear axis (IA), these components are

$$L_{IA} = \pm\Lambda\hbar \quad \Lambda = 1, 2, ... \tag{A.34}$$

$$S_{IA} = \Sigma\hbar \quad \Sigma = -S, -S+1, ..., S-1, S \tag{A.35}$$

We see that for every value of S, there are $2S+1$ values of S_{IA}, its component along the internuclear axis. The magnitude of $2S+1$ is known as the *multiplicity*; thus, the NO ground-state has a multiplicity of 2 and results in two possible transitions from the excited A state that contribute to the emission spectra observed in this work. This two-fold degeneracy is known as Λ-*doubling* and occurs due to the coupling between the spin and orbit vectors. Electromagnetic theory predicts that the motion of a rotating electron will induce a magentic dipole moment vector. Similarly, a molecule rotating about its own axis will also induce a magnetic field. Furthermore, a basic property of spin is magnetic momentum. Hence, an interaction takes place between the induced magnetic vectors and the orbiting motion which causes torque; the angular momentum and spin vectors will precess around the total angular momentum vector. This is known as *spin-orbit* coupling and affects the multiplet splitting phenomenon described above.

These features will alter the wavelength of the spectral lines. For the type of vibrational temperature calculation in this study, a fine-scale spectral resolution must be implemented and as a result, any spectral simulation program must incorporate the Λ-doubling and spin-orbit coupling.

The electronic, T_e, rotational, $F_\upsilon(J)$, and vibrational, $G(\upsilon)$, modes when summed together provide the total internal energy of a diatomic molecule, where single and double primes denote upper and lower states respectively

$$\tilde{\varepsilon}_{\text{int}}^{',''} = T_e^{'} + G(\upsilon) + F_\upsilon^{',''}(J) \tag{A.36}$$

The expression used for the vibrational energy, G(υ) is

$$G(\upsilon) = \omega_e(\upsilon + 1/2) - \omega_e x_e(\upsilon + 1/2)^2 + \omega_e y_e(\upsilon + 1/2)^3 \tag{A.37}$$

This is a 3rd-order type Dunham expansion, which accounts for anharmonicity. Due to the doublet ground state, different expressions are used for the rotational energy depending on whether an upper or ground state calculation is performed

$$F_\upsilon^{'}(J) = B_\upsilon^{'}J(J+1) - D_e^{'}J^2(J+1)^2 \tag{A.38}$$

$$F_\upsilon^{''}(J) = B_\upsilon^{''}\left[(J+1)^2 - 1 \pm \frac{1}{2}\sqrt{Y(Y-4) + 4(J+1)^2}\right] - D_e^{''}J^2(J+1)^2 \tag{A.39}$$

The parameter, Y, is $\frac{A}{B_\upsilon''}$ and for NO A-X calculations only lower-level values are required. In equation A.39, the negative sign is used for the $^2\Pi_{1/2}$ term and the positive sign for the $^2\Pi_{3/2}$. The term, D_e, accounts for rotational centrifugal stretching. Additionally, the term B_υ is dependent upon the vibrational quantum number (rotation-vibration coupling) such that

$$B_\upsilon = B_e - \alpha_e(\upsilon + 1/2) \tag{A.40}$$

Constant	NO $X^2\prod$	NO $A^2\sum^+$
ω_e	1904.13455	2374.372
$\omega_e x_e$	14.088358	16.159
$\omega_e y_e$	0.0100467	0.0373
B_e	1.70488847	1.995586
α_e	0.01754158	0.018714

Table A.2: Spectroscopic constants used for the in-house simulation program

The values used in all of these expressions are summarized in Table A.3. The Hönl-London factors for the 12 different branches associated with doublet transitions with $Delta\Lambda = 1$ are listed in Table A.3. As vibrational excitation inherently involves rotational excitation, ro-vibrational coupling occurs which manifests itself in the spectrum via so-called P,Q and R branches. P branches are located at wavelengths above a fundamental vibrational line, ω_e, and R branches labelled for those with lower wavelengths. Subsequently, based upon the selection rules for ro-vibrational transitions, the P-branch involves $J^{'} = J^{''} - 1$ while R-branch involves $J^{'} = J^{''} + 1$. Q-branches can arise for the case when $\Delta J = 0$.

In the above table, the following definitions are required

$$u^{'\pm}(J) = 2(J + 1/2) \tag{A.41}$$

$$u^{''\pm}(J) = \sqrt{Y(Y-4) + 4(J+1/2)^2} \pm (Y-2) \tag{A.42}$$

$$C^{'\pm}(J) = \frac{1}{2}\left[u^{'\pm}(J)^2 + 4(J+1/2)^2\right] \tag{A.43}$$

$$C^{'\pm}(J) = \frac{1}{2}\left\{u^{'\pm}(J)^2 + 4[(J+1/2)^2 - 1]\right\} \tag{A.44}$$

As discussed in 4.4.5 A is the spin-orbit parameter and calculated via the third-order expression

$$A = 123.252407 - 0.235702\upsilon - 0.0040762\upsilon^2 - 0.00018629\upsilon^3 \tag{A.45}$$

Branch	Line Strength
$R_1(J)$	$\frac{(J-1/2)(J+1/2)\left[u'^{-}(J)u''^{-}(J+1)+4(J+1/2)^2\right]^2}{8(J+1)C'^{-}(J)C''^{-}(J+1)}$
$Q_1(J)$	$\frac{(J-1/2)(J+1/2)(J+3/2)\left[u'^{-}(J)u''^{-}(J)+4(J+1/2)^2\right]^2}{4J(J+1)C'^{-}(J)C''^{-}(J)}$
$R_1(J)$	$\frac{(J+1/2)(J+3/2)\left[u'^{-}(J)u''^{-}(J-1)+4(J+1/2)^2\right]^2}{8JC'^{-}(J)C''^{-}(J-1)}$
${}^{Q}R_{12}(J)$	$\frac{(J-1/2)(J+1/2)\left[u'^{+}(J)u''^{-}(J+1)-4(J+1/2)^2\right]^2}{8(J+1)C'^{+}(J)C''^{-}(J+1)}$
${}^{P}Q_{12}(J)$	$\frac{(J-1/2)(J+1/2)(J+3/2)\left[u'^{+}(J)u''^{-}(J)-4(J+1/2)^2\right]^2}{4J(J+1)C'^{+}(J)C''^{-}(J)}$
${}^{O}P_{12}(J)$	$\frac{(J+1/2)(J+3/2)\left[u'^{+}(J)u''^{-}(J-1)-4(J+1/2)^2\right]^2}{8JC'^{+}(J)C''^{-}(J-1)}$
${}^{S}R_{21}(J)$	$\frac{(J-1/2)(J+1/2)\left[u'^{-}(J)u''^{+}(J+1)-4(J+1/2)^2\right]^2}{8(J+1)C'^{-}(J)C''^{+}(J+1)}$
${}^{R}Q_{21}(J)$	$\frac{(J-1/2)(J+1/2)(J+3/2)\left[u'^{-}(J)u''^{+}(J)-4(J+1/2)^2\right]^2}{4J(J+1)C'^{-}(J)C''^{+}(J)}$
${}^{Q}P_{21}(J)$	$\frac{(J+1/2)(J+3/2)\left[u'^{-}(J)u''^{+}(J-1)-4(J+1/2)^2\right]^2}{8JC'^{-}(J)C''^{+}(J-1)}$
$R_2(J)$	$\frac{(J-1/2)(J+1/2)\left[u'^{+}(J)u''^{+}(J+1)+4(J+1/2)^2\right]^2}{8(J+1)C'^{+}(J)C''^{+}(J+1)}$
$Q_2(J)$	$\frac{(J-1/2)(J+1/2)(J+3/2)\left[u'^{+}(J)u''^{+}(J)+4(J+1/2)^2\right]^2}{4J(J+1)C'^{+}(J)C''^{+}(J)}$
$P_2(J+1)$	$\frac{(J+1/2)(J+3/2)\left[u'^{+}(J)u''^{+}(J-1)+4(J+1/2)^2\right]^2}{8JC'^{+}(J)C''^{+}(J-1)}$

Table A.3: Line strengths for NO A-X doublet transitions.

A.4 Shock Stand-off Distance Calculations

A.4.1 Wen and Hornung

In his dissertation [144] and in his Journal of Fluid Mechanics paper, Wen defines the non-dimensional reaction rate parameter to be

$$\tilde{\Omega} = \frac{d}{\rho_s u_\infty} \left(\frac{1}{h_\rho} \sum_{i=2}^{n} h_{c_i} \frac{dc_i}{dt} \right)_s \tag{A.46}$$

here c is the mass fraction. All other variables have been previously defined. Subscripts i and s refer to individual species and directly post-shock values respectively. h_ρ is the partial derivative of the static enthalpy with respect to the density. The calculation of h_ρ requires first determining Γ and the mixture specific heat, c_p (from the individual species specific heats, c_{pi}. A total of 4 species were considered for the dissociating CO_2 shock layer: CO_2, CO, O_2 and O.

$$\Gamma = \sum_{i=1}^{4} \frac{c_i}{MW_i} \tag{A.47}$$

$$c_{pi}(T) = \frac{1000}{MW_i} \left(A + Bt + Ct^2 + Dt^3 + E/t^2 \right) \qquad t = \frac{T}{1000} \tag{A.48}$$

$$c_p = \sum_{i=1}^{4} c_i c_{pi} \tag{A.49}$$

$$h_\rho = -\frac{c_{ps} \rho_\infty u_\infty^2}{\rho_s^2 R \Gamma} \tag{A.50}$$

In the above equations, MW is the molecular weight. The quantity h_{c_i} is calculated as

$$h_{c_i} = (h_i - h_1) - \frac{c_{ps} T}{\Gamma} \left(\frac{1}{MW_i} - \frac{1}{MW_1} \right) \tag{A.51}$$

The post-shock mass fraction rates are supplied from the numerical calculations. The post-shock conditions directly behind the shock are taken to be the values at which the translational temperature is a maximum.

A.4.2 Theory of Inger, Higgins and Morgan

For axisymmetric flow, the shock stand-off distance is calculated as

$$\Delta = \frac{u_\infty \rho_\infty}{2} \int_0^1 \frac{1}{\beta_s(\eta)\rho(\eta)} d\eta \tag{A.52}$$

η is a density stretched coordinate, ranging from 0 at the body to 1 at the shock. In this study, it is calculated via the compressible Howard-Dorodnitsyn transformation applied by Inger et al [139]

$$\eta = \frac{\rho u}{\rho_\infty u_\infty} \tag{A.53}$$

In Equation A.52, β_s is determined via

$$\beta_s = \frac{\rho(x)u(x)}{2\int_0^x \rho dx} \tag{A.54}$$

In their theory, Inger et al. state that β_s should be a constant. However, evaluation of β_s from Equation A.54 reveals a variation of β_s with the axial coordinate. As a result, Equation A.52 is evaluated by bringing β_s inside the integral. Using a varying β_s value instead of an average (constant) β_s resulted in approximately a 5% change in calculated shock stand-off distance. In Equation A.52, the variation of the density and β_s with distance, $\rho(\eta)$ and $\beta_s(\eta)$ respectively, are determined by using the numerically calculated density and axial stagnation line data. As it is an inviscid calculation, the boundary layer portion of the numerical data is ignored. For each sphere diameter, $\rho(\eta)$ is fitted to an 8th-order polynomial and $\beta_s(\eta)$ to a cubic. The shock stand-off distance was then obtained via numerical integration.

APPENDIX B

DRAWINGS

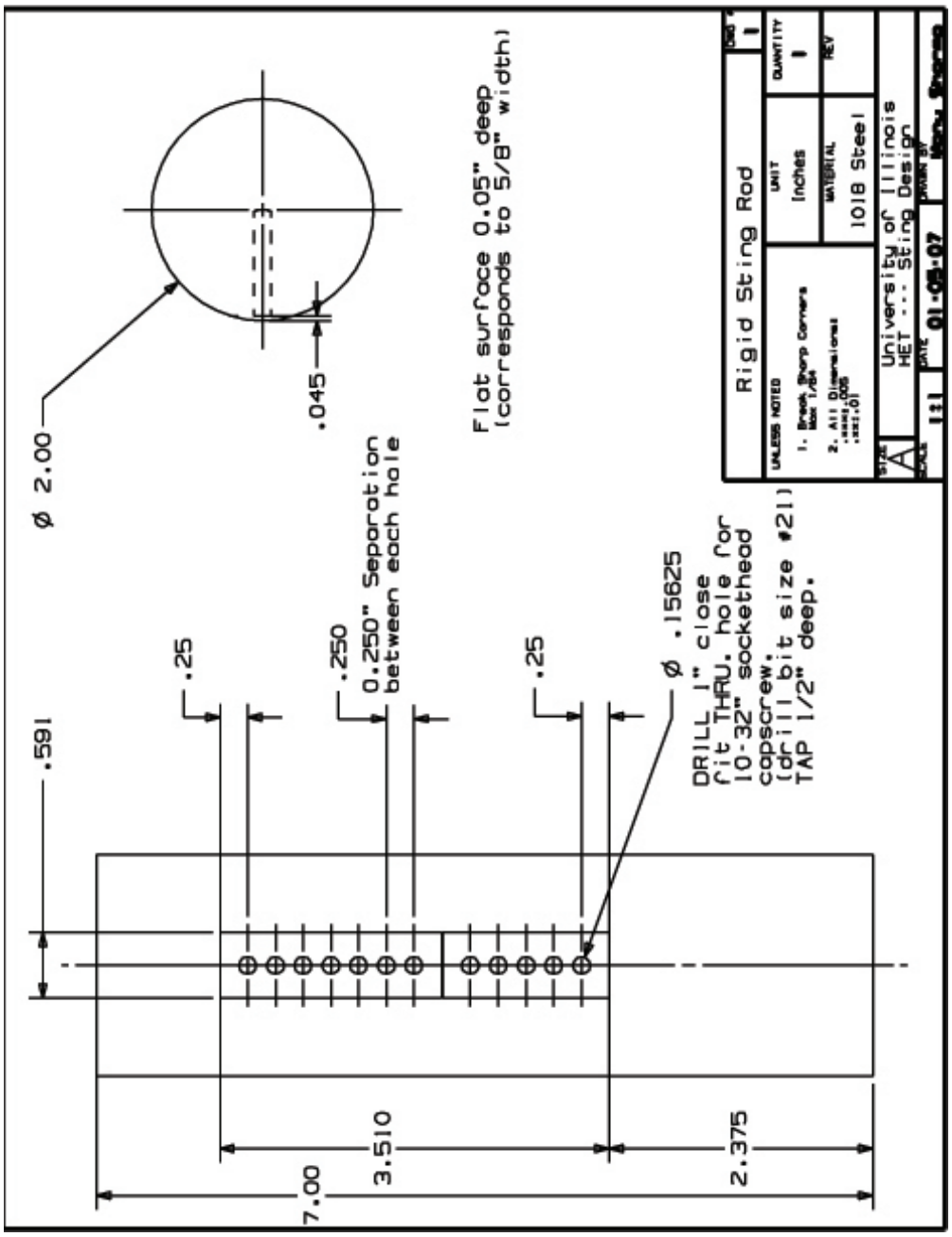

Figure B.1: Sting rod.

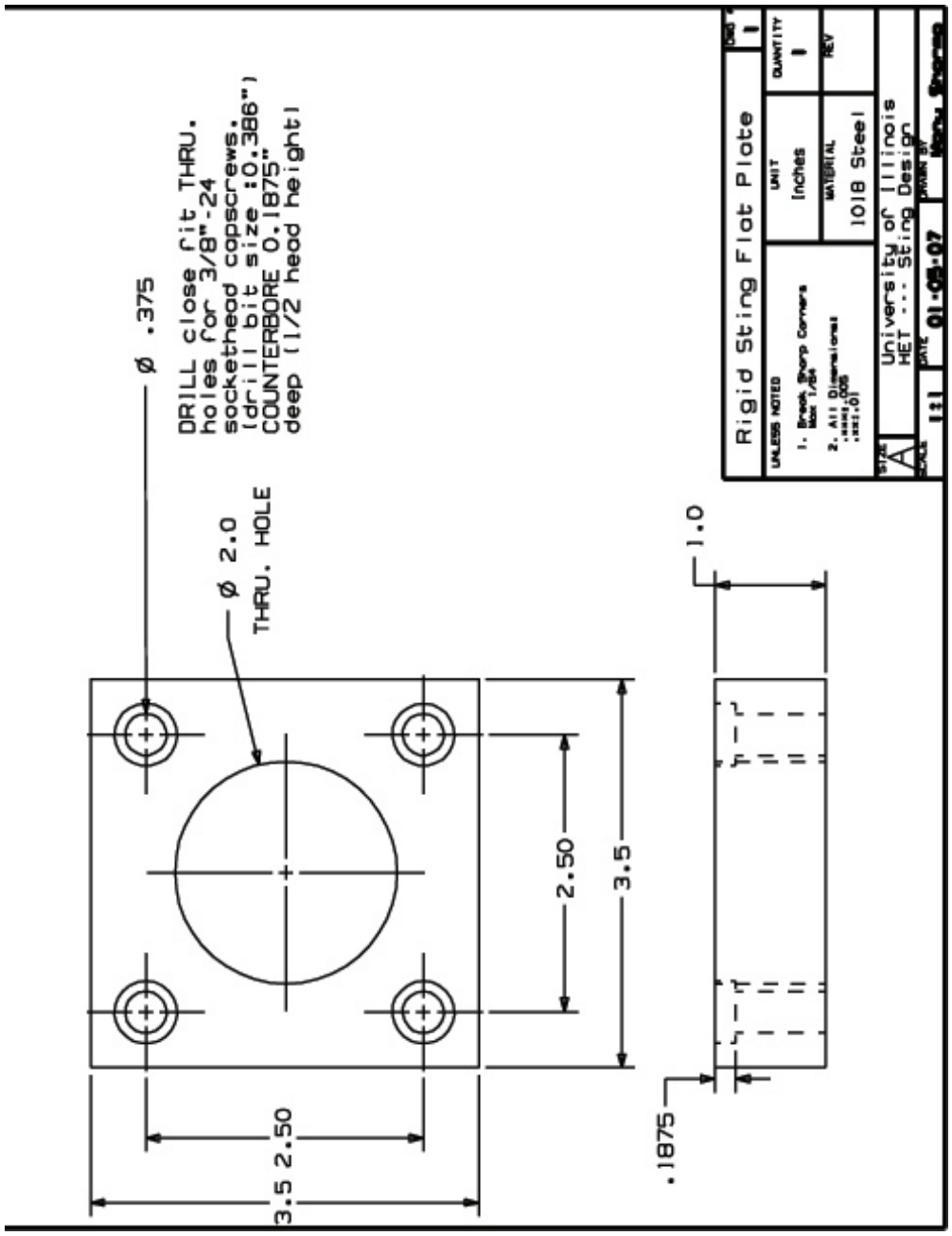

Figure B.2: Sting flat plate.

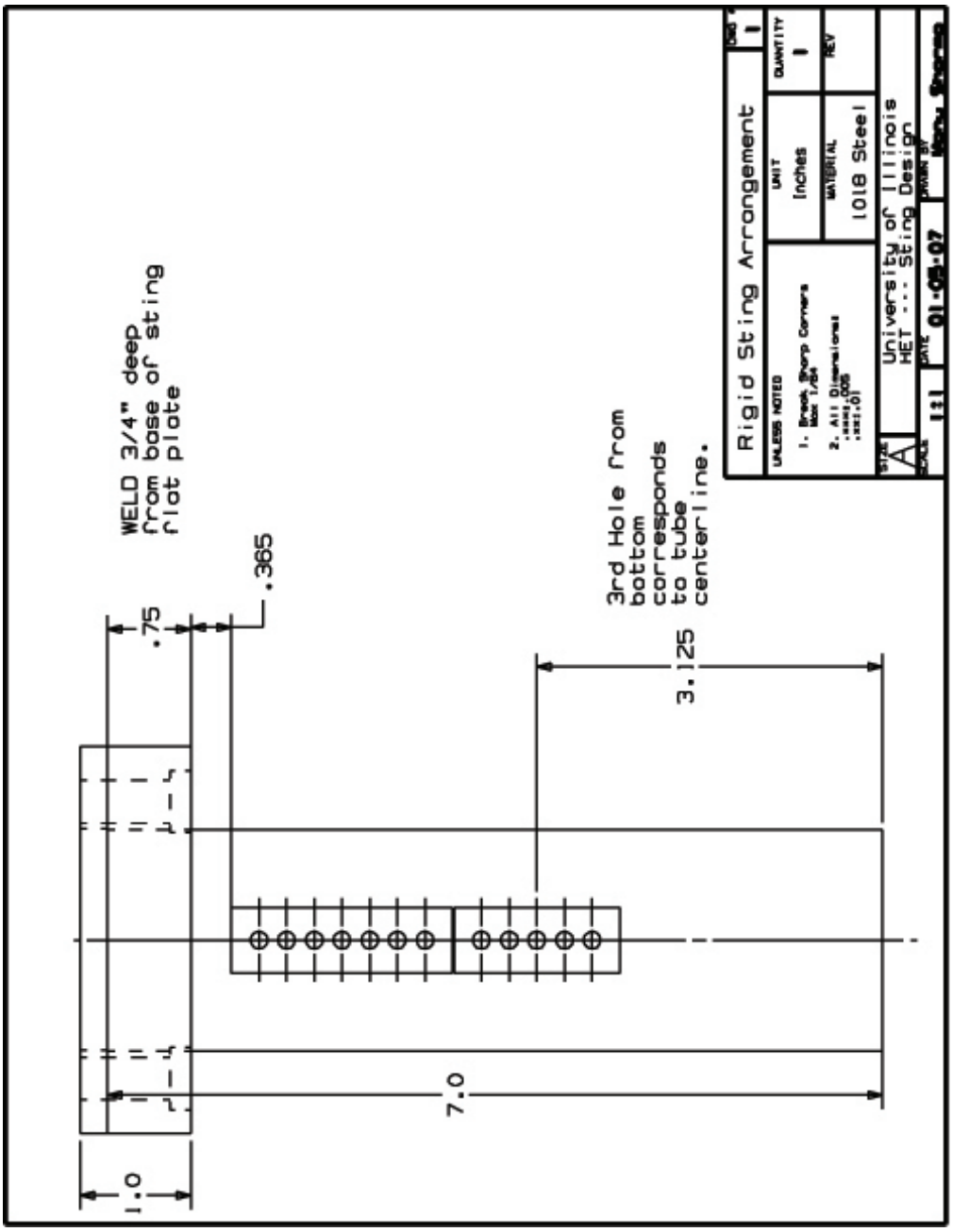

Figure B.3: Sting assembly including rod and flate plate

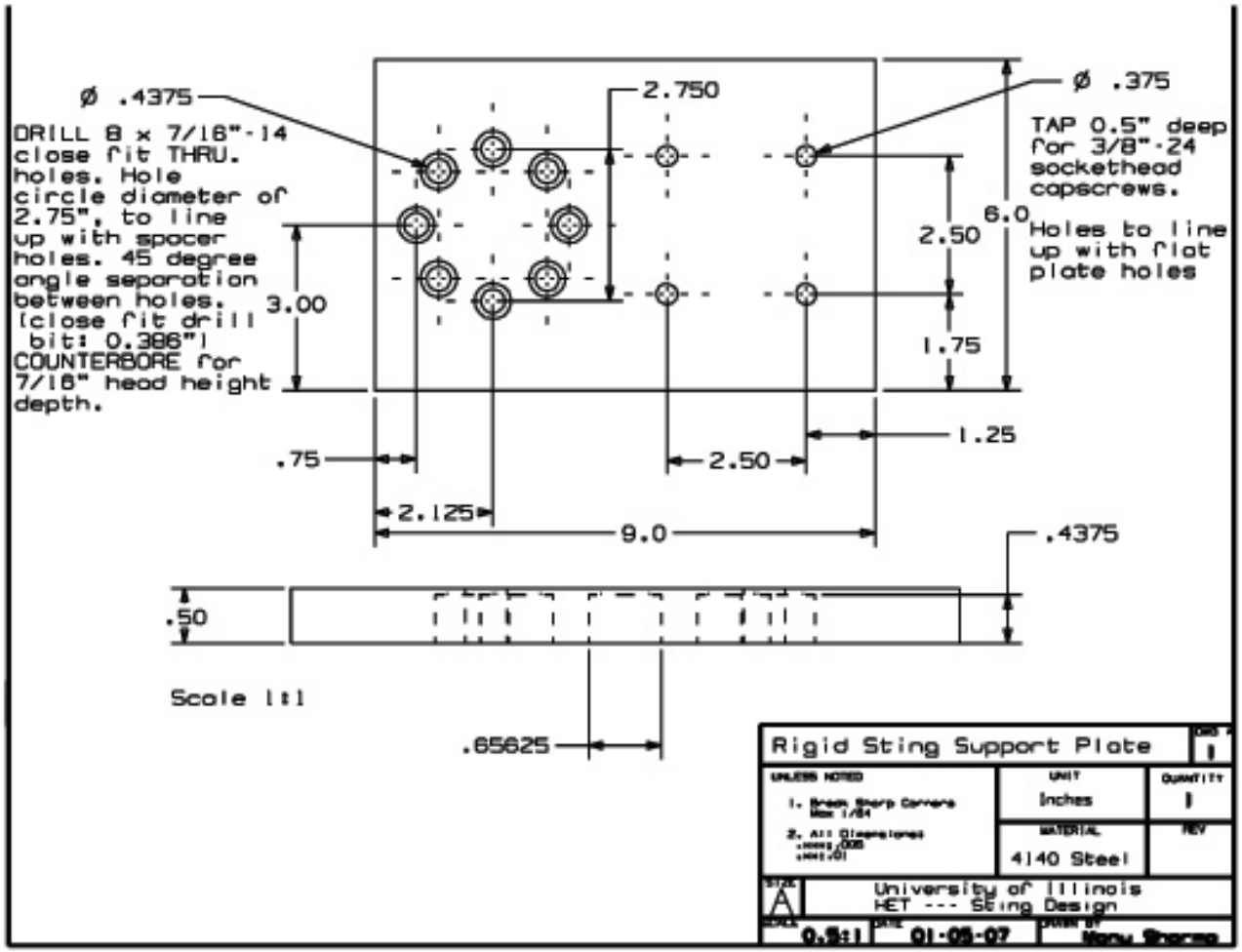

Figure B.4: Support plate for sting mounting.

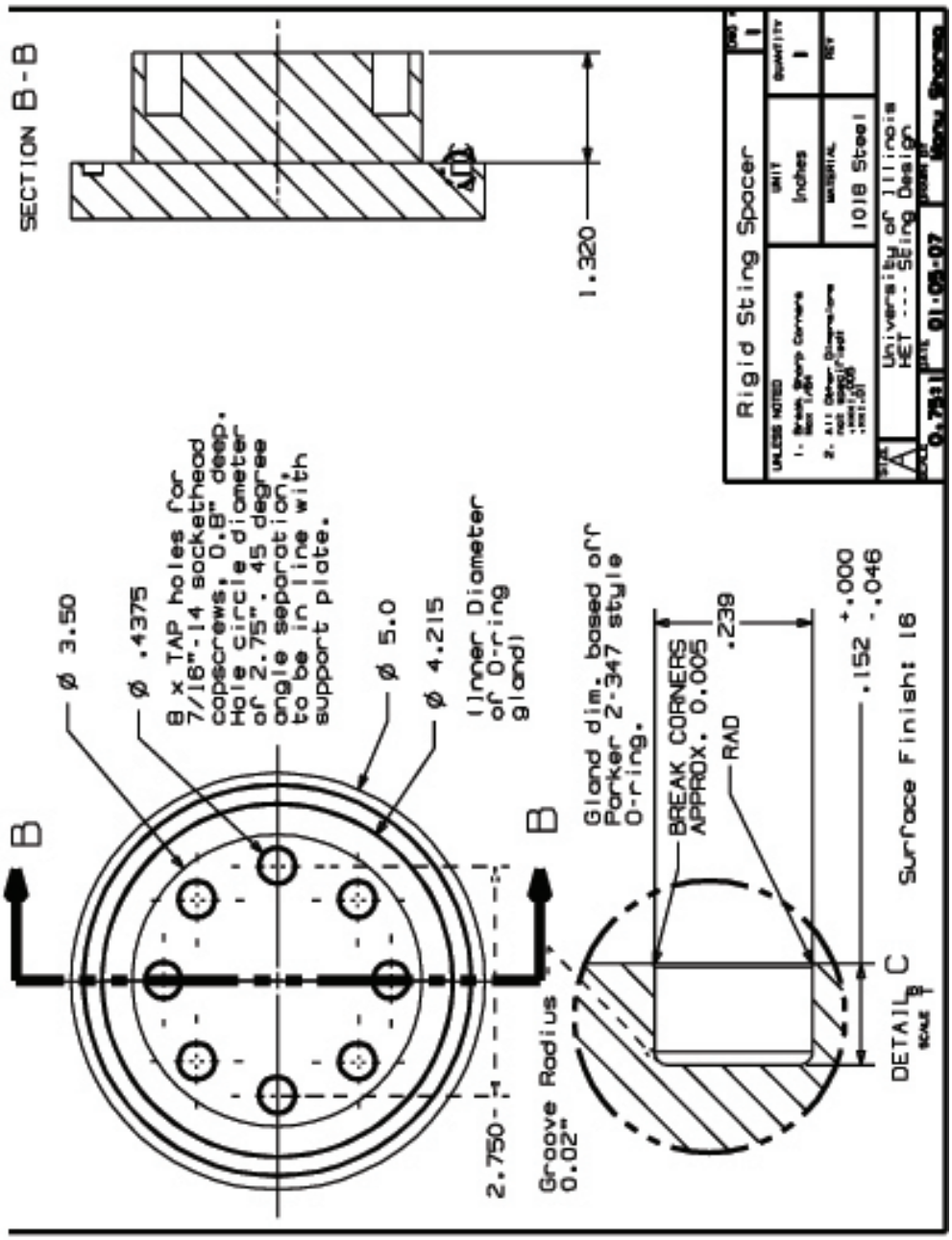

Figure B.5: Spacer for sting mounting

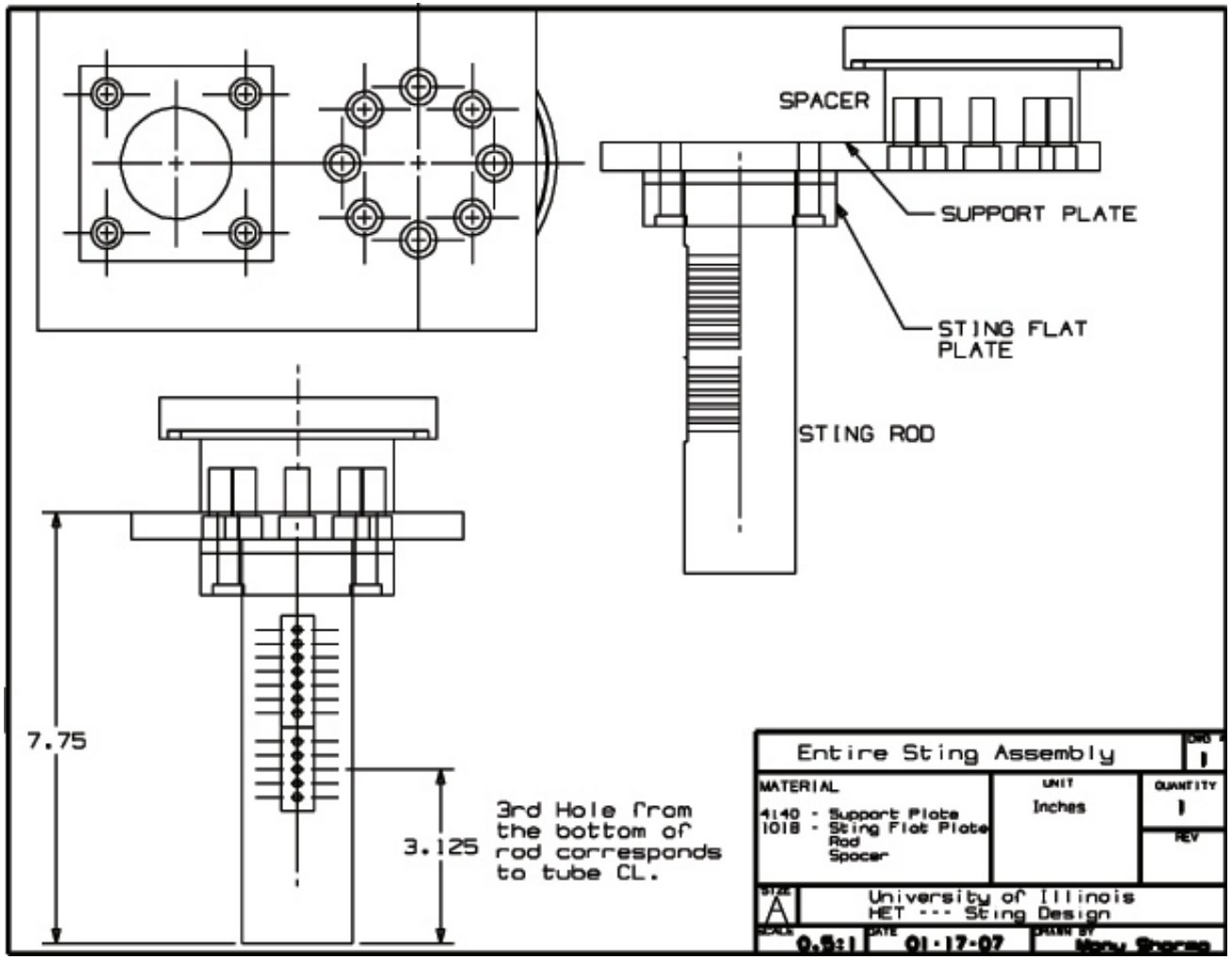

Figure B.6: Assembly of sting and sting mounting arrangement including rod, flat plate, support plate and spacer.

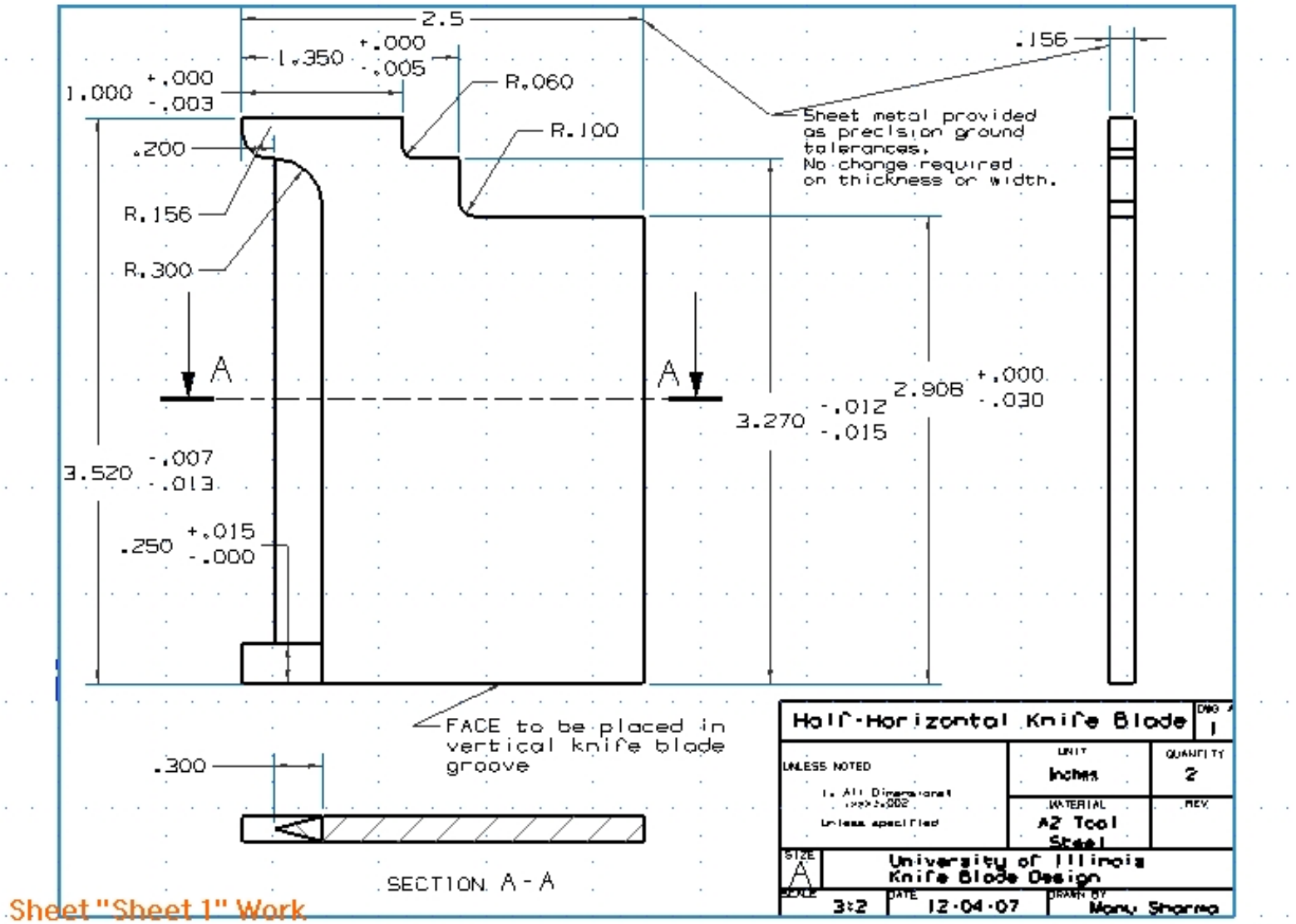

Figure B.7: Knife cross half-piece at pre-weld stage.

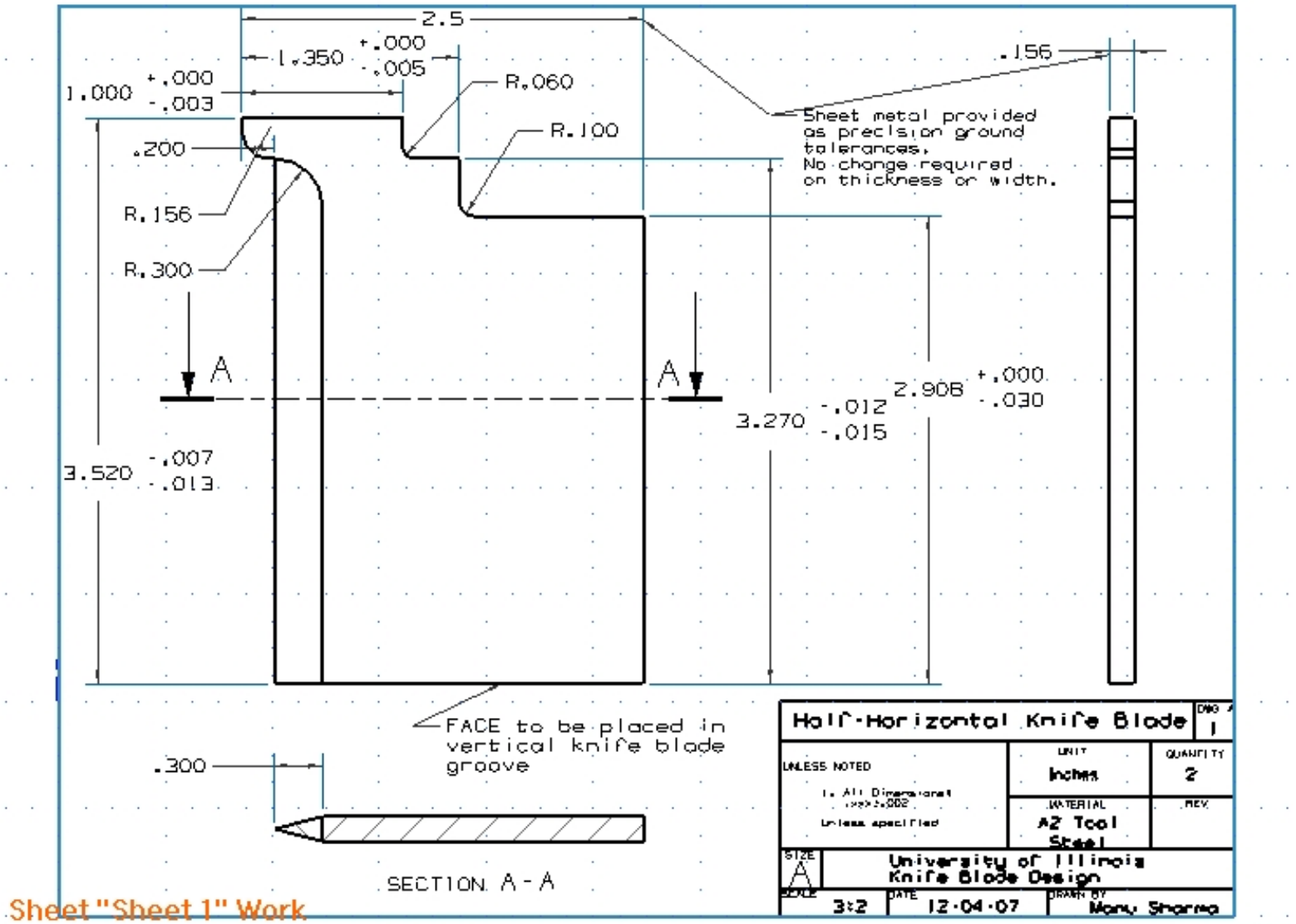

Figure B.8: Knife cross half-piece post-weld stage.

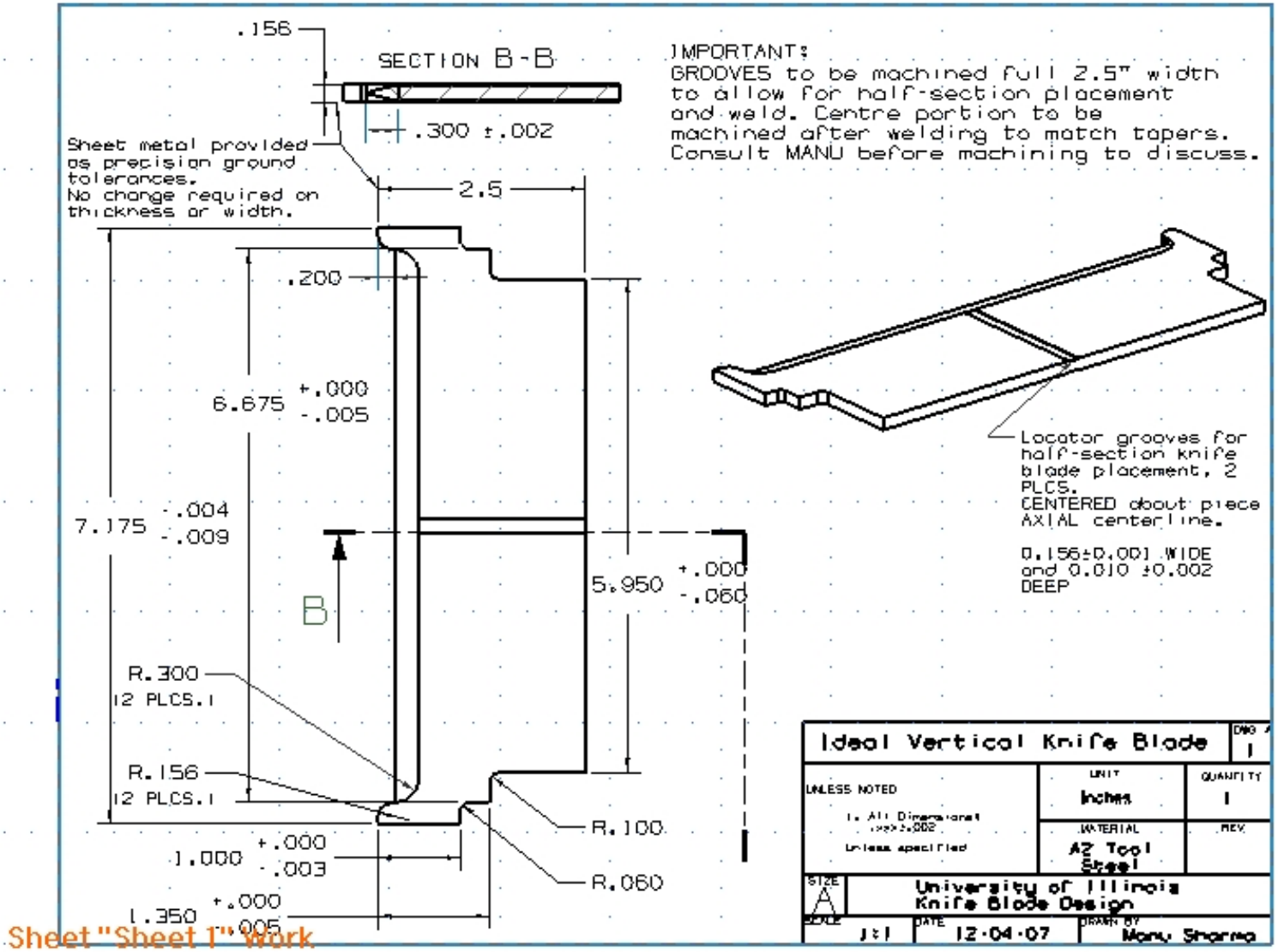

Figure B.9: Knife cross single piece.

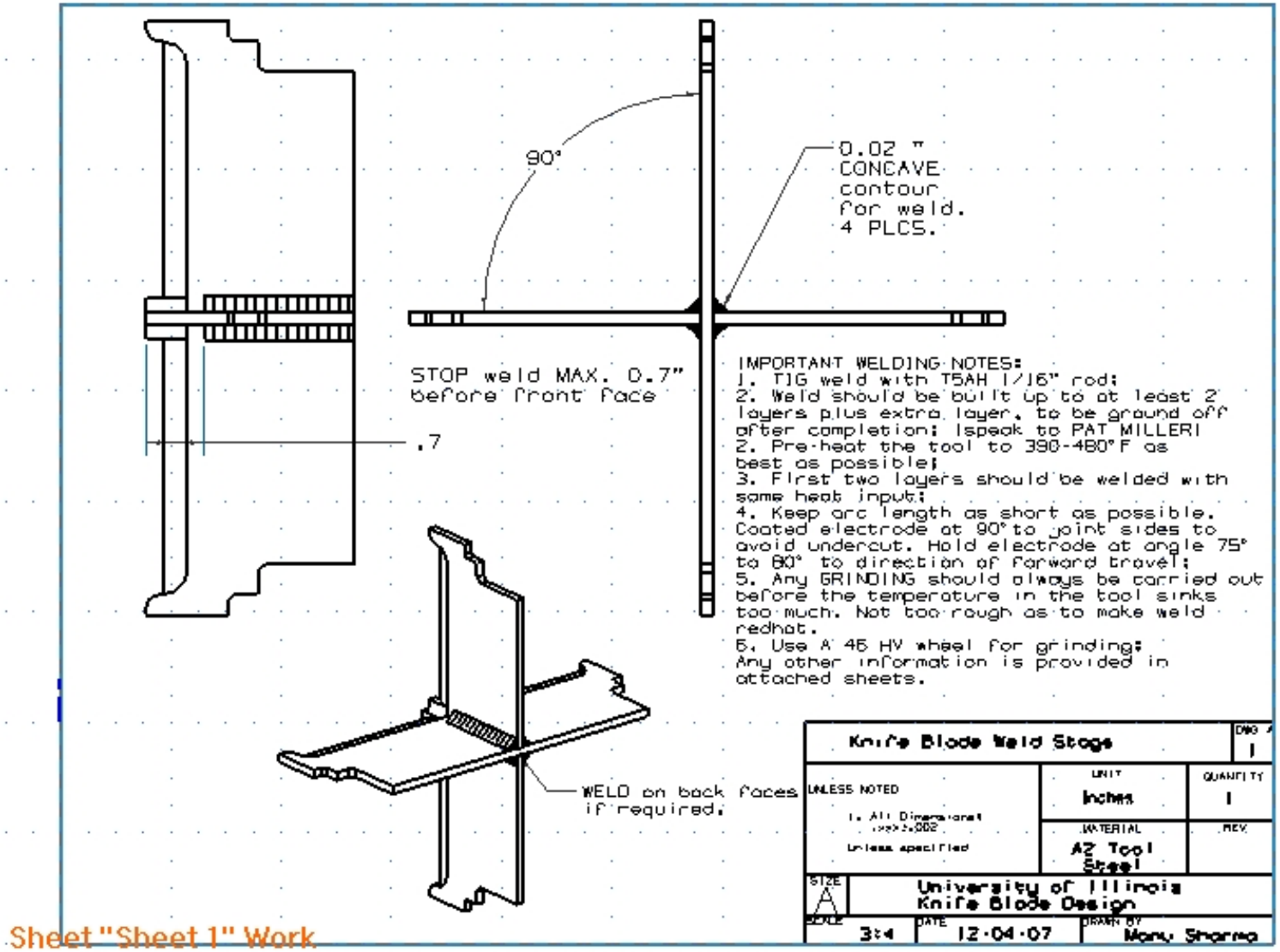

Figure B.10: Full blade assembly pre-weld stage.

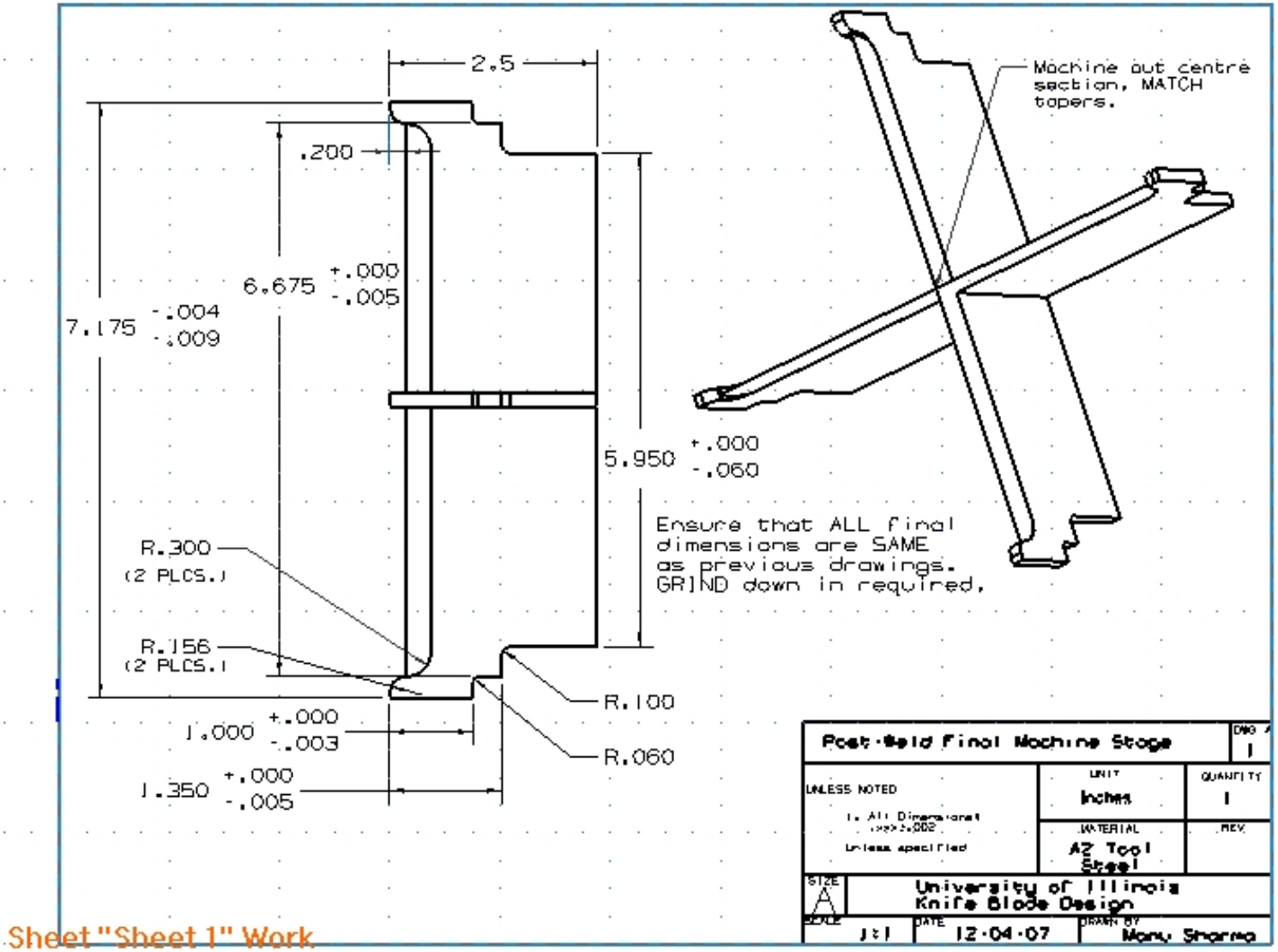

Figure B.11: Full blade assembly post-weld stage.

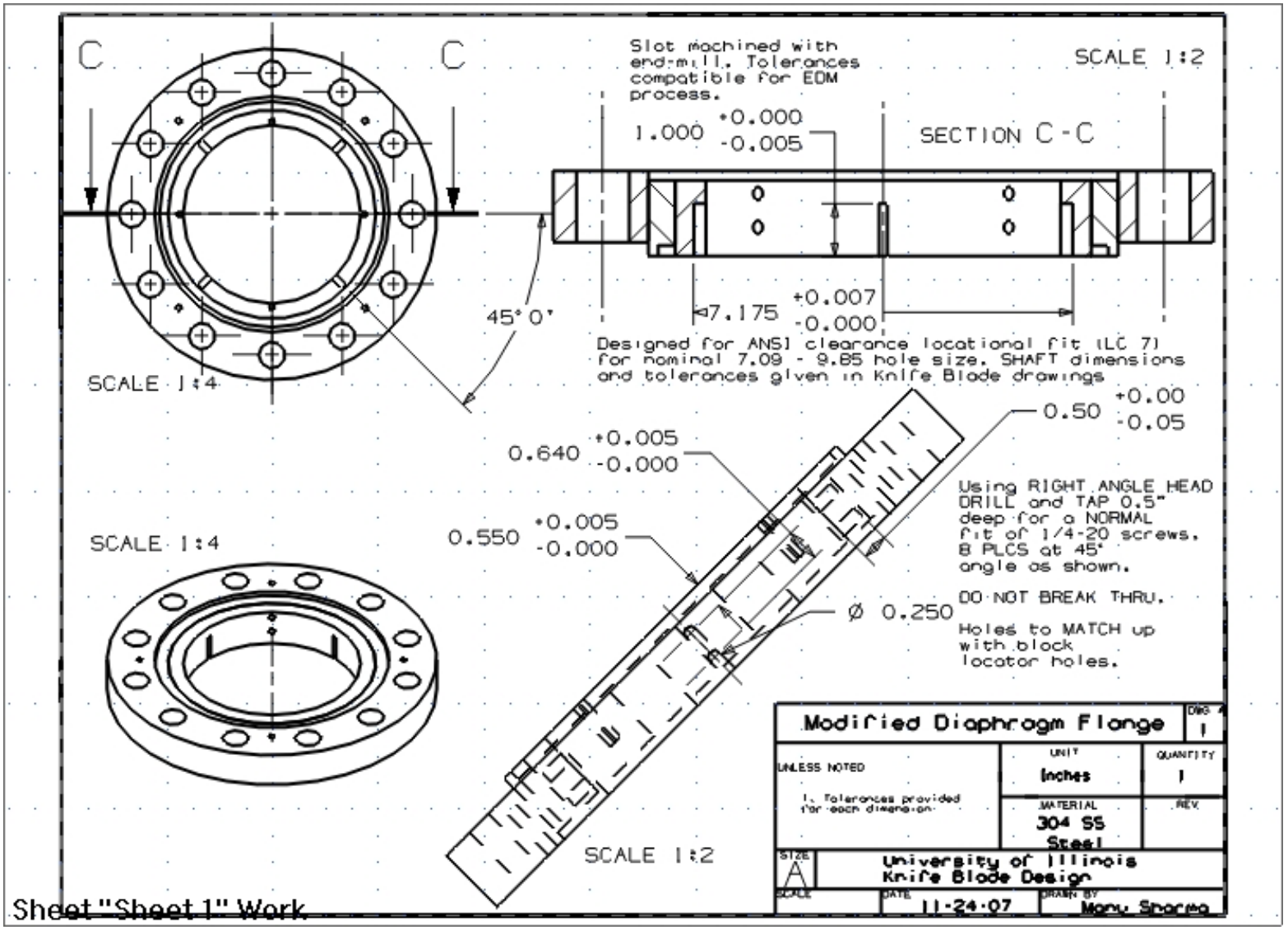

Figure B.12: Modified diaphragm flange.

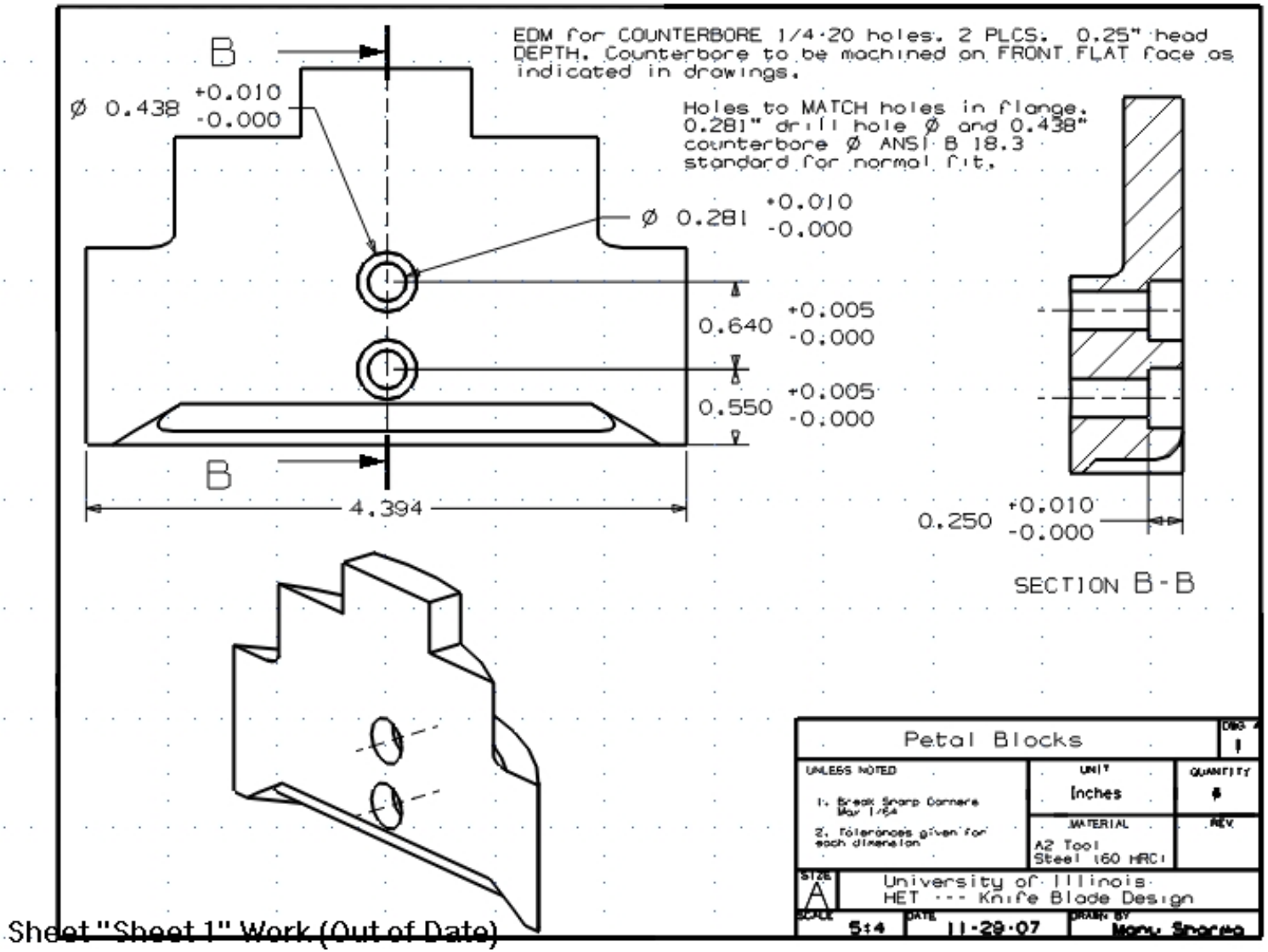

Figure B.13: Modified blocks.

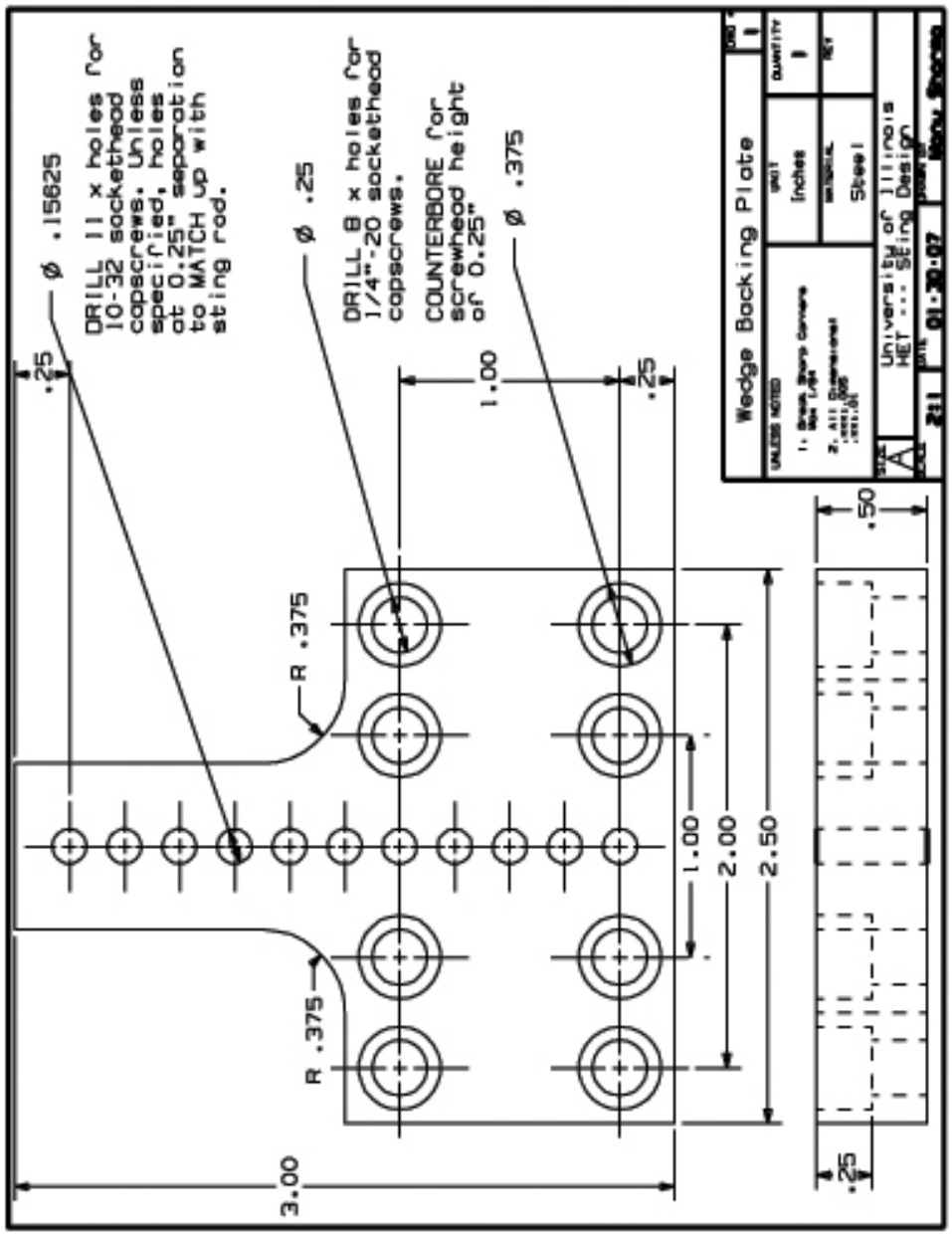

Figure B.14: Backing Plate for Wedges

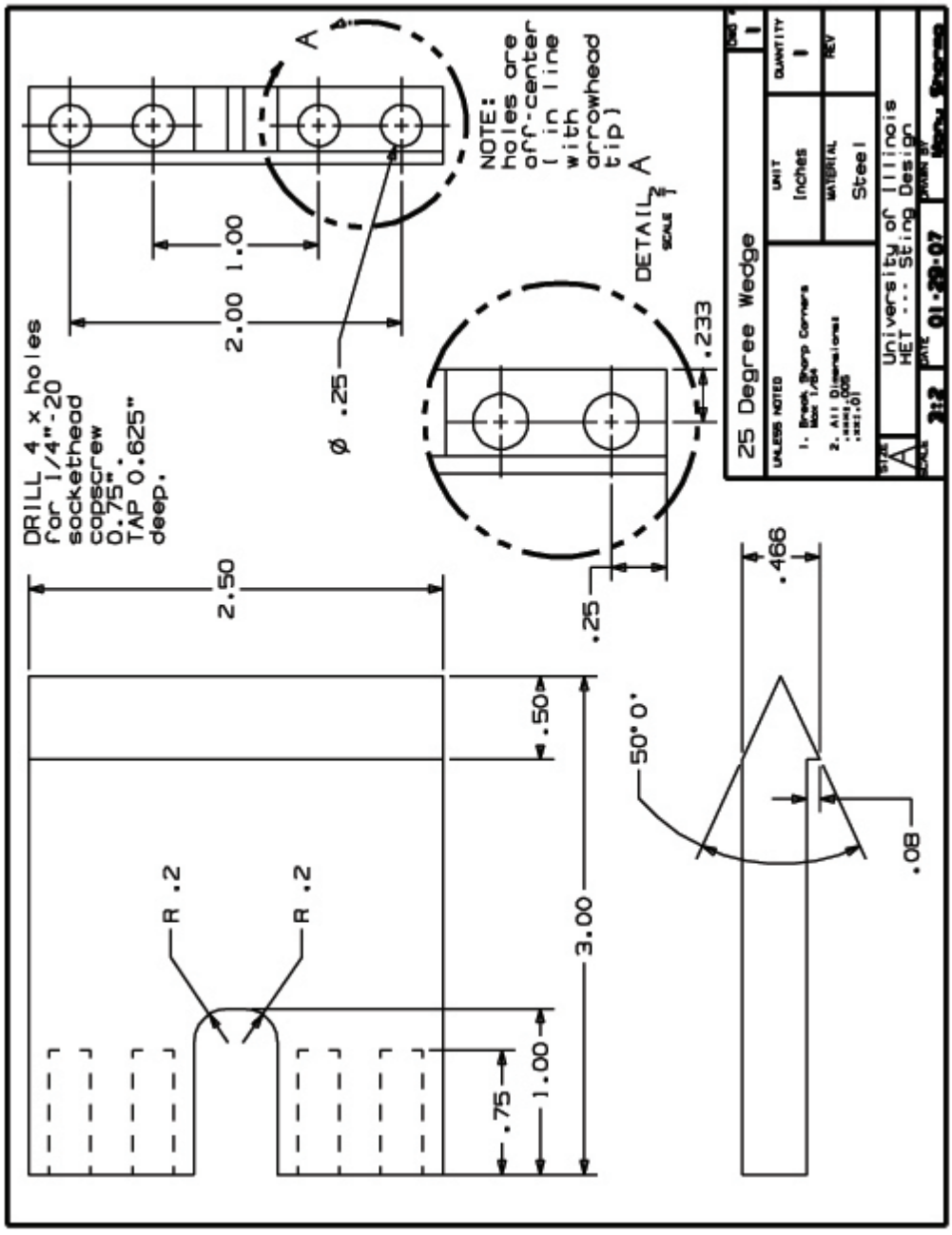

Figure B.15: 25° Wedge for shear layer experiments.

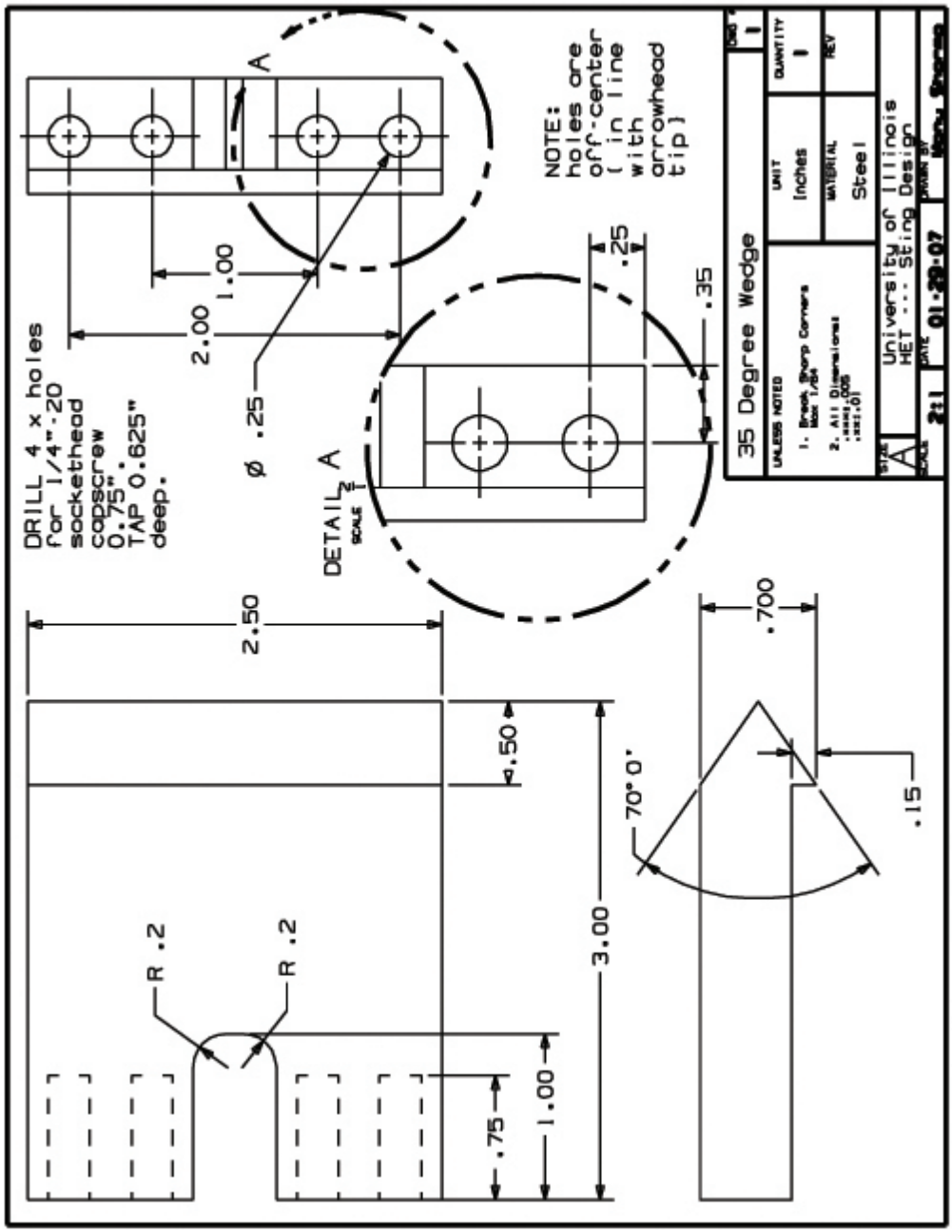

Figure B.16: 35° Wedge for shear layer experiments.

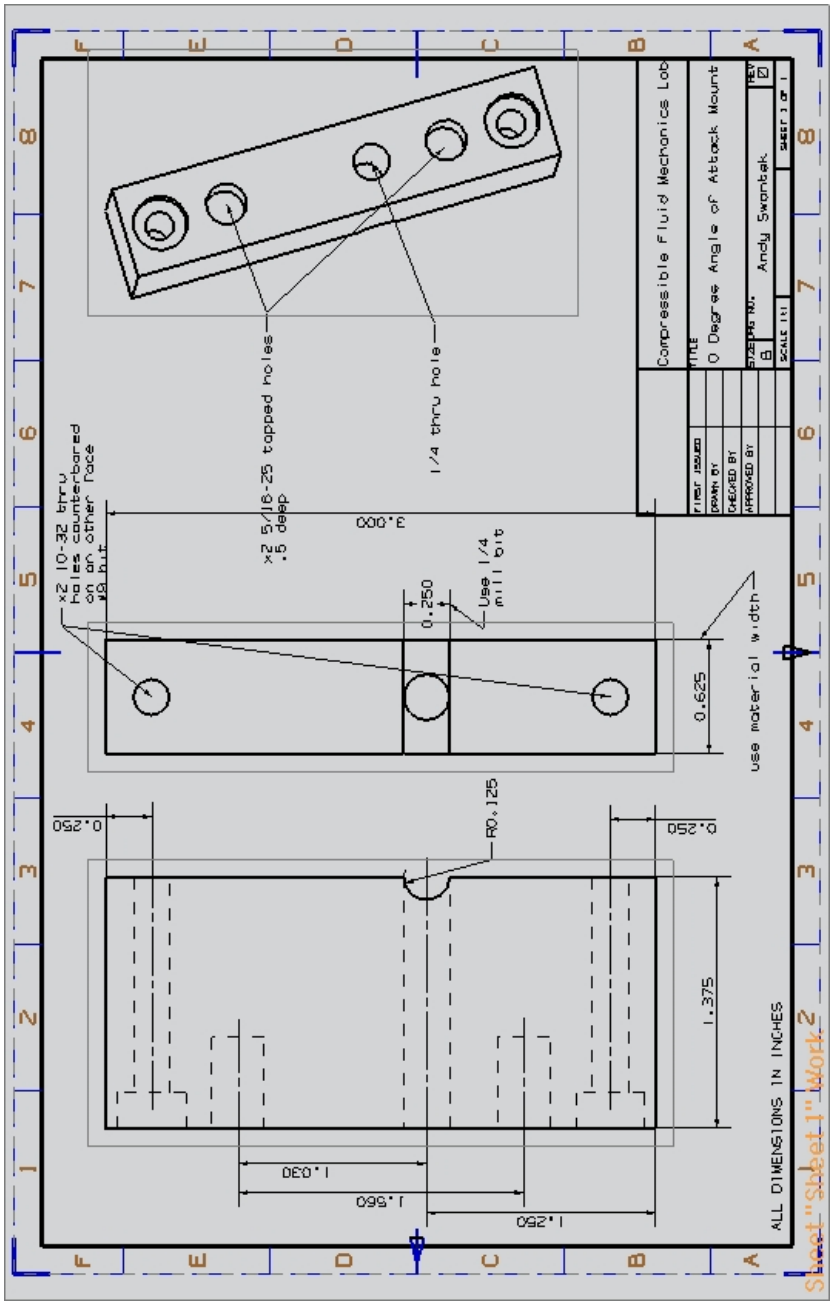

Figure B.17: 0 degree angle of attack mount for the Mars Science Lander.

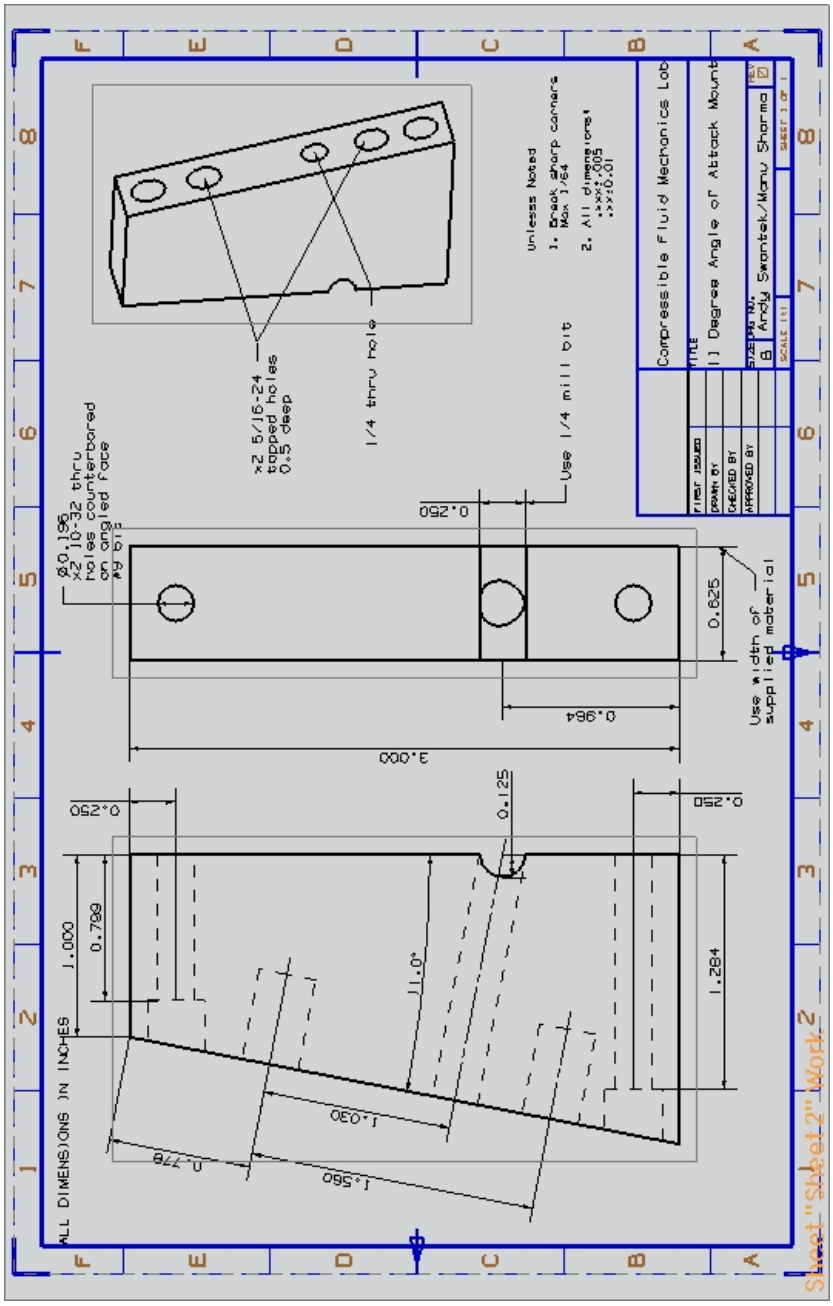

Figure B.18: 11 degree angle of attack mount for the Mars Science Lander.

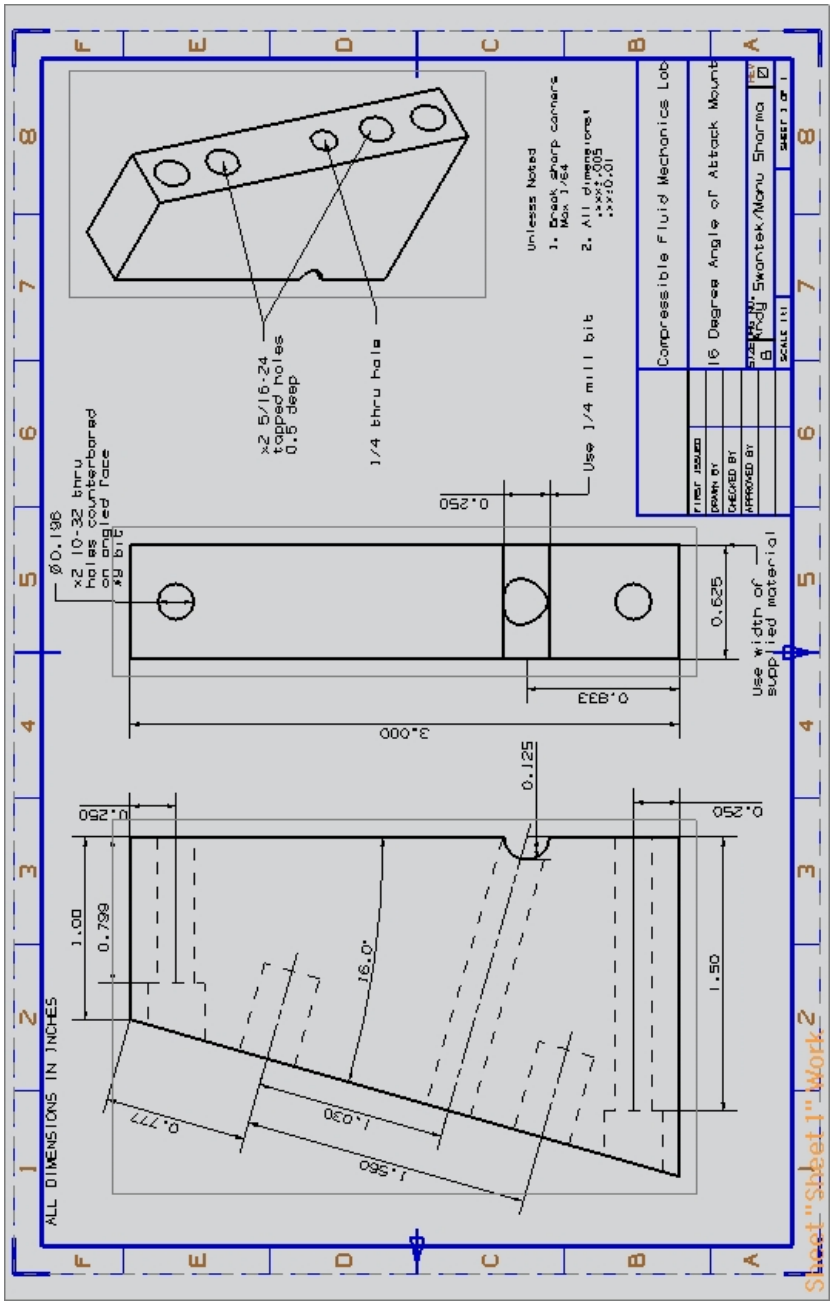

Figure B.19: 16 degree angle of attack mount for the Mars Science Lander.

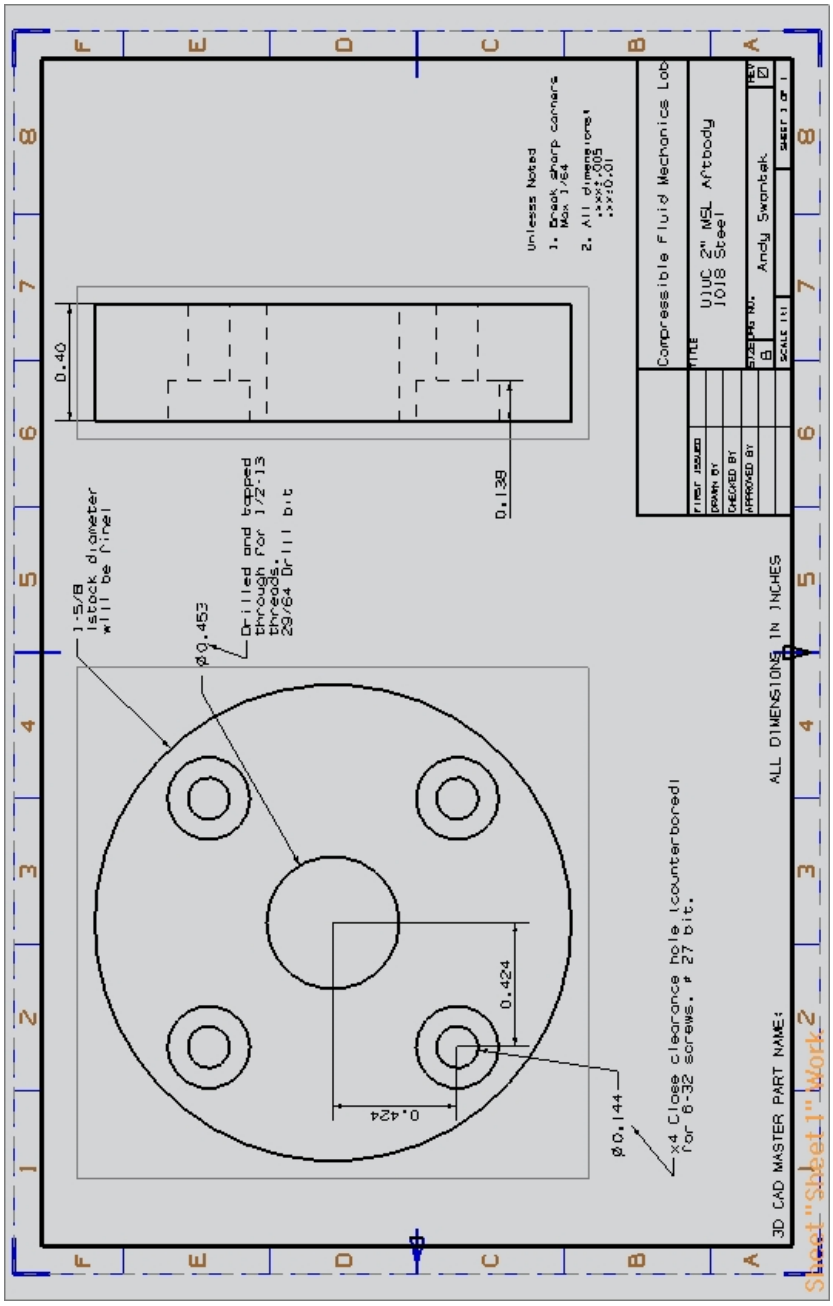

Figure B.20: Aftbody geometry for Mars Science Lander model used in the HET.

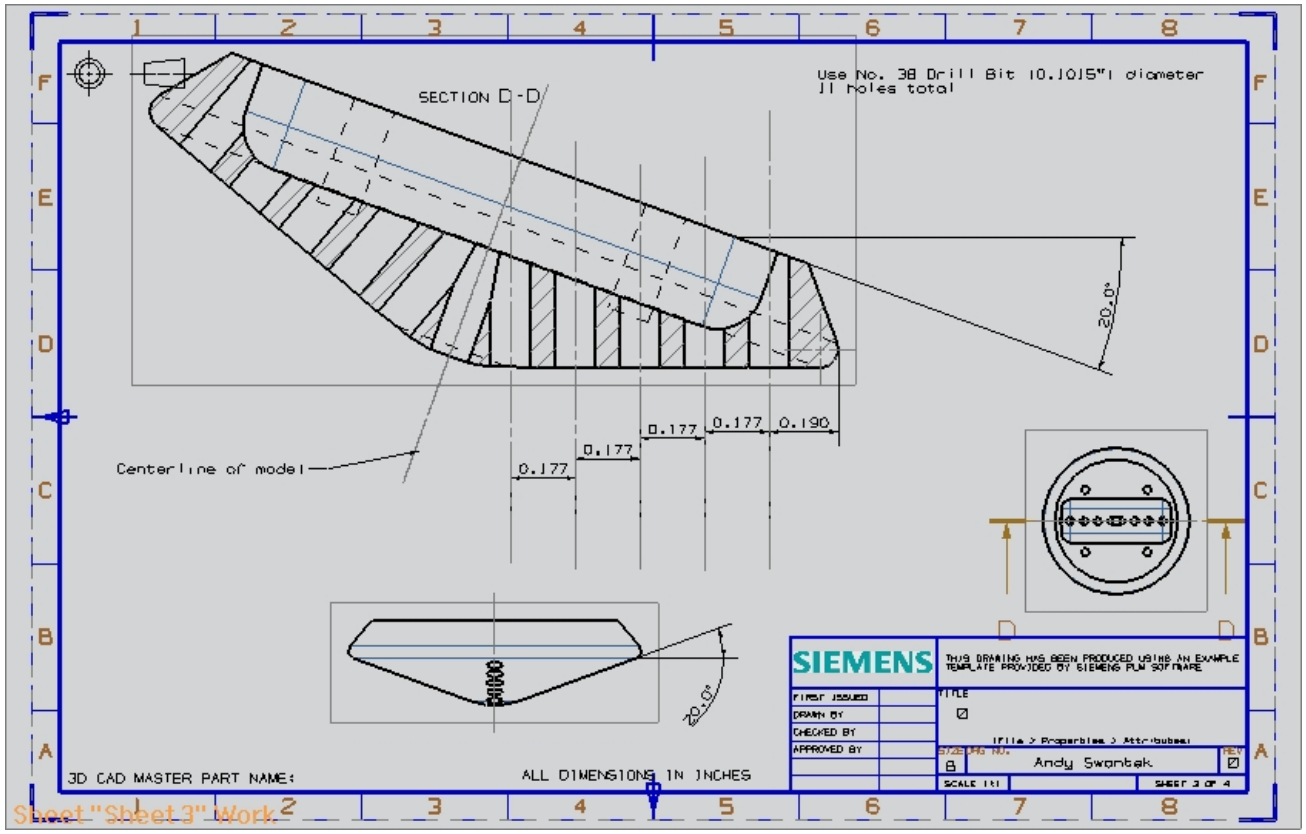

Figure B.21: 70 degree sphere-cone forebody Mars Science Lander used in the HET. Model dimensions are 1/90th the scale of the actual vehicle.

REFERENCES

[1] Holden, M. S., Wadhams, T. P., MacLean, M., and Mundy, E., "Experimental Studies in LENS I and X to Evaluate Real Gas Effects on Hypervelocity Vehicle Performance," *45th AIAA Aerospace Sciences Meeting and Exhibit*, 2007, AIAA Paper 2007-204.

[2] Hollis, B. R., Leichy, D. S., Wright, M. J., Holden, M. S., Wadhams, T. P., MacLean, M., and Dyakonov, A., "Transition Onset and Turbulent Heating Measurements for the Mars Science Laboratory Entry Vehicle," *43rd AIAA Aerospace Sciences Meeting and Exhibit*, 2005, AIAA Paper 2005-1437.

[3] Holden, M. S., Wadhams, T. P., Smolinski, G. J., MacLean, M., Harvey, J. K., and Walker, B. J., "Experimental and Numerical Studies on Hypersonic Vehicle Performance in the LENS Shock and Expansion Tunnels," *44th AIAA Aerospace Sciences Meeting and Exhibit*, 2006, AIAA Paper.

[4] Holden, M. S. and MacLean, M., "Catalytic Effects on Heat Transfer Measurements for Aerothermal Studies with CO_2," *44th AIAA Aerospace Sciences Meeting and Exhibit*, 2006, AIAA Paper 2006-182.

[5] Hollis, B. R. and Perkins, J. N., "High-Enthalpy and Perfect-Gas Heating Measurements on a Blunt Cone," *Journal of Spacecraft and Rockets*, Vol. 33, No. 5, 1996, pp. 628–634.

[6] Hollis, B. R. and Perkins, J. N., "High-Enthalpy Aerothermodynamics of a Mars Entry Vehicle Part 1: Experimental Results," *Journal of Spacecraft and Rockets*, Vol. 34, No. 4, 1997, pp. 449–456.

[7] Wright, M. J., Olejniczak, J., Brown, J. L., Hornung, H. G., and Edquist, K. T., "Computational Modeling of T5 Laminar and Turbulent Heating Data on Blunt Cones, Part 2: Mars Applications," *43rd AIAA Aerospace Sciences Meeting and Exhibit*, 2005, AIAA Paper 2005-177.

[8] Stewart, D. A. and Chen, Y. K., "Hypersonic Convective Heat Transfer over 140-deg Blunt Cones in Different Gases," *Journal of Spacecraft and Rockets*, Vol. 31, No. 5, 1994, pp. 735–743.

[9] Edquist, K. T., Liechty, D. S., Hollis, B. R., Alter, S. J., and Loomis, M. P., "Aeroheating Environments for a Mars Science Lander," *Journal of Spacecraft and Rockets*, Vol. 43, No. 2, 2006, pp. 330–339.

[10] Wright, M. J., Olejniczak, J., Brown, J. L., Hornung, H. G., and Edquist, K. T., "Modeling of Shock Tunnel Aeroheating Data on the Mars Science Laboratory Aeroshell," *J. Thermophysics and Heat Transfer*, Vol. 20, No. 4, 2006, pp. 641–651.

[11] Hollis, B. R. and Perkins, J. N., "High-Enthalpy Aerothermodynamics of a Mars Entry Vehicle Part 1: Computational Results," *Journal of Spacecraft and Rockets*, Vol. 34, No. 4, 1997, pp. 457–463.

[12] MacLean, M. and Holden, M. S., "Numerical Assesment of Data in Catalytic and Transitional Flows for Martian Entry," *9th AIAA/ASME Joint Thermophysics and Heat Transfer Conference*, 2006, AIAA Paper 2006-2940.

[13] Maclean, M. and Holden, M., "Assessment of Aerothermal Heating Augmentation attributed to Surface Catalysis in High Enthalpy Shock Tunnel Flows," *Sixth European Symposium on Aerothermodynamics for Space Vehicles*, 2008.

[14] Doraiswamy, S., Kelley, J. D., and Candler, G. V., "Vibrational Modeling of CO_2 in High Enthalpy Nozzle Flows," *in press Journal of Thermophysics and Heat Transfer*, 2010.

[15] Candler, G. V., Doraiswamy, S., and Kelley, J. D., "The Potential Role of Electronically-Excited States in Recombining Flows," *48th AIAA Aerospace Sciences Meeting*, 2010, AIAA Paper 2010-912.

[16] Holden, M. S., Wadhams, T. P., and MacLean, M., "Experimental Studies in the LENS Supersonic and Hypersonic Tunnels for Hypervelocity Vehicle Performance and Code Validation," *15th AIAA International Space Planes and Hypersonic Systems and Technologies Conference*, 2008, AIAA Paper 2008-2505.

[17] Gnoffo, P., Weilmuenster, K., Braun, R., and Cruz, C., "Influence of Sonic Line Location on Mars Pathfinder Probe Aerodynamics," *Journal of Spacecraft and Rockets*, Vol. 33, No. 2, 1996, pp. 169–177.

[18] Spencer, D., Blanchard, R., Braun, R., Kallemeyn, P., and Thurman, S., "Mars Pathfinder Entry, Descent and Landing Reconstruction," *Journal of Spacecraft and Rockets*, Vol. 36, No. 3, 1996, pp. 357–366.

[19] O'Byrne, S., Danehy, P. M., and Houwing, A. F. P., "Nonintrusive Temperature and Velocity Measurements in a Hypersonic Nozzle Flow," *22nd AIAA Aerodynamic Measurement Technology and Ground Testing Conference*, 2002, AIAA Paper 2002-2917.

[20] Lukasiewicz, J., *Experimental Methods of Hypersonics*, Marcel Dekker, Inc., New York, 1973.

[21] Hornung, H. G., "Experimental hypervelocity flow simulation, needs, achievements and limitations," *Proc. 1st Pacific Int. Conf. on Aerospace Science and Technology*, 1994.

[22] *Advanced Hypersonic Test Facilities*, ed. F K. Lu and D E. Marren, Progress in Astronautics and Aeronautics Series v. 198, AIAA, 2002.

[23] Trimpi, R. L., "Preliminary theoretical study of the expansion tube, new device for producing high enthalpy short-duration hypersonic gas flows," , No. TR R-133, 1962.

[24] Shinn, J. L. and Miller, C. G., "Experimental perfect gas study of expansion-tube flow characteristics," *NASA TP 1317*, 1978.

[25] Dufrene, A., Sharma, M., and Austin, J. M., "Design and characterization of a hypervelocity expansion tube facility," *Journal of Propulsion and Power*, Vol. 23, No. 6, 2007, pp. 1185–1193.

[26] Paull, A. and Stalker, R. J., "Test flow disturbances in an expansion tube," *Journal of Fluid Mechanics*, Vol. 245, 1992, pp. 493–521.

[27] Dufrene, A., MacLean, M., Parker, R. A., Wadhams, T. P., and Holden, M., "Characterization of the New LENS Expansion Tunnel Facility," *48th AIAA Aerospace Sciences Meeting*, 2010, AIAA Paper 2010-1564.

[28] Sasoh, A., Ohnishi, Y., Ramjuan, D., Takayama, K., and Otsu, H., "Effective Test Time Evaluation in High-Enthalpy Expansion Tube," *AIAA Journal*, Vol. 39, No. 11, 2001, pp. 2141–2147.

[29] Neely, A. J. and Morgan, R. G., "The Superorbital Expansion Tube Concept, Experiment and Analysis," *Aeronautical Journal*, Vol. 98, No. 973, 1994, pp. 97–105.

[30] McIntyre, T. J., Bishop, A. I., Thomas, A. M., Sasoh, A., and Rubinsztein-Dunlop, H., "Ionizing nitrogen and air flows ina superorbital expansion tube," *AIAA Journal*, Vol. 38, No. 9, 2000, pp. 1685–1691.

[31] Abdel-Jawad, M., Mee, D., Morgan, R., Jacobs, P., and Philpot, J., "Transient Force Measurements at Superorbital Speeds," *23rd International Symposium on Shock Waves*, 2001.

[32] Ben-Yakar, A. and Hanson, R. K., "Characterization of Expansion Tube Flows for Hypervelocity Combustion Studies," *Journal of Propulsion and Power*, Vol. 18, No. 4, 2002.

[33] Sharma, M., "Further Development and Experimentation with the Hypervelocity Expansion Tube," M.S. Thesis, University of Illinois at Urbana-Champaign, 2007.

[34] McGilvray, M., Austin, J. M., Sharma, M., Jacobs, P. A., and Morgan, R. G., "Diagnostic modelling of an expansion tube operating condition," *Shock Waves*, Vol. 19, No. 1, 2009, pp. 59–66.

[35] Dufrene, A., "Design and characterization of the hypervelocity expansion tube," M.S. Thesis, University of Illinois at Urbana-Champaign, 2006.

[36] "AISI A2: Cold work tool steel," Boehler Uddeholm Corporation, 2003.

[37] Oberg, E., Jones, F. D., Horton, H. L., and Ryffel, H. H., "Machinery's Handbook," *Industrial Press Inc*, 1992.

[38] Brouillette, M. and Sturtevant, B., "Experiments on the Richtmyer-Meshkov instability:Small-scale perturbations on a continuous interface," *Journal of Fluid Mechanics*, Vol. 263, 1994, pp. 271–292.

[39] Bonazza, R. and Sturtevant, B., "X-ray measurements of growth rates at a gas interface accelerated by shock waves," *Physics of Fluids*, Vol. 8, No. 9, 1996, pp. 2496–2512.

[40] Puranik, P. B., Oakley, J. G., Anderson, M. H., and Bonazza, R., "Experimental study of the Richtmyer-Meshkov instability induced by a Mach 3 shock wave," *Shock Waves*, Vol. 13, No. 6, 2004, pp. 413–429.

[41] Richtmyer, R. D., "Taylor Instability in Shock Acceleration of Compressible Fluids," *Communications on Pure and Applied Mathematics*, Vol. 13, 1960, pp. 297–319.

[42] Meshkov, Y. Y., "Instability of a Shock Wave Accelerated Interface Between Two Gases," *NASA Technical Translation-13074*, 1970, pp. 15.

[43] Sadot, O., Elez, L., Alon, U., Oron, D., Levin, L. A., Erez, G., Ben-Dor, G., and Shvarts, D., "Study of nonlinear evolution of single-mode and two-bubble interaction under Richtmyer-Meshkov instability," *Physical Review Letters*, Vol. 80, No. 8, 1998, pp. 1654–1657.

[44] Houas, L., Farhat, A., and Brun, R., "Shock induced Rayleigh-Taylor instability in the presence of a boundary layer," *Physics of Fluids*, Vol. 31, No. 4, 1987, pp. 807–812.

[45] Giovanni, M. D., Marcel Dekker, Inc, 1982.

[46] Pierce, A. D., *Acoustics: An Introduction ot Its Physical Principles and Applications*, McGraw-Hill, Inc, 1989.

[47] Mirels, H., "Shock Tube Test Time Limitation Due to Turbulent-Wall Boundary Layer," *AIAA Journal*, Vol. 2, No. 10, 1964, pp. 84–93.

[48] Mirels, H., "Test time in Low-Pressure Shock Tubes," *Physics of Fluids*, Vol. 6, No. 9, 1963, pp. 1201–1214.

[49] Mirels, H., "Laminar Boundary Layer behind Shock advancing into Stationary Fluid," *NACA Technical Note 3401*, Vol. 25p, 1955.

[50] Mirels, H., "Boundary Layer behind Shock or Thin Expansion Wave moving into Stationary Fluid," *NACA Technical Note 3712*, Vol. 53p, 1956.

[51] Reshotko, E., "Boundary-Layer Stability and Transition," *Annual Review of Fluid Mechanics*, Vol. 8, 1976.

[52] Wilkinson, S. P., "A Review of Hypersonic Boundary Layer Stability Experiments in a Quiet Mach 6 Wind Tunnel," *35th AIAA Aerospace Sciences Meeting and Exhibit*, 2009, AIAA Paper 2009-153.

[53] Casper, K. M., Bereshy, S. J., Henfling, J. F., Spillers, R. W., Pruett, B., and Schneider, S. P., "Hypersonic Wind-Tunnel Measurements of Boundary-Layer Pressure Fluctuations," *39th AIAA Fluid Dynamics Conference*, 2009, AIAA Paper 4054.

[54] Alba, C. R., Casper, K. M., Beresh, S. J., and Schneider, S. P., "Comparison of Experimentally Measured and Computed Second-Mode Disturbances in Hypersonic Boundary-Layers," *35th AIAA Aerospace Sciences Meeting and Exhibit*, 2010, AIAA Paper 2010-897.

[55] Mack, L. M., "Linear Stability Theory and the Problem of Supersonic Boundary-Layer Transition," *AIAA Journal*, Vol. 13, No. 3, 1975.

[56] Candler, G. V., Mavriplis, D. J., and Trevino, L., "Current Status and Future Prospects for the Numerical Simulation of Hypersonic Flows," AIAA Paper 2009-153, Jan. 2009.

[57] Erdman, P. W., Zipf, E. C., Howlett, L. C., Levin, D. A., Collins, R. J., and Candler, G. V., "Flight Measurements of Low-Velocity Bow Shock Ultraviolet Radiation," *Journal of Thermophysics and Heat Transfer*, Vol. 7, No. 1, 1993, pp. 37–41.

[58] Levin, D. A., Candler, G. V., Collins, R. J., Erdman, P. W., Zipf, E., Espy, P., and Howlett, C., "Comparison of Theory with Experiment for the Bow Shock Ultraviolet Rocket Flight," *Journal of Thermophysics and Heat Transfer*, Vol. 7, No. 1, 1993, pp. 30–36.

[59] Levin, D. A., Candler, G. V., Collins, R. J., Erdman, P. W., Zipf, E. C., and Howlett, L. C., "Examination of Theory for Bow Shock Ultraviolet Rocket Experiments - I," *Journal of Thermophysics and Heat Transfer*, Vol. 8, No. 3, 1994, pp. 447–452.

[60] Levin, D. A., Candler, M. B. G. V., Collins, R. J., and Smith, G. P., "Examination of Theory for Bow Shock Ultraviolet Rocket Experiments - II," *Journal of Thermophysics and Heat Transfer*, Vol. 8, No. 3, 1994, pp. 453–459.

[61] Levin, D. A., Collins, R. J., Candler, G. V., Wright, M. J., and Erdman, P. W., "Examination of OH Ultraviolet Radiation from Shock-Heated Air," *Journal of Thermophysics and Heat Transfer*, Vol. 10, No. 2, 1996, pp. 200–208.

[62] Levin, D. A., Candler, G. V., and Collins, R. J., "Overlay Method for Calculating Excited State Species Properties in Hypersonic Flows," *AIAA Journal*, Vol. 35, No. 2, 1997, pp. 288–294.

[63] Levin, D. A., Laux, C. O., and Kruger, C. H., "A general model for the spectral calculation of OH radiation in the ultraviolet," *Journal of Quantitative Spectroscopy and Radiative Transfer*, Vol. 61, No. 3, 1999, pp. 377–392.

[64] Levin, D. A., Gimelschein, S. F., and Gimelschein, N. E., "Examination of Water Dissociation Models in Shock-Heated Air," *Journal of Thermophysics and Heat Transfer*, Vol. 16, No. 2, 2002, pp. 251–260.

[65] Levin, D. A., Gimelschein, S. F., and Gimelschein, N. E., "Quasi-classical Trajectory Modeling of OH Production in Direct Simulation Monte Carlo," *Journal of Thermophysics and Heat Transfer*, Vol. 19, No. 2, 2005, pp. 235–244.

[66] Gimelschein, N. E., Levin, D. A., and Gimelschein, S. F., "Hydroxyl Formation Mechanisms and Models in High-Altitude Hypersonic Flows," *AIAA Journal*, Vol. 41, No. 7, 2003, pp. 1323–1331.

[67] Kossi, K. K. and Boyd, I. D., "Detailed Computation of Ultraviolet Spectra in Rarefied Hypersonic Flow," *Journal of Spacecraft and Rockets*, Vol. 35, No. 5, 1998, pp. 653–659.

[68] Nerem, R. M., Carlson, L. A., and Hartsel, J. E., "Chemical Relaxation Phenomena behind Normal Shock Waves in a Dissociated Freestream," *AIAA Journal*, Vol. 5, No. 5, 1966, pp. 910–916.

[69] Russo, A. L., "Spectrophotometric Measurements of the Vibrational Relaxation of CO in Shock-Wave and Nozzle Expansion-Flow Environments," *Journal of Chemical Physics*, Vol. 47, No. 12, 1967, pp. 5201–5210.

[70] Moser, L. K. and Hindelang, F. J., "Vibrational relaxation of NO behind shock waves," *Experiments in Fluids*, Vol. 7, No. 1, 1989, pp. 67–69.

[71] Moser, L. K. and Hindelang, F. J., "Shock-tube Study of the Vibrational Relaxation of Nitric Oxide," *17th International Symposium on Shock Waves and Shock Tubes*, AIP, Bethlehem, PA, 1990, pp. 531–536.

[72] Sharma, S. P. and Gillespie, W., "Nonequilibrium and Equilibrium Shock Front Radiation Measurements," *Journal of Thermophysics and Heat Transfer*, Vol. 5, No. 3, 1991, pp. 257–265.

[73] Allen, R. A., Keck, J. C., and Camm, J. C., "Non-Equilibrium Radiation from Shock Heated Nitrogen and a Determination of the Recombination Rate," AVCO-Everett Research Laboratory, Report-110, 1961.

[74] Allen, R. A., "Nonequilibrium Shock Front Rotational, Vibrational and Electronic Temperature Measurements," AVCO-Everett Research Laboratory, Report-1986, 1964.

[75] Allen, R. A., Keck, J. C., and Camm, J. C., "Radiation from Hot Nitrogen," AVCO-Everett Research Laboratory, Report-102, 1961.

[76] Labracherie, L., Billiotte, M., and Houas, L., "Nonequilibrium Determination of Temperature Profiles by Emission Spectroscopy," *Journal of Quantitative Spectroscopy and Radiative Transfer*, Vol. 54, No. 3, 1995, pp. 573–579.

[77] Ramjuan, D., Dumitrescu, M., and Brun, R., "Kinetics of Free Radicals Behind Strong Shock Waves," *Journal of Thermophysics and Heat Transfer*, Vol. 13, No. 2, 1999, pp. 219–225.

[78] Rond, C., Boubert, P., Felio, J. M., and Chikhaoui, A., "Nonequilibrium radiation behind a strong shock wave in CO_2-N_2," *Journal of Chemical Physics*, Vol. 340, No. 1-3, 2007, pp. 93–104.

[79] Wurster, W. H., Treanor, C. E., and Williams, M. J., "Nonequilibrium UV Radiation and Kinetics Behind Shock Waves in Air," 1989, AIAA Paper 1989-1918.

[80] Wurster, W. H., Treanor, C. E., and Williams, M. J., "Kinetics of UV Production Behind Shock Waves in Air," AIAA Paper 1990-1666.

[81] Babikian, D. S., Gopaul, N. K. J. M., and Park, C., "Measurement and Analysis of Nitric Oxide Radiation in an Arcjet Flow," *Journal of Thermophysics and Heat Transfer*, Vol. 8, No. 4, 1994, pp. 737–743.

[82] Park, C. S., Newfield, M. E., Fletcher, D. G., and Goekçen, T., "Spectroscopic Measurements of Shock-Layer Flows in an Arcjet Facility," *Journal of Thermophysics and Heat Transfer*, Vol. 13, No. 1, 1999, pp. 60–67.

[83] Park, C. S., Newfield, M. E., Fletcher, D. G., Goekçen, T., and Sharma, S. P., "Spectroscopic Emission Measurements Within the Blunt-Body Shock Layer in an Arcjet Flow," *Journal of Thermophysics and Heat Transfer*, Vol. 12, No. 2, 1998, pp. 190–197.

[84] Staack, D., Farouk, B., Gutsol, A. F., and Fridman, A. A., "Spectroscopic studies and rotational and vibrational temperature measurements of atmospheric pressure normal glow plasma discharges in air," *Plasma Sources Science and Technology*, Vol. 15, No. 4, 2006, pp. 818–827.

[85] I.Nompelis, Candler, G. V., and Holden, M. S., "Effect of Vibrational Nonequilibrium on Hypersonic Double-Cone Experiments," *AIAA Journal*, Vol. 41, No. 11, 2003, pp. 2162–2169.

[86] C.Park, "Thermochemical Relaxation in Shock Tunnels," *Journal of Thermophysics and Heat Transfer*, Vol. 4, No. 4, 2006, pp. 690–698.

[87] Pilverdier, H., Brun, R., and Dumitrescu, M. P., "Emission and Raman spectroscopy measurements in hypersonic nitrogen flows," *Journal of Thermophysics and Heat Transfer*, Vol. 15, No. 4, 2001, pp. 484–490.

[88] Boubert, P., Chaiz, A., Chikhaoui, A., Robin, L., and Versich, P., "Aerodynamic calibration of TCM2 facility and study of a bow shock layer by emission and laser spectroscopy," *Shock Waves*, Vol. 11, No. 5, 2002, pp. 341–351.

[89] Ramjuan, D., Sasoh, A., Ohnishi, Y., and Takayama, K., "Time-resolved spectroscopy in the shock layer of a blunt body placed in an expansion tube flow," *24th International Congress on High-Speed Photography and Photonics*, Vol. 4183, 2001.

[90] McGilvray, M., Austin, J. M., Sharma, M., Jacobs, P. A., and Morgan, R. G., "Diagnostic modelling of an expansion tube operating condition for a hypersonic shear layer experiment," *Proceedings of the 16th Australasian Fluid Mechanics Conference*, Gold Coast, Australia, 2007.

[91] Massa, L. and Austin, J. M., "Spatial linear stability of a hypersonic shear layer with nonequilibrium thermochemistry," *Physics of Fluids*, Vol. 20, No. 8, 2008, pp. 84–104.

[92] Adamovich, I. and Rich, J., "Three Dimensional Nonperturbative Analytical Model of Vibrational Energy Transfer in Atom-Molecule Collisions," *Journal of Chemical Physics*, Vol. 109, No. 18, 1998, pp. 7711–7724.

[93] Macheret, S. and Adamovich, I., "Semiclassical Modelling of State Specific Dissociation Rates in Diatomic Gases," *Journal of Chemical Physics*, Vol. 113, No. 17, 2000, pp. 7351–7361.

[94] Adamovich, I., "Three Dimensional Analytical Model of Vibrational Energy Transfer in Molecule-Molecule Collisions," *AIAA Journal*, Vol. 39, No. 10, 2001, pp. 1916–1925.

[95] Bose, D. and Candler, G. V., "Thermal rate constants of the N_2+O→NO+N reaction using *ab initio* potential energy surfaces," *Journal of Chemical Physics*, Vol. 10, No. 8, 1996, pp. 2825–2833.

[96] Bose, D. and Candler, G. V., "Thermal rate constants of the O_2+N→NO+O reaction based on *ab initio* potential energy surfaces," *Journal of Chemical Physics*, Vol. 107, No. 16, 1997, pp. 6136–6145.

[97] Kolesnick, G. D. B. R. E., "Vibrational Relaxation of Oxygen. State to State Rate Constants," *Chemical Physics Letters*, Vol. 200, No. 4, 1992, pp. 382–386.

[98] Billing, G. D., "Rate Constants and Cross Sections for Vibrational Transitions in Atom-Diatom and Diatom-Diatom Collisions," *Computer Physics Communications*, Vol. 32, No. 1, 1984, pp. 45–62.

[99] Millikan, R. C. and White, D. R., "Systematic of Vibrational Relaxation," *Journal of Chemical Physics*, Vol. 39, No. 12, 1963, pp. 3209–3213.

[100] Ormonder, S., "Vibrational Relaxation Theories and Measurements," *Review of Modern Physics*, Vol. 47, No. 1, 1975, pp. 193–258.

[101] Baulch, D., Drysdale, D., and Horne, D., "Evaluated Kinetic Data for High Temperature Reactions," *CRC, Boca Raton*, Vol. 2-3.

[102] Camac, M. and Vaughan, A., "O_2 Dissociation Rates in O_2-Ar Mixtures," *Journal of Chemical Physics*, Vol. 34, No. 2, 1961, pp. 460–470.

[103] Taylor, R. L., Camac, M., and Feinberg, R. M., "Measurements of Vibration-Vibration Coupling in Gas Mixtures," Avco Everett Reseach Lab Report, Report-250, 1966.

[104] Skews, B. W., "Aspect ratio effects in wind tunnel studies of shock wave reflection transition," *Shock Waves*, Vol. 7, 1997, pp. 373–383.

[105] Li, H., Chpoun, A., and Ben-Dor, G., "Analytical and experimental investigations of the reflection of asymmetric shock waves in steady flows," *Journal of Fluid Mechanics*, Vol. 390, 1999, pp. 25–43.

[106] Gimelschein, S., Markelov, G., and Ivanov, M., "Relaxation and Rarefaction Effects on Shock Wave Reflections," AIAA Paper 1998-2819, 1998.

[107] Grasso, F. and Paoli, R., "An Analytical Study of Mach Reflection in Nonequilibrium Steady Flows," *Physics of Fluids*, Vol. 11, No. 10, 1999, pp. 3150–3167.

[108] Burtschell, Y., Zeitoun, D. E., and Ben-Dor, G., "Steady shock wave reflections in thermochemical nonequilibrium flows," *Shock Waves*, Vol. 11, 2000, pp. 15–21.

[109] Grasso, F. and Paoli, R., "Simulations of Shock-Wave Reflections in Nonequilibrium Flows," *Journal of Spacecraft and Rockets*, Vol. 37, No. 2, 2000, pp. 224–234.

[110] Luque, J. and Crosley, D. R., "LIFBASE: Database and Spectral Simulation Program (Version 1.5)," SRI International Report MP 99-009, 1999.

[111] Kovacs, I., *Rotational Structure in the Spectra of Diatomic Molecules*, 1969.

[112] Amiot, C., "The Infrared Emission Spectrum of NO: Analysis of the Δv =3 Sequence up to v=22," *Journal of Molecular Spectroscopy*, Vol. 94, 1982, pp. 150–172.

[113] Ory, H. A., Gittleman, A. P., and Maddox, J. P., "Franck-Condon Factors for the NO Beta and Gamma Band Systems," *Astrophysical Journal*, Vol. 139, No. 1, 1963, pp. 346–356.

[114] Luque, J. and Crosley, D. R., "Radiative and predissociative rates for NO $A^2\sum^+$ v′=0-5 and $D^2\sum^+$ v′=0-3," *Journal of Chemical Physics*, Vol. 112, No. 21, 2000, pp. 9411–9416.

[115] Luque, J. and Crosley, D. R., "Transition probabilities and electronic transition moments of the $A^2\sum^+ \rightarrow X^2\prod$ and $D^2\sum^+ \rightarrow X^2\prod$ systems of nitric oxide," *Journal of Chemical Physics*, Vol. 111, No. 16, 1999, pp. 7405–7415.

[116] Velasco, A. M., Martin, I., Lavin, C., and Bustos, E., "Radiative lifetimes for the $A^2\sum^+$ (v′=0-7) and $D^2\sum^+$ (v′=0-5) Rydberg states of NO," *Molecular Physics*, Vol. 103, No. 10, 2005, pp. 1375–1385.

[117] McBride, B. J. and Gordon, S., "Computer Program for Calculation of Complex Chemical Equilibrium Compositions and Applications, II. Users Manual and Program Description," NASA CR-1311, 1996.

[118] Wen, C. Y. and Hornung, H. G., "Non-equilibrium dissociating flow over spheres," *Journal of Fluid Mechanics*, Vol. 299, 1995, pp. 389–405.

[119] Hornung, H. G. and Smith, G. H., "The Influence of Relaxation on Shock Detachment," *Journal of Fluid Mechanics*, Vol. 93, No. Pt.2, 1979.

[120] Wright, M. J., Tang, C. Y., Edquist, K. T., Hollis, B. R., Krassa, P., and Campbell, C. A., "A Review of Aerothermal Modeling for Mars Entry Missions," *48th AIAA Aerospace Sciences Meeting and Exhibit*, 2010, AIAA Paper 2010-443.

[121] Edquist, K., Dyakonov, A., Wright, M., and Tang, C., "Aerothermodynamic Environments Definition for the Mars Science Laboratory Entry Capsule," *45th AIAA Aerospace Sciences Meeting*, 2007, AIAA Paper 2007-1206.

[122] Netterfield, M. P., Mazoue, F., Marraffa, L., Kastell, D., and Eitelberg, G., "Experiments and Computations on a Blunt Body in High Enthalpy CO_2," *31st AIAA Thermophysics and Heat Transfer Conference*, 1996.

[123] Marschall, J., Copeland, R. A., Hwang, H. H., and Wright, M. J., "Surface Catalysis Experiments on Metal Surfaces in Oxygen and Carbon Monoxide Mixtures," *44th AIAA Aerospace Sciences Meeting and Exhibit*, 2006, AIAA Paper 2006-181.

[124] Nompelis, I., Drayna, T. W., and Candler, G. V., "Development of a Hybrid Unstructured Implicit Soliver for the Simulation of Reacting Flows Over Complex Geometries," *34th AIAA Fluid Dynamics Conference*, 2004, AIAA Paper 2004-2227.

[125] Sanderson, S. R., "Shock wave interaction in hypervelocity flow," *PhD Thesis, California Institute of Technology*, 1995.

[126] Davis, J.-P., "High-Enthalpy Shock/Boundary-Layer Interaction on a Double Wedge," *PhD Thesis, California Institute of Technology*, 1999.

[127] Rasheed, A., "Passive Hypervelocity Boundary Layer Control Using an Ultrasonically Absorptive Surface," *PhD Thesis, California Institute of Technology*, 2001.

[128] Croarkin, M. C., Guthrie, W. F., Burns, G. E., Kaeser, M., and Strouse, G. F., "Temperature-Electromotive Force Referance Function and Tables for the Letter-Designated Thermocouple Types Based on the ITS-90," Monograph 175, National Institute of Standard Technologies, 1993.

[129] Flaherty, W. and Austin, J. M., "Comparative Surface Heat Transfer Measurements in Hypervelocity Flow," *48th AIAA Aerospace Sciences Meeting and Exhibit*, 2010, AIAA Paper 2010-671.

[130] Sharma, M., Swantek, A. B., Flaherty, W., Glumac, N. G., and Austin, J., "Expansion Tube Investigation of Shock Stand-Off Distances in High-Enthalpy CO2 Flow Over Blunt Bodies," *48th AIAA Aerospace Sciences Meeting and Exhibit*, 2010, AIAA Paper 2010-1566.

[131] Sharma, M., Swantek, A. B., Flahety, W., Austin, J. M., Doraiswamy, S., and Candler, G. V., "Experimental and Numerical Investigation of Hypervelocity Carbon Dioxide Flow over Blunt Bodies," *Journal of Thermophysics and Heat Transfer*, 2010.

[132] Macrossan, M. N., "Hypervelocity flow of dissociating nitrogen downstream of a blunt nose," *Journal of Fluid Mechanics*, Vol. 217, 1990, pp. 167–202.

[133] Sharma, M., Austin, J. M., Glumac, N. G., and Massa, L., "NO and OH Spectroscopic Vibrational Temperature Measurements in a Post-Shock Relaxation Region," *in press AIAA Journal*.

[134] Spurk, J. H., "Design, operation and preliminary results of the BRL expansion tube," *Fourth Hypervelocity Technical Symposium, A.E.D.C*, 1965, pp. 114–144.

[135] Whitfield, J., Norfleet, G., and Wolny, W., "Status of Research on a High Performance Shock Tunnel," Tech. Rep. AEDC 65-272, U.S. Air Force, 1966.

[136] Lick, W., "Inviscid flow of a reacting mixture of gases around a blunt body," *Journal of Fluid Mechanics*, Vol. 9, No. 1, 1960, pp. 128–144.

[137] Hall, J. G., Eschendoeder, A. Q., and Marrone, P. V., "Blunt-nose inviscid ariflows with coupled non-equilibrium processes," *Journal of Aeronautical Space Sciences*, Vol. 29, No. 9, 1962, pp. 1038–1051.

[138] Hornung, H. G., "Non-equilibrium dissociating nitrogen flows over spheres and circular cylinders," *Journal of Fluid Mechanics*, Vol. 53, 1972, pp. 149–176.

[139] Inger, G. R., Higgins, C., and Morgan, R., "Shock Standoff on Hypersonic Blunt Bodies in Nonequilibrium Gas Flows," *Journal of Thermophysics and Heat Transfer*, Vol. 16, No. 2, 2002.

[140] Belouaggadia, N., Olivier, H., and Brun, R., "Numerical and theoretical study of the shock stand-off distance in non-equilibrium flows," *Journal of Fluid Mechanics*, Vol. 607, 2008, pp. 167–197.

[141] Olivier, H., "A theoretical model for the shock stand-off distance in frozen and equilibrium flow," *Journal of Fluid Mechanics*, Vol. 413, 2000, pp. 345–353.

[142] Wegener, P. P. and Buzyna, G., "Experiments on shock stand-off distance in non-equilibrium flow," *Journal of Fluid Mechanics*, Vol. 37, pt. 2, No. 2, 1969, pp. 325–335.

[143] Fay, J. A. and Riddell, F. R., "Theory of stagnation point heat transfer in dissociated air," *Journal of the Aeronautical Sciences*, Vol. 25, No. 2, 1999, pp. 73–85.

[144] Wen, C., "Hypervelocity Flow over Spheres," *PhD Thesis, California Institute of Technology*, 1994.

[145] Liechty, D. S., Hollis, B. R., and Edquist, K. T., "Mars Science Laboratory Experimental Aerothermodynamics with Effects of Cavities and Control Surfaces," *Journal of Spacecraft and Rockets*, Vol. 43, No. 2, 2006, pp. 340–353.

[146] Liechty, D. S. and Hollis, B. R., "Transition Due to Heat Shield Cavities on a Mars Entry Vehicle," *Journal of Spacecraft and Rockets*, Vol. 43, No. 2, 2006, pp. 354–366.

[147] Hollis, B. R. and Collier, A., "Turbulent Aeroheating Testing of Mars Science Laboratory Entry Vehicle in Nitrogen," *45th AIAA Aerospace Sciences Meeting*, 2007, AIAA Paper 2007-1208.

[148] Sutton, K. and Graves, A. R., "A general stagnation-point convective-heating equation for arbitary gas mixtures," Tech. rep., NASA, 1971.

[149] Ben-Dor, G., *Shock Wave Reflection Phenomena*, Springer, New York, 1991.

[150] Anderson, J., *Modern Compressible Flow: A Historical Perspective*, MGraw Hill Higher Education, New York, 2003.

[151] Ivanov, M., Klemenkov, G., Kudryavtsev, A., and Fomin, V., "Experimental investigation of the transition to the Mach reflection of steady shock waves," *Physics - Doklady*, Vol. 42, No. 12, 1997, pp. 691.